TECHNISCHE UNIVERSITÄT MÜNCHEN

Lehrstuhl für Aerodynamik und Strömungsmechanik

Analysis of stochastic models in fluids by simulations

Dmitrii Alexandrovich Azarnykh

Vollständiger Abdruck der von der Fakultät für Maschinenwesen der Technischen Universität München zur Erlangung des akademischen Grades eines

Doktor-Ingenieurs

genehmigten Dissertation.

Vorsitzender:	Prof. Phaedon-Stelios Koutsourelakis, Ph.D.
Prüfer der Dissertation:	Prof. Dr.-Ing. Nikolaus A. Adams
	Prof. Dr. rer. nat. Marco Ellero

Die Dissertation wurde am 26.02.2018 bei der Technischen Universität München eingereicht und durch die Fakultät für Maschinenwesen am 18.09.2018 angenommen.

Dmitrii Azarnykh
Straßbergerstr. 24
80809 München
Germany

azarnyih.dmitry@gmail.com

Released October 25, 2018
Typesetting LaTeX

KURZFASSUNG

Stochastische Modelle in der Strömungsdynamik werden verwendet, um Phänomene mit Skalenseparation zu beschreiben und stellen ein System von Differentialgleichungen mit einem stochastischen Term dar. Die Lösung stochastischer Gleichungen erfordert anspruchsvolle numerische Algorithmen, die verwendet werden können, um das Anwendungsspektrum stochastischer Modelle zu erweitern. Numerische Algorithmen für stochastische Modelle können sich von denen unterscheiden, die in deterministischen Modellen zum Einsatz kommen. Die Analyse stochastischer Modelle durch Simulationen kann genutzt werden, um die Genauigkeit der Algorithmen abzuschätzen.

Verschiedene stochastische Modelle können die gleichen physikalischen Phänomene repräsentieren und können in ähnlichen technischen Anwendungen eingesetzt werden. Die Äquivalenz der Modellparameter ist nicht immer gut definiert. Die Analyse stochastischer Modelle bietet die Möglichkeit, unterschiedliche stochastische Modelle miteinander zu verknüpfen und eventuell neue Anwendungen der vorhandenen Modelle zu finden.

In dieser Arbeit werden stochastische Modelle für zwei verschiedene Phänomene betrachtet: turbulente Strömung und thermische Fluktuationen. Die entsprechende Analyse, die auf Simulationen basiert, wird präsentiert. Die Arbeit ist folgendermaßen gegliedert:

In Kapitel 1 wird die Motivation der Arbeit dargelegt, die eng mit jüngsten Leistungen im Bereich stochastischer Modelle in der Strömungsmechanik verknüpft ist. Die Übersicht über die stochastischen Modelle mit ihren Anwendungen wird aufgeführt, gefolgt von der Liste der statistischen Größen, die für die Analyse von stochastischen Modellen durch Simulationen verwendet werden können. In Kapitel 2 werden mehrere stochastische Modelle, wie gitterbasiertes Landau-Lifshitz-Navier-Stokes Gleichungen, Smoothed Dissipative Particle Dynamics, Dissipative Particle Dynamics und Langevin-Modelle in der Eulerschen und Lagrangeschen Betrachutungsweise. Dabei wird ein Augenmerk auf die Diskussion der neuesten numerischen Algorithmen und statistischen Modellparameter gelegt. Die Erkenntnisse der wichtigsten durch Fachleute begutachteten Publikationen sind in Kapitel 3 aufgeführt. Die Liste der Veröffentlichungen wird in Kapitel 4 präsentiert. Im Anhang A sind drei Hauptpublikationen samt der Veröffentlichungsvereinbarungsmitteilung zur Wiederverwendung angefügt.

Abstract

Stochastic models in fluid dynamics are used to represent phenomena with scale separation and consist of a system of differential equations with a random term. The solution of the stochastic equations requires sophisticated numerical algorithms that can be used to expand the range of application of stochastic models. Numerical algorithms for stochastic models can differ from the ones those are used in deterministic models. The analysis of stochastic models by simulations can be used to estimate an accuracy of the algorithms.

Different stochastic models might represent the same physical phenomena and can be used in similar engineering applications. The correspondence between parameters of such models is not always well defined. Analysis of stochastic models offers the way to link different stochastic models with each other and possibly find new applications of the existing models.

In this thesis, stochastic models for two different phenomena are considered: turbulent flow and thermal fluctuations. The corresponding analysis that relies on simulations is provided. The thesis is structured in the following way:

In Chapter 1, the motivation of the thesis is stated, which is closely related to the recent achievements of stochastic models in fluid dynamics. The overview of stochastic models with applications is given, followed by a list of statistical characteristics that can be used for the analysis of stochastic models by simulations. In Chapter 2, several stochastic models such as grid-based Landau-Lifshitz Navier-Stokes equations, the smoothed dissipative particle dynamics, the dissipative particle dynamics and the Langevin models in Eulerian and Lagrangian reference frames are described in more details along with a discussion on the recent numerical algorithms and statistical characteristics of the models. Key findings of the main peer-reviewed publications are listed in Chapter 3. The list of publications can be found in Chapter 4 and the three major publications with the publisher agreement notification to reuse are attached in Appendix A.

Acknowledgements

I would like to thank my "Doktorvater" Prof. Nikolaus A. Adams for the supervision, expert advice and encouragement. He has taught me the frontiers of numerical modeling in fluid dynamics and set high standards of scientific process which helped me to develop professionally. I am also sincerely grateful for the spirit of science which was created in the Institute of Aerodynamics and Fluid Mechanics and contributed to this thesis through fruitful discussions.

I thank Sergey Litvinov from whom I have learned a lot. He was always ready to help with his expertise in a wide range of methods and generously share his knowledge in computer science and software development.

I am grateful to Xin Bian for sharing parts of his code and providing critical and helpful advice. His impressive overview of meso-scale methods contributes to this thesis. He also was available for discussion on any issues that I had.

I also thank Vladimir Sabelnikov for providing hosting in ONERA, Prof. Chibbaro who helped to organize the trip and Nadezhda Petrova for sharing her code.

I would like to express my gratitude to Felix Schranner and Xiangyu Hu for fruitful discussion and sharing parts of the code. I would like to thank Philipp Neumann and Christoph Kowitz for their help with computational resources. I thank Anna Lukyanovich, Vladimir Bogdanov, Polina Gorkh, Vladyslav Rozov and Konstantin Vachnadze who helped me with proofreadings and supported me.

I would like to thank my family: my father Alexander, my mother Larisa, my aunt Tatjana and sister Nataliia. They supported me spiritually throughout working on this thesis and my life in general.

TABLE OF CONTENTS

1 Introduction

The word stochastic comes from the Greek word "$\sigma\tau\acute{o}\chi o\zeta$" (stokhos), which can be translated as "aim". "Stochastic" means being or having a random variable. Stochastic models in physics and engineering are used in phenomena with scale separation. In fluid dynamics, scale separation occurs due to the different characteristic times and characteristic lengths. In this thesis, I consider two examples of fluid dynamics phenomena where stochastic models are used: thermal fluctuations and turbulent flows. Thermal fluctuations appear due to collisions of molecules. Results of molecular collisions can influence the behavior of liquids beyond the characteristic time and length scales of molecular collisions. Turbulent flows are characterized by the random motion on a wide range of timescales and length scales. The common way to model turbulent flows is to separate scales of the mean-field velocity and fluctuating small-scale velocity. Stochastic models are used to represent the behavior of subgrid-scales in turbulent flows.

Stochastic models in fluid dynamics allow for taking into account for multiple possible outcomes and in this sense, are superior to deterministic models. In stochastic models, one has to consider average characteristics and probabilities of outcomes. In certain cases, the probabilities can be derived analytically. To extend stochastic models to a wider range of cases, suitable numerical algorithms have to be developed. The numerical algorithms that are used for deterministic models might not accurately represent the statistical properties of stochastic models and the development of new algorithms is of interest.

In this thesis, I present an overview of the stochastic models that are used in engineering and physical applications to describe thermal fluctuations and turbulent flows. This is followed by the general description of statistical characteristics that can be used to analyze the stochastic models in fluid dynamics. In the second chapter, several stochastic models are described in more detail with corresponding numerical algorithms and statistical characteristics for each model. In the third chapter, the accomplishments are provided.

1.1 Motivation

Navier-Stokes equations describe conservation of mass, momentum and energy in fluids [1, 2]. Navier-Stokes equations are partial differential equations which represent a wide range of phenomena in fluid dynamics. Navier-Stokes equations are limited to large scales of fluids. On small scales, where thermal fluctuations and diffusion of molecules are important, Navier-Stokes equations might be inaccurate. An accurate method to account for such small-scale phenomena is the deterministic model of molecular dynamics (MD). In MD, a simplified, coarse-grained model of molecules is used. The molecules interact with certain forces. These forces sometimes can be measured in experiments or deduced from more detailed, quantum mechanical description. As MD is itself a simplified model of quantum mechanics, it represents the motion of one single molecule only with a certain degree of accuracy. However, for the collective motion of molecules, MD shows accurate results [3, 4]. The main drawback of the MD method is the large computational cost of simulations.

Navier-Stokes equations describe motion of fluids on large scales and MD model describes the motion of fluids on small scales. A certain gap exists between descriptions of large and small scales. In this gap, Navier-Stokes equations are not valid and MD description is too slow, even for the modern computational methods. Two different approaches exist for filling this gap: top-down and bottom-up. The top-down approach suggests an extension of Navier-Stokes equations to model phenomena beyond the limit of Navier-Stokes equations. The following stochastic models can be associated with the top-down approach: Landau-Lifshitz Navier-Stokes equations, smoothed dissipative particle dynamics and stochastic models for turbulent flows. The bottom-up approach constitutes coarse-graining of MD. The models that are associated with the bottom-up approaches are dissipative particle dynamics, multiparticle collision dynamics or stochastic rotation dynamics and lattice-Boltzmann method. Stochastic models are used in both top-down and bottom-up approaches.

The first stochastic model for fluid dynamics phenomena was introduced in 1908 by Paul Langevin [5]. The Langevin model serves to describe Brownian motion, which is the random movement of a particle due to collisions with smaller molecules. Years later, another remarkable work of Landau and Lifshitz suggested an extension of the Navier-Stokes (NS) equations with a stochastic term to account for thermal fluctuations [1]. The stochastic term is added to NS equations to satisfy fluctuation-dissipation balance [6]. The extended

version of NS equations is usually referred in the literature as the Landau-Lifshitz Navier-Stokes (LLNS) equations. In addition to the modeling of thermal fluctuations, stochastic models are also used to study other complex phenomena in fluids. Generalized Langevin model (GLM) for turbulent and reactive flows was introduced in 80-es [7, 8, 9]. In GLM, the mean flow is driven by averaged NS equations, and NS equations are resolved with finite volume or finite difference approaches [10, 11]. A modified version of Langevin equations is used as a subgrid-scale model. In GLM, Langevin equations and NS equations are coupled with each other. With development of computers, many models were introduced to fill out the gap between MD and NS: Direct simulation Monte-Carlo (DSMC) [12, 13, 14], dissipative particle dynamics (DPD) [15, 16], smoothed dissipative particle dynamics (SDPD) [17, 18, 19]. Models differ by the length scales and cases of application as well as types of discretizations.

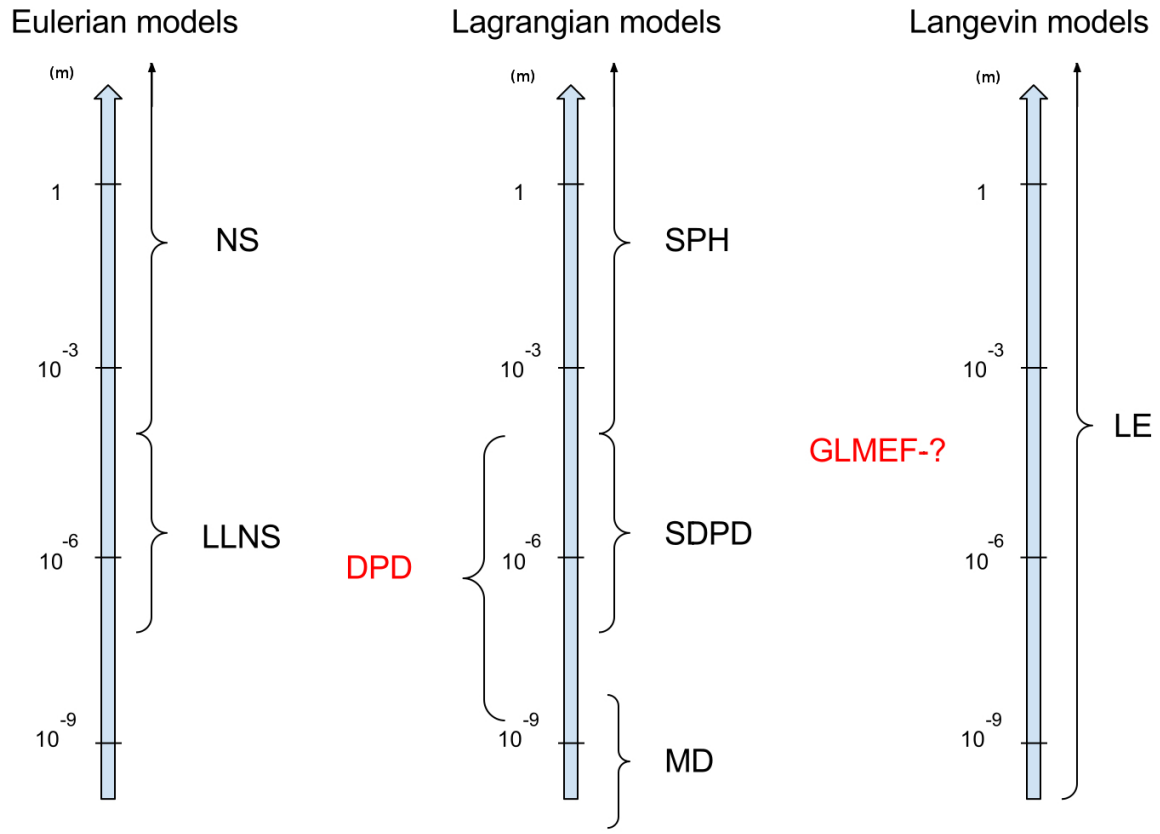

Figure 1.1: Scheme of models in hydrodynamics depending on length scales. Dimension of length scales is in meters. Red color mark the models which are considered in more details in the thesis. Generalized Langevin model in Eulerian reference frame (GLMEF) has a question mark as the application range is not yet well defined.

In models for fluid dynamics, two different types of discretization exist: Lagrangian and Eulerian. The Eulerian type is based on grid representation. Corresponding equations in the Eulerian type of models are represented in the grid points. The grid points can change in time, for example, adapting to flow field. However, grid points always preserve the certain spatial structure. In the Lagrangian type, which is sometimes referred to as meshless, the flow is represented by particles. Values of corresponding fields are attached to positions of particles. The schema of different types of stochastic models and the range of applications is depicted in Fig.1.1.

Different discretization types of the LLNS equations exist: a grid-based discretization as well as a particle discretization. In this thesis, the LLNS model is referred to the grid-based discretization of the LLNS equations. The LLNS equations can be derived by several analytical approaches for equilibrium fluctuations [1, 20, 21, 22]. For nonequilibrium thermal fluctuations, the validity of the LLNS equations was shown [23] and compared with molecular dynamics simulations [24, 25, 26]. The LLNS model was used for the description of breakup of nanojets [27, 28] and collapsing nanobridges [29], to represent thermal fluctuations in argon and water [30] and random walk of standing shocks [31]. Further improvement of numerical methods allowed to implement the LLNS model to represent the phenomena of giant fluctuations in fluids [32, 33, 34]. The phenomenon occurs when one considers gradient in concentration field with the presence of thermal fluctuations in microgravity conditions. The nature of the giant fluctuations is reversible and is related to advection by velocity fluctuations. The LLNS model is used to speed up numerical algorithm of MD [35] where the LLNS model was coupled with MD simulation of protein in the hybrid algorithm. In this setup, the LLNS model represents the outer level, while the layer of liquid around protein, as well as protein itself, are represented with MD. Moreover, the LLNS model was used to study Rayleigh-Taylor instability [36]. Recently, an algorithm for fluid-structure interaction for the LLNS model [37], which is able to significantly extend the range of application of the LLNS model, was developed.

Smoothed particle hydrodynamics (SPH) was introduced [38, 39] and is widely used as a Lagrangian approach to solve NS equations [40]. SDPD is an extension of SPH to the phenomena where thermal fluctuations are important [15, 16]. The fluctuations are added in a way to satisfy fluctuation-dissipation balance using General Equation for Non-Equilibrium Reversible-Irreversible Coupling (GENERIC) formalism [41, 42, 43]. One particle in SDPD represents a discretized piece of fluid. SDPD originates from SPH and can be considered as a particle representation of the LLNS equations [44]. SDPD model is expected to be slower, than the model that is based on grid-based the LLNS equations in a wide range of cases. However, one of the benefits of SDPD is that, due to meshless properties, it is well-suited for phenomena with complex geometries. SDPD is used in simulations of DNA chains in flow [45, 46, 47, 48, 49]. In SDPD, DNA chains are modeled with connected particles. A single particle should be understood as representing the properties of "cluster" of molecules. SDPD model suspensions of colloidal particles [50, 51, 52]. SDPD is also used in simulations of flows of red blood cells to improve and model drug delivery, microvascular blood

flows, white blood cell margination in microcirculation, deterministic lateral displacement (DLD) devices for hydrodynamic size-depending separation of cells [53, 54, 55, 56].

Lattice-Boltzmann is a Eulerian model that is used to discretize Boltzmann equation. Bolzman equation is solved in statistical manner in lattices [57, 58, 59, 60, 61]. Thermal fluctuations can be added to lattice-Boltzmann model in different ways [62, 63, 64]. The derived equations can be considered as lattice-Boltzmann representation of the LLNS equations. The corresponding model was applied to investigate different phenomena with thermal fluctuations [65, 66, 67].

DPD was introduced and developed as a coarse-graining model of MD [17, 18, 19]. DPD is used to represent complex phenomena in polymers [19], colloids [68], and membranes [69]. The DPD model is similar to SDPD, as it is also a Lagrangian approach and in the limit of large scales have similar properties as the LLNS equations [70]. Though, DPD is derived using bottom-up approach and SDPD is the top-down model. One of the challenges in the DPD model is to set appropriate parameters to represent the phenomena of interest. In general case, no accurate relations between mesoscopic parameters of DPD, microscopic potential of MD and macroscopic parameters of NS equations exist. Despite the numerous efforts to derive such relations [70, 71, 72, 73], theory is still under development. The current progress is related to implementation of Mori-Zwanzig formalism [74, 75, 76], which allows to derive coarse-grained model of star polymer melt [77]. Another improvement of the DPD model is related to energy conservative formulation [78, 79, 80].

It is possible to implement the bottom-up approach to Boltzmann equation to derive the model for hydrodynamics with thermal fluctuations. The DSMC proposed by Bird [12, 13, 14] is an example of such model. The DSMC model is a powerful tool in solving flows with high Knudsen number (Kn), in which length scales of interest are comparable with the mean-free path of gas molecules. An extended version of DSMC to represent thermal fluctuations in fluids was introduced in [81]. The new model was denoted multiparticle collision dynamics (MPCD) or stochastic rotation dynamics (SRD) [82, 83, 84] and is used as a coarse-grained model in fluids.

Langevin model was introduced for a description of Brownian motion [5]. Two forces act on the Langevin particle: the dissipative force represents a friction of Brownian particle with media and the random force represents collisions with liquid molecules. Fokker-Planck equation describes the evolution of probability density function of the velocity of a Brownian particle in time [85, 86]. Joint-PDF of velocity and position of a Brownian particle can be derived from Fokker-Planck equation [87, 88]. For the last centuries, Langevin equations were applied to the different aspects of fluid dynamics. Though, beyond the modeling of Brownian motion [89, 90, 91], Langevin model is used to describe the motion of molecules. The method was denoted as Brownian Dynamics [92]. Langevin model is used as a thermostat for MD simulations allowing to speed up numerical algorithms [93, 94]. Langevin model can be used for complex non-linear phenomena in fluid dynamics, such as turbulent and reactive flows [7, 8, 95] and polydisperse turbulent two-phase flows [96].

To analyze stochastic models in this thesis, I consider different statistical characteristics that can be measured in simulations. The method to evaluate the characteristics is similar for the considered stochastic models. For certain stochastic models, the analytical expressions for such characteristics can be derived. The definitions of the characteristics are provided in the next section.

1.2 Characteristics of Stochastic Models

Stochastic models deal with random variables. The probability density function (PDF) is the main characteristic of a random variable. PDF $f(x)$ of a continuous random variable can be defined from cumulative distribution function [97]

$$f(x) = \lim_{h \to 0} \frac{F(x+h) - F(x)}{h} \tag{1.1}$$

where $F(x) = P(X \leq x)$ is the cumulative distribution function of continuous variable. Average and variance of this random variable are given by

$$\langle A \rangle \equiv \int_{-\infty}^{\infty} f(V,t) V dV \ , \tag{1.2}$$

$$\langle (A - \langle A \rangle)^2 \rangle \equiv \int_{-\infty}^{\infty} f(V,t)(V - \langle A \rangle)^2 dV \ . \tag{1.3}$$

Here operator $\langle \bullet \rangle$ is defined by equations (1.2). In experiments and simulations, the averaging can be used in the different ways [97]. One can measure mean value in stationary process (over a time interval T) as

$$\langle A \rangle_T \equiv \frac{1}{T} \int_t^{t+T} A(t) dt \ . \tag{1.4}$$

If the experiment can be repeated multiple times N, then average in ensemble is

$$\langle A \rangle_N \equiv \frac{1}{N} \sum_{n=1}^{N} A^n(t) \ . \tag{1.5}$$

The common situation is that considered system has more than one random variables, which are correlated. Let us consider the system with two random dependent variables $A_1(t)$, $A_2(t)$. Such system can be described with a joint-PDF function $P(A_1, A_2, t)$, which is the probability that A_1 and A_2 will take certain values simultaneously in time t. The other important characteristic is a conditional PDF $P(A_1, t|A_2)$. It is the probability stated

that variable A_1 will take the certain value in time t, given that the second variable took value A_2. The relation of joint-PDF and conditional PDF is given by [97]

$$P(A_1, A_2, t) = P(A_1, t|A_2)P(A_2) \ .$$

The joint-PDF of all variables in the model is the most general characteristic of the model. When the joint-PDF is determined, one can derive corresponding mean characteristics by averaging, which is defined similarly to the eq. 1.2. A numerical algorithm has to correctly represent the joint-PDF of all variables of the model. However, joint-PDF is a bad candidate to rely on in analysis as it is hard to measure in experiments and can be derived analytically only in the certain cases. In the next three sections, other statistical characteristics are considered: stationary PDF, static structure factor, dynamic structure factor and current autocorrelation functions.

1.2.1 Stationary Probability Density Function

Stationary PDF $P(A)$ can be defined as a limit of PDF $P(A, t)$ in time

$$P(A) = \lim_{t\to\infty} P(A, t) \ .$$

Stationary PDF of velocity and density fields can be derived for a wide range of stochastic models in fluid dynamics. If stationary PDF is Gaussian, it is characterized solely by mean value $\lim_{t\to\infty}\langle A(t)\rangle$ and variance $\lim_{t\to\infty}\langle A(t) - \langle A(t)\rangle^2\rangle$. Stationary PDF of certain characteristics can be estimated in experiments [98, 99, 100].

1.2.2 Current Autocorrelation Functions

Current autocorrelation functions (CACF) can be determined in simulations for stochastic models both in Eulerian and Lagrangian reference frames. To compute CACF in simulation, every certain time period velocity field $\boldsymbol{u}(x, y, z)$ is transformed to Fourier space $\hat{\boldsymbol{w}}(q_x, q_y, q_z)$. Different notation in $\boldsymbol{u}$ and $\boldsymbol{w}$ emphasize the difference between current and velocity fields. The velocity field $\boldsymbol{u}$ might be represented in both Eulerian and Lagrangian reference frames. The current field $\boldsymbol{w}$ is attached to the Eulerian reference frame. Autocorrelation of derived Fourier modes of the current field is evaluated. One can distinguish two different kinds of CACF: longitudinal (LCACF) and transverse (TCACF). In 3D domain three LCACF are

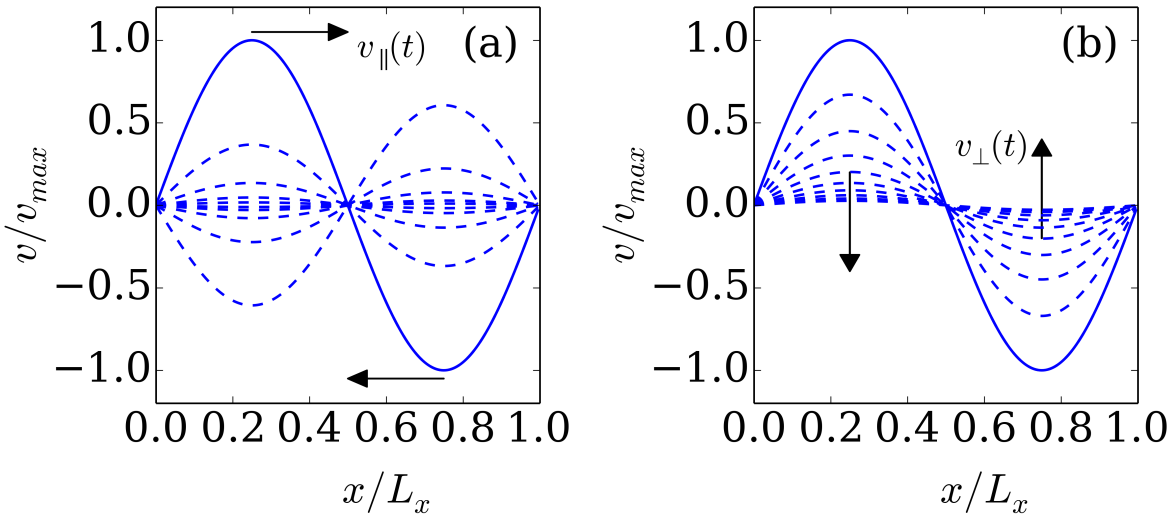

Figure 1.2: The decay of initial sinusoidal wave in velocity field. In the left figure, the initial sinusoidal wave is set parallel to the velocity direction, which formally corresponds to longitudinal current autocorrelation functions (LCACF). In the right figure, perpendicular sinusoidal wave corresponds to transversal current autocorrelation functions (TCACF).

$$C_\parallel(q_x,t) = \frac{\langle \hat{w}_x(q_x,0)\hat{w}_x(q_x,t)\rangle}{\delta\hat{w}_x^2(q_x,0)}\ , C_\parallel(q_y,t) = \frac{\langle \hat{w}_y(q_y,0)\hat{w}_y(q_y,t)\rangle}{\delta\hat{w}_y^2(q_y,0)}\ ,$$
$$C_\parallel(q_z,t) = \frac{\langle \hat{w}_z(q_z,0)\hat{w}_z(q_z,t)\rangle}{\delta\hat{w}_z^2(q_z,0)}\ , \tag{1.6}$$

and six different TCACF are

$$\begin{aligned}
C_{xy\perp}(q_x,t) &= \frac{\langle \hat{w}_y(q_x,0)\hat{w}_y(q_x,t)\rangle}{\delta\hat{w}_y^2(q_x,0)}\ , C_{xz\perp}(q_x,t) = \frac{\langle \hat{w}_z(q_x,0)\hat{w}_z(q_x,t)\rangle}{\delta\hat{w}_z^2(q_x,0)}\ ,\\
C_{yz\perp}(q_y,t) &= \frac{\langle \hat{w}_z(q_y,0)\hat{w}_z(q_y,t)\rangle}{\delta\hat{w}_z^2(q_y,0)}\ , C_{yx\perp}(q_y,t) = \frac{\langle \hat{w}_x(q_y,0)\hat{w}_x(q_y,t)\rangle}{\delta\hat{w}_x^2(q_y,0)}\ ,\\
C_{zy\perp}(q_z,t) &= \frac{\langle \hat{w}_y(q_z,0)\hat{w}_y(q_z,t)\rangle}{\delta\hat{w}_y^2(q_z,0)}\ , C_{zx\perp}(q_z,t) = \frac{\langle \hat{w}_x(q_z,0)\hat{w}_x(q_z,t)\rangle}{\delta\hat{w}_x^2(q_z,0)}\ .
\end{aligned} \tag{1.7}$$

CACF are widely used in the analysis of stochastic models and MD. In the LLNS equations and GLM, CACF can be derived analytically and are used to verify corresponding numer-

ical algorithms [30, 31, 101, 102]. In MD and DPD, the corresponding CACF are hard to derive analytically and can be used to link the models with each other and choose appropriate parameters to improve the prediction accuracy of the models [98, 103, 104, 105, 106]. CACF is similar to the ensemble-averaged decay of an initially sinusoidal field to steady state. In Fig. 1.2 two different cases of the initial sinusoidal wave of the velocity field are shown. The case where the direction of the sinusoidal wave is parallel to the initial velocity corresponds to the LCACF, represented in Fig. 1.2a. Fig. 1.2b corresponds to the TCACF.

1.2.3 Dynamic and Static Structure Factors

Dynamic structure factor (DSF) is a time-dependent spectrum characteristic. DSF of density field and temperature can be measured in experiments with incoherent neutron scattering or Rayleigh scattering of light [98, 99, 100].

One can follow [107] and consider general linear stochastic partial differential equation (SPDE) for the field $\boldsymbol{U}(\boldsymbol{r},t) \equiv \boldsymbol{U}(t)$ in Eulerian reference frame of the form

$$d\boldsymbol{U}(t) = \boldsymbol{L}\boldsymbol{U}(t)dt + \boldsymbol{K}\boldsymbol{W}(\boldsymbol{r},t) \ , \tag{1.8}$$

where time-independent linear operators $\boldsymbol{L}$ is a generator, $\boldsymbol{K}$ is a filter. $\boldsymbol{W}(t)$ is a spatiotemporal white noise

$$\langle \boldsymbol{W}(\boldsymbol{r},t)\boldsymbol{W}^{\star}(\boldsymbol{r}',t')\rangle = \delta(t-t')\delta(\boldsymbol{r}-\boldsymbol{r}') \ . \tag{1.9}$$

Then DSF is [107]

$$\boldsymbol{S}(\boldsymbol{q},\omega) = V\left\langle \hat{\boldsymbol{U}}(\boldsymbol{q},\omega)\hat{\boldsymbol{U}}^{\star}(\boldsymbol{q},\omega)\right\rangle = (\hat{\boldsymbol{L}}(\boldsymbol{q}) - i\omega\boldsymbol{I})^{-1}(\hat{\boldsymbol{K}}\hat{\boldsymbol{K}}^{\star})(\hat{\boldsymbol{L}}^{\star}(\boldsymbol{q}) + i\omega\boldsymbol{I})^{-1} \ . \tag{1.10}$$

where $\hat{\bullet}$ denotes fourier-space transform. Static structure factor (SSF) comes by integration over ω of dynamic structure factor

$$\boldsymbol{S}(\boldsymbol{q}) = \frac{1}{2\pi}\int_{-\infty}^{+\infty} \boldsymbol{S}(\boldsymbol{q},t)d\omega \ , \tag{1.11}$$

The fluctuation dissipation balance can be written [6]

$$\boldsymbol{L} + \boldsymbol{L}^{\star} = \boldsymbol{K}\boldsymbol{K}^{\star} \ , \tag{1.12}$$

which ensures that SSF is equal to unity matrix

$$\boldsymbol{S} = \boldsymbol{I} \ . \tag{1.13}$$

In stochastic models of the Lagrangian type, static structure factor resembles the behavior of radial distribution function. For both the Lagrangian and the Eulerian types of stochastic models dynamic structure factor resembles CACF behavior [98].

2 Analysis and Numerical Algorithms

In this chapter, the overview of several stochastic models is provided. In the description of every model, corresponding statistical characteristics such as stationary PDF, CACF and SSF are listed with numerical algorithms. In this thesis, I restrict my attention to the algorithms for modeling of homogeneous fluids. The chapter only partly covers numerical algorithms which are used to simulate complex boundary conditions and complex fluids, such as polymers, membranes, colloids etc. The description of numerical algorithms and models of the lattice-Boltzmann method and MPCD/SRD models is beyond the scope of this thesis.

2.1 Stochastic Integration

Stochastic integration demands special consideration. The most widespread stochastic calculus are Ito and Stratonovich. In the following subsections, I provide a brief overview of these calculus. More detailed explanation can be found in [108, 109, 110, 111, 112, 113].

For a function $f(t)$ of time t and a Wiener process $W(t)$ with properties [108]

$$\langle dW_t \rangle = 0, \quad \langle (dW_t)^2 \rangle = dt, \quad \langle (dW_t)^n \rangle = o(dt) \ , \tag{2.1}$$

Riemann-Stieltjes definition of an integral constitutes

$$\int_0^t f(t)dW(t) = \lim_{n\to\infty} \sum_{j=1}^{n} f(\tau_j)(W(t_{j+1}) - W(t_j)) \ , \tag{2.2}$$

where $\tau_j \in [t_j, t_{j+1}]$. For smooth $f(t)$ one does not need any stochastic modification. In SPDEs $W(t)$ is not smooth, continuous and non-differentiable variable with unbounded variation in any interval. For that reason, the limits which define the integral depends on where τ_j is taken. Different choices correspond to different stochastic calculus.

- $\tau_j = t_j$ is Ito calculi
- $\tau_j = \frac{1}{2}(t_j + t_{j+1})$ is Stratonovich calculi

It is easy to show the difference of Stratonovich and Ito calculus on the simple example [108]. Let us consider $\int_0^t W(t')dW'(t')$. According to definition (2.2) the results for different stochastic calculus are

- Ito integration

$$I = \int_0^t W(t')dW'(t') = \frac{1}{2}\left[W(t)^2 - W(0)^2 - t\right] \ . \tag{2.3}$$

- Stratonovich integration

$$I = \int_0^t W(t')dW'(t') = \frac{1}{2}\left[W(t)^2 - W(0)^2\right] \ . \tag{2.4}$$

2.1.1 Ito integration

Ito integral is defined similar to Riemann-Stieltjes integral, however taking the function at the beginning of partial sums. Stochastic integral is defined as a mean square limit [108]

$$\int_{t_0}^t f(t')dW(t') = ms - \lim_{n\to\infty} \sum_{j=1}^{n} f(t_j)(W(t_{j+1}) - W(t_j)) \ . \tag{2.5}$$

Velocity Verlet algorithm

Stochastic Velocity Verlet algorithm [114, 115] is of Ito form. The basic idea is to write forward and backward third-order expansion of particle position in time

$$\boldsymbol{r}(t+\Delta t) = \boldsymbol{r}(t) + \boldsymbol{v}(t)\Delta t + \frac{1}{2}a(t)\Delta t^2 + \frac{1}{6}b(t)\Delta t^3 + O(\Delta t^4) \ ,$$
$$\boldsymbol{r}(t-\Delta t) = \boldsymbol{r}(t) - \boldsymbol{v}(t)\Delta t + \frac{1}{2}a(t)\Delta t^2 - \frac{1}{6}b(t)\Delta t^3 + O(\Delta t^4) \ ,$$

where $\boldsymbol{v}$, $\boldsymbol{a}$ and $\boldsymbol{r}$ are velocity, acceleration and position of particles, correspondingly. $\boldsymbol{b}$ is the third derivative of $\boldsymbol{r}$. The summation of the two expressions gives

$$\boldsymbol{r}(t+\Delta t) = 2\boldsymbol{r}(t) - \boldsymbol{r}(t-\Delta t) + \boldsymbol{a}(t)\Delta t^2 + O(\Delta t^4) \ . \tag{2.6}$$

The derived algorithm is denoted as Verlet algorithm. The Velocity Verlet scheme is similar to Verlet algorithm extended to velocity evaluation

$$\boldsymbol{r}(t+\Delta t) = \boldsymbol{r}(t) + \boldsymbol{v}(t)\Delta t + \frac{1}{2}\boldsymbol{a}(t)\Delta t^2 \ , \tag{2.7}$$
$$\boldsymbol{v}(t+\Delta t/2) = \boldsymbol{v}(t) + \frac{1}{2}\boldsymbol{a}(t)\Delta t \ , \tag{2.8}$$
$$\boldsymbol{a}(t+\Delta t) = -\frac{1}{m}\nabla V(\boldsymbol{r}(t+\Delta t)) \ , \tag{2.9}$$
$$\boldsymbol{v}(t+\Delta t) = \boldsymbol{v}(t+\Delta t/2) + \frac{1}{2}\boldsymbol{a}(t+\Delta t)\Delta t \ . \tag{2.10}$$

Acceleration term $a(t)$ usually includes deterministic F_D and stochastic forces F_s

$$a(t) = F_D + F_s \ . \tag{2.11}$$

The Velocity Verlet algorithm is used in Lagrangian methods, such as MD, DPD, SDPD, etc.

2.1.2 Stratonovich integration

Stratonovich integral is defined as [108]

$$\int_{t_0}^{t} f(x(t'),t') \circ dW(t') = ms - \lim_{n\to\infty} \sum_{j=1}^{n} f\left(\frac{1}{2}\left(x(t_j)+x(t_{j-1})\right), t_{j-1}\right)\left(W(t_{j+1})-W(t_j)\right) . \tag{2.12}$$

In Stratonovich integration, the ordinary rules of calculus is valid for change of variables [108].

Third-order Runge-Kutta method

Third-order Runge-Kutta variance-preserving method is used to integrate stochastic differential equations in the Eulerian reference frame in time. It is based on a strongly stable (for deterministic equations) Runge-Kutta temporal integrator (RK3) [116, 117]. It accurately reproduces dynamic and static structure factors for advection-diffusion equation and for the isothermal LLNS equations. [31, 107, 118] The integration allows generating noise field only two times for one timestep.

RK3 for the equation of the type of the eq. (1.8) has three substeps given by equations

$$\boldsymbol{U}^{n+1/3} = \boldsymbol{U}^{n} - dtd\boldsymbol{U}^{n} + \sqrt{dt}\boldsymbol{K}^{n} , \tag{2.13}$$

$$\boldsymbol{U}^{n+2/3} = \frac{3}{4}\boldsymbol{U}^{n} + \frac{1}{4}\boldsymbol{U}^{n+1/3} - \frac{1}{4}dtd\boldsymbol{U}^{n+1/3} + \sqrt{dt}\boldsymbol{K}^{n+1/3} , \tag{2.14}$$

$$\boldsymbol{U}^{n+1} = \frac{1}{3}\boldsymbol{U}^{n} + \frac{2}{3}\boldsymbol{U}^{n+2/3} - \frac{2}{3}dtd\boldsymbol{U}^{n+2/3} + \sqrt{dt}\boldsymbol{K}^{n+2/3} , \tag{2.15}$$

where $d\boldsymbol{U}$ is the solution vector, and $\boldsymbol{K}$ is the stochastic-force vector. There are several possibilities for evaluating $\boldsymbol{K}$ at intermediate time steps [107, 118]. The following formulation requires only two independent random fields ($\boldsymbol{W}_A$ and $\boldsymbol{W}_B$)

$$\boldsymbol{K}^{n+1/3} = \alpha_1\boldsymbol{W}_A + \beta_1\boldsymbol{W}_B , \quad \boldsymbol{K}^{n+2/3} = \alpha_2\boldsymbol{W}_A + \beta_2\boldsymbol{W}_B , \quad \boldsymbol{K}^{n+1} = \alpha_3\boldsymbol{W}_A + \beta_3\boldsymbol{W}_B , \tag{2.16}$$

with the coefficients

$$\begin{aligned} \alpha_1 = \alpha_2 = \alpha_3 = 1,\ \beta_1 = \frac{2\sqrt{2} \pm \sqrt{3}}{5}, \\ \beta_2 = \frac{-4\sqrt{2} \pm 3\sqrt{3}}{5},\ \beta_3 = \frac{\sqrt{2} \mp 2\sqrt{3}}{10}\ . \end{aligned} \tag{2.17}$$

For multiplicative noise, when prefactor of noise changes in time, the scheme might be inaccurate and has to be extended.

2.2 Grid-Based Landau-Lifshitz Navier-Stokes model

The LLNS model is based on the solution of the LLNS equations with the Eulerian method of discretization. The LLNS equations are a stochastic extension of Navier-Stokes equations [99]

$$\frac{\partial \rho}{\partial t} + \nabla \cdot \rho \boldsymbol{u} = 0\ , \tag{2.18}$$

$$\frac{\partial \boldsymbol{g}}{\partial t} + \nabla \cdot (\rho \boldsymbol{u}\boldsymbol{u} - \boldsymbol{\sigma} - \boldsymbol{\sigma}_S) = 0\ , \tag{2.19}$$

$$\frac{\partial e}{\partial t} + \nabla \cdot (\boldsymbol{Q} + e\boldsymbol{u} - \boldsymbol{u} \cdot \boldsymbol{\sigma} - \boldsymbol{u} \cdot \boldsymbol{\sigma}_S) = 0\ , \tag{2.20}$$

where e is total energy, $\boldsymbol{\sigma}$ and $\boldsymbol{\sigma}_S$ are a deterministic and a stochastic stress tensors, respectively. We consider the fluid with Newtonian properties. Stress tensor of such a fluid is given by equation

$$\sigma_{ij} = p\delta_{ij} - \eta_s(\nabla_i u_j + \nabla_j u_i - \frac{2}{3}\nabla \cdot \boldsymbol{u}\delta_{ij}) + \eta_v \nabla \cdot \boldsymbol{u}\delta_a ij\ , \tag{2.21}$$

where η_s and η_v are shear and bulk viscosities, respectively. Diffusive part of energy flux $\boldsymbol{Q}$ is

$$\boldsymbol{Q} = -\lambda \nabla T\ . \tag{2.22}$$

Stochastic stress tensor is Gaussian matrix with zero mean and correlation is chosen to satisfy fluctuation-dissipation theorem

$$\langle \boldsymbol{\sigma_S}(\boldsymbol{r_1}, t_1)\boldsymbol{\sigma_S}(\boldsymbol{r_2}, t_2)\rangle = 2k_B T\Delta V C_{\alpha\beta\gamma\delta}\delta(t_1 - t_2)\delta(r_1 - r_2) \ , \tag{2.23}$$

where $C_{\alpha\beta\gamma\delta} = \eta_s(\delta_{\alpha\delta}\delta_{\beta\gamma} + \delta_{\alpha\gamma}\delta_{\beta\delta}) + (\eta_v - \frac{2}{3}\eta_s)\delta_{\alpha\beta}\delta_{\delta\gamma}$ and ΔV is volume cell, which defines the level of discretization. The smaller the volume is, the higher fluctuations in velocity fields are.

The equations (2.18)–(2.23) are not closed. One needs to define the equation of state, which constitutes the dependency of pressure p from density ρ. One of the options is to consider linear dependency of pressure from density

$$p = c_T^2 \rho \ , \tag{2.24}$$

where c_T is isothermal speed of sound. With equation of state (2.24), equations (2.18)–(2.20) can be simplified to the isothermal LLNS equations

$$\frac{\partial \rho}{\partial t} + \nabla \cdot \rho \boldsymbol{u} = 0 \ , \tag{2.25}$$

$$\frac{\partial \boldsymbol{g}}{\partial t} + \nabla \cdot (\rho \boldsymbol{u}\boldsymbol{u} - \boldsymbol{\sigma} - \boldsymbol{\sigma}_S) = 0 \ . \tag{2.26}$$

Statistical characteristics

In this section, statistical characteristics of the isothermal LLNS equations are provided. Corresponding characteristics in more general case can be found in [98, 99]. Stationary PDF of density and velocity fields in the LLNS equations are Gaussian functions and are characterized by mean and variance. Variances of velocity and density field, respectively, are

$$\langle u^2 \rangle = \frac{k_B T}{\bar{\rho}} \Delta V^{-1} \ , \langle \rho^2 \rangle = \frac{\bar{\rho} k_B \bar{T}}{c_T^2} \Delta V^{-1} \ . \tag{2.27}$$

Dynamic structure factor of the isothermal LLNS equations is given by

$$S_{uu}(q, \omega) = \frac{q^2 D_v \, \omega^2}{\left(c_s{}^2 \, q^2 - \omega^2\right)^2 + q^2 D_v{}^2 \, \omega^2} \ , \tag{2.28a}$$

$$S_{\rho\rho}(q, \omega) = \frac{q^4 D_v \, c_s{}^2}{\left(c_s{}^2 \, q^2 - \omega^2\right)^2 + q^2 D_v{}^2 \, \omega^2} \ , \tag{2.28b}$$

$$S_{\rho u}(q, \omega) = S_{u\rho}(q, \omega) = 0 \ , \tag{2.28c}$$

where $D_v = \frac{4}{3}\frac{\eta_s}{\bar{\rho}} + \frac{\eta_v}{\bar{\rho}}$ is longitudinal kinematic viscosity. Static stricture factor can be obtained through integration of

$$S_{uu}(q) = \frac{1}{2\pi}\int_{-\infty}^{+\infty} S_{uu}(k,\omega)d\omega = 1 \ , \tag{2.29a}$$

$$S_{\rho\rho}(q) = \frac{1}{2\pi}\int_{-\infty}^{+\infty} S_{\rho\rho}(q,\omega)d\omega = 1 \ . \tag{2.29b}$$

Current autocorrelation function resembles behavior of dynamic structure factor

$$C_{\parallel LLNS} = e^{-q^2 D_v \frac{1}{2}\tau}\cos(c_s q\tau) - \frac{D_v q}{2c_s}e^{-q^2 D_v \frac{1}{2}\tau}\sin(c_s q\tau) \ , \tag{2.30}$$

$$C_{\perp LLNS} = e^{-q^2 D_v \frac{1}{2}\tau} \ , \tag{2.31}$$

$$C_{\rho LLNS} = e^{-q^2 D_v \frac{1}{2}\tau}\cos(c_s q\tau) + \frac{D_v q}{2c_s}e^{-q^2 D_v \frac{1}{2}\tau}\sin(c_s q\tau) \ . \tag{2.32}$$

Numerical algorithms

The isothermal LLNS equations are non-multiplicative as prefactor of the stochastic term is constant in time. For non-multiplicative case, time integration can be evaluated with explicit Stratonovich third-order Runge-Kutta scheme eqs. (2.13)-(2.17). Other time-integration schemes for stochastic partial differential equations with non-multiplicative noise were considered in [107, 118]. Though, for the small fluctuations in temperature field, multiplicity in the LLNS equations was observed to be small [31].

The LLNS is a system of stochastic partial differential equations (SPDE). For the solution of the LLNS SPDE, one has to introduce a scheme for the spatial discretization. Finite volume discretization of the isothermal LLNS equations was suggested in [30]. Different finite volume discretization methods were considered for the compressible LLNS equations in [31]. Piecewise parabolic method with Godunov scheme was shown to represent correctly the variance of velocity, density and temperature fields of the compressible LLNS equations. Furthermore, discretization based on a staggered finite-difference scheme was found superior in comparison with the schemes on the collocated grid for the LLNS equations [119]. The further development of numerical algorithms confirms the superiority of staggered finite-difference discretization over the one on the collocated grid by considering discrete static structure factor [107]. The skew-symmetric discretization originally derived for NS equations [120] was shown to give the most accurate results for static structure factor [101, 121]. The recently developed scheme uses finite-element approach to solve the LLNS equations [122], which might be beneficial in case of complex boundary conditions.

2.3 Smoothed Dissipative Particle Dynamics

SDPD is based on the second-order discretization of Navier-Stokes equations. The method is an extension of SPH model to the length scales, where thermal fluctuations are important [16].

Density of the fluid is given by

$$\rho_i = m_i \sum_j W_{ij} \ . \tag{2.33}$$

The momentum equations are discretized as

$$\frac{dv_i}{dt} = -\frac{1}{m_j}\sum_j \left(\frac{p_i}{\sigma_i^2} + \frac{p_j}{\sigma_j^2}\right)\frac{\partial W_{ij}}{\partial r_{ij}}\boldsymbol{e}_{ij} + \frac{\eta}{m_i}\sum_j \left(\frac{1}{\sigma_i^2} + \frac{1}{\sigma_j^2}\right)\frac{\boldsymbol{v}_{ij}}{r_{ij}}\frac{\partial W_{ij}}{\partial r_{ij}} + d\tilde{\boldsymbol{P}}_i \ , \tag{2.34}$$

where fluctuation term $d\tilde{\boldsymbol{P}}_i$ is derived [16] according to GENERIC formalism [41, 42, 43] and is given as

$$d\tilde{\boldsymbol{P}}_i = \sum B_{ij} d\bar{W}_{ij}\boldsymbol{e}_{ij} \ , \tag{2.35}$$

where $d\bar{W}_{ij}$ is the traceless symmetric part of an independent increment of Wiener process and B_{ij} is the corresponding fluctuating coefficient in SDPD given by

$$B_{ij} = [-4k_B T\eta]^{\frac{1}{2}} \ . \tag{2.36}$$

Statistical characteristics

Statistical characteristics of the SDPD model are similar to the LLNS equations. Stationary PDF of velocity field are Gaussian functions with variance

$$\langle v^2 \rangle = d\frac{k_B T}{\bar{\rho} V_i} \ , \tag{2.37}$$

where V_i is a particle volume, similar to a cell volume in the LLNS equations. Stationary PDF of density field depends on a choice of an equation of state. In the SDPD model, a radial distribution function is usually considered instead of a static structure factor. The radial distribution function approximates unity on the large distance r similar to SSF of

the LLNS equations. On the small distance, radial distribution function differs from the unity and is similar to one of MD simulations of liquid [49].

For the dynamic statistical characteristics, such as DSF and CACF, one would expect similar behavior as in the LLNS equations, that is described in Section 2.2.

Numerical algorithms

SDPD is a meshless Lagrangian approach. In contrast to Eulerian frame methods, it does not need additional discretization of non-linear term. The quintic weighting function, that gives the best convergence properties for SPH discretization of NS equations [123] is usually chosen [49, 52] for the SDPD simulations.

Time integration of Lagrangian methods is usually done with Ito type of time integration. In the SDPD simulations, Velocity Verlet algorithm can be used. Timestep integration can be improved with implicit numerical scheme for SDPD [124, 125].

2.4 Langevin model in the Lagrangian reference frame

Langevin models are represented with Langevin equations. The Langevin equations (LE) state

$$\dot{\boldsymbol{x}}_{\boldsymbol{i}} = \boldsymbol{v}_{\boldsymbol{i}} \ , \tag{2.38}$$

$$\dot{\boldsymbol{v}}_{\boldsymbol{i}} = -\beta \boldsymbol{v}_{\boldsymbol{i}} + \boldsymbol{\theta}_{\boldsymbol{i}}(t) \ , \tag{2.39}$$

where $i, j = 1, 2, 3..., N$ for N particles that are governed by LE. Here a dissipation coefficient β is constant and $\theta_{i,k}$ is a delta-correlated in time Gaussian random variable

$$\langle \theta_{i,k}(t) \rangle = 0 \ , \tag{2.40}$$

$$\langle \theta_{i,k}(t) \theta_{j,l}(t') \rangle = \frac{2 k_B T \beta}{m} \delta_{ij} \delta_{kl} \delta(t - t') \ , \tag{2.41}$$

where $k, l = x, y, z$, k_B is the Boltzmann constant, T is the temperature and m is the mass of the Brownian particle. Modified version of LE is used as subgrid scale model in turbulent flows [7, 8, 95]. LE are also used in modeling of rarefied gasses in the case of low Knudsen number [126, 127].

Statistical characteristics

The most general way to describe the properties of LE is through its conditional joint-PDF $P(\boldsymbol{v}, \boldsymbol{x}, t|\boldsymbol{v_0})$, which is the probability of the particle with the initial velocity $\boldsymbol{v}(t = 0, \boldsymbol{x} = 0) = \boldsymbol{v_0}$ that is situated in $\boldsymbol{x_0}$ to be at time t in $\boldsymbol{x}$ with velocity $\boldsymbol{v}$. The expression for conditional joint-PDF of Langevin equations for d-dimensions [88] is

$$P(\boldsymbol{v}, \boldsymbol{x}, t|\boldsymbol{v_0}) = Z_p \exp\Big[- \frac{A\boldsymbol{V}\cdot\boldsymbol{V} + 2C\boldsymbol{V}\cdot\boldsymbol{X} + B\boldsymbol{X}\cdot\boldsymbol{X}}{2(AB - C^2)}\Big] \ , \tag{2.42}$$

$$Z_p = \frac{e^{\beta t d}}{(2\pi)^d (AB - C^2)^{\frac{d}{2}}} \ , \tag{2.43}$$

$$\boldsymbol{V} = e^{\beta t}\boldsymbol{v} - \boldsymbol{v_0}, \quad \boldsymbol{X} = \boldsymbol{x} + \boldsymbol{u}/\beta - \boldsymbol{x_0} - \boldsymbol{v_0}/\beta \ , \tag{2.44}$$

$$A = 2\frac{k_B T}{m}\beta^{-2} t \ , \quad B = \frac{k_B T}{m}\beta^{-1}(e^{2\beta t} - 1) \ , \quad C = -2\frac{k_B T}{m}\beta^{-2}(e^{\beta t} - 1) \ . \tag{2.45}$$

For the further analysis, it is enough to consider only one direction x. The corresponding equations for other directions y, z are equivalent. The marginal PDFs result from definition after integration of the joint-PDF

$$P_x(x, t|v_{x0}) = \int_{-\infty}^{\infty} P(v_x, x, t|v_{x0}) dv \ ,$$
$$P_v(v_x, t|v_{x0}) = \int_{-\infty}^{\infty} P(v_x, x, t|v_{x0}) dx \ .$$

The Maxwell-Boltzmann distribution can be derived from the joint-PDF

$$G(v_x) = \lim_{t\to\infty} P_v(v_x, t|v_{x0}) \ ,$$
$$G(v_x) = \sqrt{2\pi\frac{k_B T}{m}} \exp\Big[- \frac{m}{2k_B T} v_x^2\Big] \ . \tag{2.46}$$

Expressions for the CACF were derived in [128]. TCACF, LCACF and density current autocorrelation functions, respectively, are

$$C_{LE\perp} = \exp\Big[-\beta t\Big] \times \exp\Big[-\frac{q^2 k_B T}{\beta^2 m}\big(\beta t - 1 + e^{-\beta t}\big)\Big]\,, \tag{2.47}$$

$$C_{LE\parallel} = \Big(e^{\beta t} - q^2\big(\frac{k_B T}{\beta^2 m}\big)(e^{\beta t}-1)^2\Big)\times$$
$$\exp\Big[-2\beta t\Big]\exp\Big[-\frac{q^2 k_B T}{\beta^2 m}(\beta t - 1 + e^{-\beta t})\Big]\,, \tag{2.48}$$

$$C_{LE\rho} = \exp\Big[-\frac{q^2 k_B T}{\beta^2 m}(\beta t - 1 + e^{-\beta t})\Big]\,. \tag{2.49}$$

Numerical algorithms

Velocity-Verlet can be used to perform integration in time. Another option is to use semi-implicit algorithm for integration in time, which gives similar accuracy with higher Current-Levi-Friedrich (CFL) number [126], and conserves kinetic energy. Other time integration schemes can be found in [129].

2.5 Langevin models in Eulerian reference frame

The certain correspondence between the Eulerian frame PDF and the Lagrangian frame PDF of Langevin models exists [97]. Moreover, Fokker-Planck equation that represents an evaluation of PDF in time is similar for the Lagrangian and the Eulerian PDF for Langevin equations [97]. Solution of Fokker-Planck equation directly takes a large amount of computational resources and is seldom used in modeling. Usually, Fokker-Planck equation is solved by means of corresponding stochastic differential equation (SDE) in the Lagrangian reference frame. In Generalized Langevin Model (GLM), Langevin equations in the Lagrangian reference frame are used as a subgrid-scale model for turbulent flows [97] and large scales are represented by NS equations in the Eulerian reference frame. The hybrid Lagrangian-Eulerian approach has shown to be successful in the modeling of turbulent and reactive flows [95, 96]. One of the possibilities to improve an accuracy of GLM and reduce computational costs is to use the Eulerian reference frame for Langevin equations.

The main challenge arises from numerical solution of Langevin equations in the Eulerian reference frame. The derived SPDE has the nonlinear term that has to be discretized. However, in contrast to the LLNS equations, Langevin equations in the Eulerian reference

frame have no viscosity and no pressure term. Due to this difference, the common algorithms that are used for the solution of Navier-Stokes equations can not be implemented without additional modifications.

Recently, two methods were proposed to solve Langevin equations in the Eulerian reference frame: Eulerian Monte-Carlo (EMC) method and Generalized Langevin model in the Eulerian reference frame (GLMEF). In EMC, SPDE that are statistically equivalent to the Langevin equations in the Lagrangian reference frame are considered [130, 131]. In GLMEF, additional pressure term to SPDE [132] is introduced. The additional term simplifies numerical algorithm, however, the derived equations are not statistically equivalent to the Langevin equations in Lagrangian reference frame [102].

Another difference between the two methods is due to the different way of introducing stochastic term. In EMC method the noise term is delta-correlated in time and constant in space. Such approach demands to solve simultaneously around $N_s = 500$ equations [133]. Each equation represents one smooth realization of the stochastic field which is shifted in comparison with other realizations of the same value in the whole domain. PDF is evaluated by the means of Favre averages. In GLMEF the noise term is introduced as delta-correlated in time and in space. In the next Section, the EMC method is provided. GLMEF numerical algorithm and statistical characteristics are described in the first paper in Appendix A.

2.5.1 Eulerian Monte Carlo method

EMC model has been proposed for solving one-time one-point velocity PDF transport equation [130, 131, 134]. The one-dimensional EMC subgrid scale model can be written for fluctuating velocity u'' by

$$\frac{\partial \rho}{\partial t} + \frac{\partial \rho u''}{\partial x} = 0 \ , \tag{2.50}$$

$$\frac{\partial \rho u''}{\partial t} + \frac{\partial \rho u''^2}{\partial x} = \frac{\rho}{\overline{\rho}} \frac{\partial \overline{\rho u''^2}}{\partial x} + \rho C_1 \omega u'' + \rho \sqrt{C_0 \epsilon} \xi \ , \tag{2.51}$$

where ρ is a stochastic density, $\overline{\rho}$ is a mean density, C_1 and C_0 are model constants, ω and ϵ is a mean turbulent frequency and a mean turbulent energy dissipation [97].

Statistical properties

Statistical properties of EMC are similar to the Lagrangian Langevin equations, described in Section 2.4.

Numerical algorithm

In EMC 2.50, 2.51, special multivariate solution has to be considered [133]. The algorithm to solve EMC was proposed in [135] and was tested for one-dimensional PDF.

2.5.2 Generalized Langevin model in Eulerian reference frame

The GLMEF in one dimension consitutes [102]

$$\frac{\partial \rho(x,t)}{\partial t} + \frac{\partial g(x,t)}{\partial x} = 0 \tag{2.52a}$$

$$\frac{\partial g(x,t)}{\partial t} + \frac{\partial}{\partial x}\frac{g^2(x,t)}{\rho(x,t)} = -\frac{\partial p(x,t)}{\partial x} - \gamma\rho(x,t)\left(u(x,t) - u_0(x,t)\right) + \sqrt{\rho(x,t)D\gamma}\zeta(x,t)\ , \tag{2.52b}$$

with the weakly compressible equation of state

$$p(x,t) = \rho(x,t)c_s^2\ . \tag{2.52c}$$

In these equations $\rho(x,t)$ and $p(x,t)$ denote mass density and pressure fields, respectively, $g(x,t) = \rho(x,t)u(x,t)$ and c_s is the isothermal speed of sound.

Numerical analysis and algorithm for the equations is provided in Appendix [102].

2.6 Dissipative Particle Dynamics

DPD is a multiparticle model that was initially introduced as a coarse-graining of molecular dynamics. In this thesis, I restrict my attention to statistical properties of a DPD solvent. DPD was introduced in [17, 18]. A pairwise force acts on each particle $\boldsymbol{F}_{ij}$ [19] and shifts their locations:

$$\frac{d\boldsymbol{r}_i}{dt} = \boldsymbol{v}_i, \quad \frac{d\boldsymbol{v}_i}{dt} = \frac{1}{m}\sum_{j\neq i}\boldsymbol{F}_{ij}\ . \tag{2.53}$$

The force $\boldsymbol{F}_{ij}$ consists of three different parts: conservative force $\boldsymbol{F}_{ij}^C$, dissipative force $\boldsymbol{F}_{ij}^D$ and random force $\boldsymbol{F}_{ij}^R$:

$$\boldsymbol{F}_{ij} = \boldsymbol{F}_{ij}^C + \boldsymbol{F}_{ij}^D + \boldsymbol{F}_{ij}^R\ . \tag{2.54}$$

The pairwise forces have a cutoff radius r_c which is taken as unity as well. The conservative force is repulsive between particles and acts along the connecting line between two particles

$$F_{ij}^C = \begin{cases} a_{ij} m(1 - \frac{r_{ij}}{r_c})\hat{\boldsymbol{r}}_{ij}, \ r_{ij} < r_c \\ 0, \ r_{ij} \geq r_c \end{cases} , \tag{2.55}$$

where a_{ij} is the maximum repulsion between the particles, $\boldsymbol{r}_{ij} = \boldsymbol{r}_i - \boldsymbol{r}_j$, $r_{ij} = |\boldsymbol{r}_{ij}|$ and $\hat{\boldsymbol{r}}_{ij} = \boldsymbol{r}_{ij}/r_{ij}$ are relative position, distance and unit vector between two particles i and j, respectively. The dissipative and random forces are

$$\boldsymbol{F}_{ij}^D = -m\gamma w^D(r_{ij})(\hat{\boldsymbol{r}}_{ij} \cdot \boldsymbol{v}_{ij})\hat{\boldsymbol{r}}_{ij} , \tag{2.56}$$

and

$$\boldsymbol{F}_{ij}^R = m\sigma w^R(r_{ij})\theta_{ij}\hat{\boldsymbol{r}}_{ij} , \tag{2.57}$$

where weighting functions $w^D(r_{ij})$ and $w^R(r_{ij})$ as well as dissipation coefficient γ and random coefficient σ are related so that they satisfy the fluctuation-dissipation balance [18]

$$w^D(r_{ij}) = (w^R(r_{ij}))^2, \ \ \gamma = \frac{\sigma^2}{2k_B T} . \tag{2.58}$$

Here, $\boldsymbol{r}_{ij} = \boldsymbol{r}_i - \boldsymbol{r}_j$, $r_{ij} = |\boldsymbol{r}_{ij}|$ and $\hat{\boldsymbol{r}}_{ij} = \boldsymbol{r}_{ij}/r_{ij}$ are relative position, distance and unit vector between two particles i and j, respectively. k_B is the Boltzmann constant and T is the temperature. $\boldsymbol{v}_{ij} = \boldsymbol{v}_i - \boldsymbol{v}_j$ is the relative velocity, and θ_{ij} is a Gaussian random variable with the properties [19]

$$\langle \theta_{ij}(t) \rangle = 0 , \tag{2.59}$$

$$\langle \theta_{ij}(t)\theta_{kl}(t') \rangle = (\delta_{ik}\delta_{jl} + \delta_{il}\delta_{jk})\delta(t - t') . \tag{2.60}$$

The standard weighting functions $w^R(r_{ij})$ and $w^D(r_{ij})$ are [19]

$$w^D(r_{ij}) = (w^R(r_{ij}))^2 = \begin{cases} \left(1 - \frac{r_{ij}}{r_c}\right)^2, \ r_{ij} < r_c \\ 0, \ r_{ij} \geq r_c \end{cases} . \tag{2.61}$$

Statistical properties

Stationary Probability density function of DPD solvent is Gaussian. DPD has the properties of the LLNS equations on large scales. On small scales, DPD is expected to represent features of the microscopic motion of fluids. In this sense, DPD might benefit over SDPD, as it has a potential to represent a wider range of scales. The main disadvantage of the DPD model, in comparison with SDPD, is that one has to use the mesoscopic DPD parameters. The relation between macroscopic parameters and the DPD parameters were derived

in [72, 71], however, is accurate in the limited number of cases. The problem is described with more aspects in the second paper in Appendix A [106] as well as a new approach to measure macroscopic parameters that is based on CACF consideration is suggested.

Analysis for large scales and mesoscales of DPD was performed analytically in [70]. It was also demonstrated, that on the large scales, the DPD resembles statistical properties of the LLNS equations. Statistical properties of DPD on small scales differ from the LLNS equations and are considered in the third paper in Appendix A [136].

Numerical algorithms

Time integration of DPD can be performed with Velocity-Verlet algorithms described in Section 2.1.1 for the case of low Schmidt numbers. For realistic Schmidt numbers of liquids, an implicit splitting scheme for DPD originally proposed by Shardlow can be used [137]. The superiority of the Shardlow-like splitting algorithm is shown in [138]. In [139], splitting algorithms were developed for constant-enthalpy and constant-energy DPD conditions. The papers related to DPD that are listed in Appendix A use Velocity-Verlet algorithm for time integration.

3 Accomplishments

3.1 Numerical methods for the weakly compressible Generalized Langevin Model in Eulerian reference frame

Turbulent flows are characterized by wide range of time and length scales. A common computational approach is to solve a filtered or averaged set of equations and to model small scales fluctuations with probability density function methods. The PDF can be evolved by Generalized Langevin Model introduced by Pope [8]. The natural representation of the model is a system of equations in Lagrangian frame, typically solved by particle methods. A representation in a Eulerian frame, however, has the potential to significantly reduce computational effort. The GLMEF has a potential of serving as approximate subgrid-scale reconstruction [132], where previously developed in [140, 141] approximate-deconvolution procedure for turbulent flows was used. There is a correspondence between GLMEF and nonlinear fluctuating hydrodynamics (NFHD) equations derived by Nakamura and Yoshimori [142]. Unlike Landau-Lifshitz Navier-Stokes equations NFHD equations are derived from the underdamped Langevin equation and do not require an assumption of local equilibrium. The objective of this work is to examine numerical methods that were recently

proposed for solving the LLNS equations when they are applied to GLMEF and to come to conclusions about their feasibility.

In **D. Azarnykh, S. Litvinov, N. A. Adams**: Numerical methods for the weakly compressible Generalized Langevin Model in Eulerian reference frame; Journal of Computational Physics; Volume 314, Pages 93-106, 2016 [102]

for spatial discretization, we use a skew-symmetric semi-discrete compact finite difference scheme on a regular grid [120] and for time integration we use a strongly-stable Runge-Kutta method [107]. Skew symmetry of the fluxes ensures that spatial scheme maintains a discrete fluctuation-dissipation balance. Two test cases in one dimension are considered following [31]. For the simulation of dilute monatomic gas where thermal fluctuations are in equilibrium, the spatial skew-symmetric scheme improves the prediction of static structure factor in comparison with other high-order finite volume schemes. The variance of the momentum, density and spectral autocorrelation of density function agrees with theory. For a random walk of a static shock wave, the model recovers the dependence of the shock-location variance on the Mach number

My contribution to this work lies in developing the method and its implementation in an in-house code. Moreover, I have verified the implementation and validated the method as well as performed the numerical simulations. The algorithm for postprocessing and analyzing the results is due to me. The manuscript for the publication has been written predominantly by me.

3.2 Determination of macroscopic transport coefficients of a dissipative particle dynamics solvent

Macroscopic parameters of a DPD solvent can be estimated with different methods. The standard methods are to use Poiseuille flow [143] or reverse Poiseuille flow [144, 145, 146] to estimate shear viscosity. However, the standard methods are unable to measure complicated relation of shear viscosity and length scales within one simulation. Moreover, these methods can not determine other macroscopic parameters, such as bulk viscosity and isothermal speed of sound.

The work **D. Azarnykh, S. Litvinov, X. Bian, N. A. Adams**: Determination of macroscopic transport coefficients of a dissipative particle dynamics solvent; Physical Review E - Statistical, Nonlinear, and Soft Matter Physics; Volume 93, (Issue 1), 2016 [106]

is devoted to the measurement of macroscopic parameters: shear viscosity, isothermal speed of sound and bulk viscosity in simulations of DPD solvent. For this purpose, we analyze CACF of DPD. One can think about CACF as a more general version of a radial distribution function. In fact, the former can be derived directly from CACF [98]. However, CACF contains more information, as it reflects also dynamic properties of the model. Moreover, analysis of CACF allows to see the properties of the DPD on different scales as well as to determine which is the maximum scale where DPD still reflects the real behavior of fluid and where numerical errors start to dominate. We introduce a new function that gives a good approximation for the modes of CACF in the DPD solvent and allows to measure shear viscosity with reasonably high accuracy from CACF for a wide range of parameters. We observe that macroscopic parameters of the DPD solvent depend on length scale. Bulk viscosity and shear viscosity measured in simulations are compared with analytical predictions, which were derived by Marsh [71, 72, 70] for the DPD solvent without repulsive potential.

My contribution to this work lies in developing the method. Moreover, I have verified the implementation and validated the method as well as performed the numerical simulations. The algorithm for postprocessing and analyzing the results is due to me. The manuscript for the publication has been written predominantly by me.

3.3 Discussions on the correspondence of dissipative particle dynamics and Langevin dynamics at small scales

In this work, the analysis of DPD with CACF is continued. We used the method developed in the previous article [106] to investigate small-scales dynamic of DPD. Macroscopic properties of DPD, such as shear and bulk viscosity as well as isothermal speed of sound depend on two non-dimensional length-scale parameters: cut-off radius r_c, and decorrelation length l_0. In the previous studies [72],[71],[70] different regimes of DPD were introduced, based on the correspondence between these two parameters, see Table 3.1.

Table 3.1: Regimes of DPD and corresponding hydrodynamic subregimes

Collective regime $r_c > l_0$	Particle regime $l_0 > r_c$
$\lambda > r_c > l_0$ Navier-Stokes	$\lambda > l_0 > r_c$ Navier-Stokes
$r_c > \lambda > l_0$ kinetic	$l_0 > \lambda > r_c$ mesoscopic
$r_c > l_0 > \lambda$ N-particle	$l_0 > r_c > \lambda$ N-particle

For these regimes, different approximations for DPD shear viscosity were derived. However, these laws were derived analytically and based on some assumptions.

In **D. Azarnykh, S. Litvinov, X. Bian, N. A. Adams** : Discussions on the correspondence of dissipative particle dynamics and langevin dynamics at small scales. Applied Mathematics and Mechanics; 39(1):31–46, 2018 [136].

we use numerical analysis to investigate the behavior of DPD on small scales in the 3D case. For that purpose, we measure current CACF of DPD in 3D. We compare CACF of DPD with the systems in which CACF can be derived analytically. We show similarities and differences of DPD with other systems and make conclusions about the correspondences of certain scales of DPD and Langevin equations. We extend and improve the findings of previous studies [72],[71],[70] and suggest that DPD has potential to model rarefied gas dynamics.

My contribution to this work lies in developing the method. Moreover, I have verified the implementation and validated the method as well as performed the numerical simulations. The algorithm for postprocessing and analyzing the results is due to me. The manuscript for the publication has been written predominantly by me.

4 List of Publications

- D. Azarnykh, S. Litvinov, N.A. Adams. Numerical methods for the weakly compressible Generalized Langevin Model in Eulerian reference frame. Journal of Computational Physics; Volume 314, Pages 93-106, 2016
- D. Azarnykh, S. Litvinov, X. Bian, N. A. Adams. Determination of macroscopic transport coefficients of a dissipative particle dynamics solvent. Physical Review E - Statistical, Nonlinear, and Soft Matter Physics; Volume 93, (Issue 1), 2016
- D. Azarnykh, S. Litvinov, X. Bian, N. A. Adams. Discussions on the correspondence of dissipative particle dynamics and langevin dynamics at small scales. Applied Mathematics and Mechanics; 39(1):31–46, 2018

A Appendix

In the appendix, the three major publications are attached together with the publisher agreement notification to reuse the material for this cumulative thesis.

A.1 Numerical methods for the weakly compressible Generalized Langevin Model in Eulerian reference frame

Attn: Dmitrii Alexandrovich Azarnykh

Total 0.00 EUR

Terms and Conditions

INTRODUCTION

1. The publisher for this copyrighted material is Elsevier. By clicking "accept" in connection with completing this licensing transaction, you agree that the following terms and conditions apply to this transaction (along with the Billing and Payment terms and conditions established by Copyright Clearance Center, Inc. ("CCC"), at the time that you opened your Rightslink account and that are available at any time at http://myaccount.copyright.com).

GENERAL TERMS

2. Elsevier hereby grants you permission to reproduce the aforementioned material subject to the terms and conditions indicated.
3. Acknowledgement: If any part of the material to be used (for example, figures) has appeared in our publication with credit or acknowledgement to another source, permission must also be sought from that source. If such permission is not obtained then that material may not be included in your publication/copies. Suitable acknowledgement to the source must be made, either as a footnote or in a reference list at the end of your publication, as follows:
"Reprinted from Publication title, Vol /edition number, Author(s), Title of article / title of chapter, Pages No., Copyright (Year), with permission from Elsevier [OR APPLICABLE SOCIETY COPYRIGHT OWNER]." Also Lancet special credit - "Reprinted from The Lancet, Vol. number, Author(s), Title of article, Pages No., Copyright (Year), with permission from Elsevier."
4. Reproduction of this material is confined to the purpose and/or media for which permission is hereby given.
5. Altering/Modifying Material: Not Permitted. However figures and illustrations may be altered/adapted minimally to serve your work. Any other abbreviations, additions, deletions and/or any other alterations shall be made only with prior written authorization of Elsevier Ltd. (Please contact Elsevier at permissions@elsevier.com)
6. If the permission fee for the requested use of our material is waived in this instance, please be advised that your future requests for Elsevier materials may attract a fee.
7. Reservation of Rights: Publisher reserves all rights not specifically granted in the combination of (i) the license details provided by you and accepted in the course of this licensing transaction, (ii) these terms and conditions and (iii) CCC's Billing and Payment terms and conditions.
8. License Contingent Upon Payment: While you may exercise the rights licensed immediately upon issuance of the license at the end of the licensing process for the transaction, provided that you have disclosed complete and accurate details of your proposed use, no license is finally effective unless and until full payment is received from you (either by

publisher or by CCC) as provided in CCC's Billing and Payment terms and conditions. If full payment is not received on a timely basis, then any license preliminarily granted shall be deemed automatically revoked and shall be void as if never granted. Further, in the event that you breach any of these terms and conditions or any of CCC's Billing and Payment terms and conditions, the license is automatically revoked and shall be void as if never granted. Use of materials as described in a revoked license, as well as any use of the materials beyond the scope of an unrevoked license, may constitute copyright infringement and publisher reserves the right to take any and all action to protect its copyright in the materials.
9. Warranties: Publisher makes no representations or warranties with respect to the licensed material.
10. Indemnity: You hereby indemnify and agree to hold harmless publisher and CCC, and their respective officers, directors, employees and agents, from and against any and all claims arising out of your use of the licensed material other than as specifically authorized pursuant to this license.
11. No Transfer of License: This license is personal to you and may not be sublicensed, assigned, or transferred by you to any other person without publisher's written permission.
12. No Amendment Except in Writing: This license may not be amended except in a writing signed by both parties (or, in the case of publisher, by CCC on publisher's behalf).
13. Objection to Contrary Terms: Publisher hereby objects to any terms contained in any purchase order, acknowledgment, check endorsement or other writing prepared by you, which terms are inconsistent with these terms and conditions or CCC's Billing and Payment terms and conditions. These terms and conditions, together with CCC's Billing and Payment terms and conditions (which are incorporated herein), comprise the entire agreement between you and publisher (and CCC) concerning this licensing transaction. In the event of any conflict between your obligations established by these terms and conditions and those established by CCC's Billing and Payment terms and conditions, these terms and conditions shall control.
14. Revocation: Elsevier or Copyright Clearance Center may deny the permissions described in this License at their sole discretion, for any reason or no reason, with a full refund payable to you. Notice of such denial will be made using the contact information provided by you. Failure to receive such notice will not alter or invalidate the denial. In no event will Elsevier or Copyright Clearance Center be responsible or liable for any costs, expenses or damage incurred by you as a result of a denial of your permission request, other than a refund of the amount(s) paid by you to Elsevier and/or Copyright Clearance Center for denied permissions.

LIMITED LICENSE

The following terms and conditions apply only to specific license types:
15. **Translation**: This permission is granted for non-exclusive world **English** rights only unless your license was granted for translation rights. If you licensed translation rights you may only translate this content into the languages you requested. A professional translator must perform all translations and reproduce the content word for word preserving the integrity of the article.
16. **Posting licensed content on any Website**: The following terms and conditions apply as follows: Licensing material from an Elsevier journal: All content posted to the web site must maintain the copyright information line on the bottom of each image; A hyper-text must be included to the Homepage of the journal from which you are licensing at http://www.sciencedirect.com/science/journal/xxxxx or the Elsevier homepage for books at http://www.elsevier.com; Central Storage: This license does not include permission for a scanned version of the material to be stored in a central repository such as that provided by Heron/XanEdu.
Licensing material from an Elsevier book: A hyper-text link must be included to the Elsevier homepage at http://www.elsevier.com . All content posted to the web site must maintain the copyright information line on the bottom of each image.

Posting licensed content on Electronic reserve: In addition to the above the following clauses are applicable: The web site must be password-protected and made available only to bona fide students registered on a relevant course. This permission is granted for 1 year only. You may obtain a new license for future website posting.
17. **For journal authors:** the following clauses are applicable in addition to the above:
Preprints:
A preprint is an author's own write-up of research results and analysis, it has not been peer-reviewed, nor has it had any other value added to it by a publisher (such as formatting, copyright, technical enhancement etc.).
Authors can share their preprints anywhere at any time. Preprints should not be added to or enhanced in any way in order to appear more like, or to substitute for, the final versions of articles however authors can update their preprints on arXiv or RePEc with their Accepted Author Manuscript (see below).
If accepted for publication, we encourage authors to link from the preprint to their formal publication via its DOI. Millions of researchers have access to the formal publications on ScienceDirect, and so links will help users to find, access, cite and use the best available version. Please note that Cell Press, The Lancet and some society-owned have different preprint policies. Information on these policies is available on the journal homepage.

Accepted Author Manuscripts: An accepted author manuscript is the manuscript of an article that has been accepted for publication and which typically includes author-incorporated changes suggested during submission, peer review and editor-author communications.
Authors can share their accepted author manuscript:

- immediately
  - via their non-commercial person homepage or blog
  - by updating a preprint in arXiv or RePEc with the accepted manuscript
  - via their research institute or institutional repository for internal institutional uses or as part of an invitation-only research collaboration work-group
  - directly by providing copies to their students or to research collaborators for their personal use
  - for private scholarly sharing as part of an invitation-only work group on commercial sites with which Elsevier has an agreement
- after the embargo period
  - via non-commercial hosting platforms such as their institutional repository
  - via commercial sites with which Elsevier has an agreement

In all cases accepted manuscripts should:

- link to the formal publication via its DOI
- bear a CC-BY-NC-ND license - this is easy to do
- if aggregated with other manuscripts, for example in a repository or other site, be shared in alignment with our hosting policy not be added to or enhanced in any way to appear more like, or to substitute for, the published journal article.

Published journal article (JPA): A published journal article (PJA) is the definitive final record of published research that appears or will appear in the journal and embodies all value-adding publishing activities including peer review co-ordination, copy-editing, formatting, (if relevant) pagination and online enrichment.
Policies for sharing publishing journal articles differ for subscription and gold open access articles:
Subscription Articles: If you are an author, please share a link to your article rather than the full-text. Millions of researchers have access to the formal publications on ScienceDirect, and so links will help your users to find, access, cite, and use the best available version.
Theses and dissertations which contain embedded PJAs as part of the formal submission can be posted publicly by the awarding institution with DOI links back to the formal publications on ScienceDirect.
If you are affiliated with a library that subscribes to ScienceDirect you

is the responsibility of the user to ensure their reuse complies with the terms and conditions determined by the rights holder.
Additional Terms & Conditions applicable to each Creative Commons user license:
CC BY: The CC-BY license allows users to copy, to create extracts, abstracts and new works from the Article, to alter and revise the Article and to make commercial use of the Article (including reuse and/or resale of the Article by commercial entities), provided the user gives appropriate credit (with a link to the formal publication through the relevant DOI), provides a link to the license, indicates if changes were made and the licensor is not represented as endorsing the use made of the work. The full details of the license are available at http://creativecommons.org/licenses/by/4.0.
CC BY NC SA: The CC BY-NC-SA license allows users to copy, to create extracts, abstracts and new works from the Article, to alter and revise the Article, provided this is not done for commercial purposes, and that the user gives appropriate credit (with a link to the formal publication through the relevant DOI), provides a link to the license, indicates if changes were made and the licensor is not represented as endorsing the use made of the work. Further, any new works must be made available on the same conditions. The full details of the license are available at http://creativecommons.org/licenses/by-nc-sa/4.0.
CC BY NC ND: The CC BY-NC-ND license allows users to copy and distribute the Article, provided this is not done for commercial purposes and further does not permit distribution of the Article if it is changed or edited in any way, and provided the user gives appropriate credit (with a link to the formal publication through the relevant DOI), provides a link to the license, and that the licensor is not represented as endorsing the use made of the work. The full details of the license are available at http://creativecommons.org/licenses/by-nc-nd/4.0. Any commercial reuse of Open Access articles published with a CC BY NC SA or CC BY NC ND license requires permission from Elsevier and will be subject to a fee. Commercial reuse includes:

- Associating advertising with the full text of the Article
- Charging fees for document delivery or access
- Article aggregation
- Systematic distribution via e-mail lists or share buttons

Posting or linking by commercial companies for use by customers of those companies.

20. **Other Conditions**:

v1.8

Journal of Computational Physics 314 (2016) 93–106

Contents lists available at ScienceDirect

Journal of Computational Physics

www.elsevier.com/locate/jcp

Numerical methods for the weakly compressible Generalized Langevin Model in Eulerian reference frame

Dmitrii Azarnykh *, Sergey Litvinov, Nikolaus A. Adams

Institute of Aerodynamics and Fluid Mechanics, Technical University of Munich, Garching, Germany

ARTICLE INFO

Article history:
Received 29 May 2015
Received in revised form 10 December 2015
Accepted 29 February 2016
Available online 8 March 2016

Keywords:
Generalized Langevin Model
Fluctuating hydrodynamics
Eulerian reference frame
Nonlinear stochastic partial differential equations
Turbulent flow

ABSTRACT

A well established approach for the computation of turbulent flow without resolving all turbulent flow scales is to solve a filtered or averaged set of equations, and to model non-resolved scales by closures derived from transported probability density functions (PDF) for velocity fluctuations. Effective numerical methods for PDF transport employ the equivalence between the Fokker–Planck equation for the PDF and a Generalized Langevin Model (GLM), and compute the PDF by transporting a set of sampling particles by GLM (Pope (1985) [1]). The natural representation of GLM is a system of stochastic differential equations in a Lagrangian reference frame, typically solved by particle methods. A representation in a Eulerian reference frame, however, has the potential to significantly reduce computational effort and to allow for the seamless integration into a Eulerian-frame numerical flow solver. GLM in a Eulerian frame (GLMEF) formally corresponds to the nonlinear fluctuating hydrodynamic equations derived by Nakamura and Yoshimori (2009) [12]. Unlike the more common Landau–Lifshitz Navier–Stokes (LLNS) equations these equations are derived from the underdamped Langevin equation and are not based on a local equilibrium assumption. Similarly to LLNS equations the numerical solution of GLMEF requires special considerations. In this paper we investigate different numerical approaches to solving GLMEF with respect to the correct representation of stochastic properties of the solution. We find that a discretely conservative staggered finite-difference scheme, adapted from a scheme originally proposed for turbulent incompressible flow, in conjunction with a strongly stable (for non-stochastic PDE) Runge–Kutta method performs better for GLMEF than schemes adopted from those proposed previously for the LLNS. We show that equilibrium stochastic fluctuations are correctly reproduced.

1. Introduction

The Generalized Langevin Model (GLM), introduced by Pope [1], is a rather well established Lagrangian approximation of the Fokker–Planck equation for the probability density function (PDF) of turbulent fluctuations [2]. A drawback of GLM is that its Lagrangian formulation leads to a particle discretization scheme, which cannot be seamlessly integrated into a Eulerian frame grid-based solution algorithm for the mean or filtered flow field.

A Eulerian reference frame PDF-based approach has been applied for modeling turbulent reactive flows [3]. O. Soulard and V. Sabelnikov proposed the Eulerian Monte Carlo (EMC) method to solve a transport equation for the Favre joint PDF of velocity fields and turbulent reactive scalars [4–6]. A challenge for the application of EMC to turbulent flows originates

* Corresponding author.
E-mail address: d.azarnykh@tum.de (D. Azarnykh).

http://dx.doi.org/10.1016/j.jcp.2016.02.073
0021-9991/

from the particular properties of the resulting stochastic partial differential equations (SPDEs). Further research on the topic demonstrated that the equivalence of the solutions obtained from the PDF transport equations and that from the EMC SPDEs is based on multi-valued solution of the SPDEs [7,8]. In this work also an algorithm to solve EMC SPDEs was proposed. The solution of EMC SPDEs is statistically equivalent to that of a Fokker–Planck equation without potential force. The same kind of Fokker–Planck equation is obtained for GLM which shows that EMC is well suited for modeling turbulent fluctuations.

In [9] a stochastic extension of the approximate deconvolution subgrid-scale model (ADM) [10,11] has been proposed to cope with the hard-deconvolution problem in turbulence modeling by an enrichment of subgrid-scales from a stochastic model for turbulent transport. A Eulerian-reference-frame formulation of GLM was proposed (GLMEF) which differs from GLM by a repulsive potential. Results for isotropic compressible turbulence have indicated an improvement on the standard formulation of ADM. However, neither has this paper addressed the question of consistent numerical discretizations of GLMEF, nor have the particular properties of GLMEF been analyzed. Besides the repulsive potential, another difference between GLMEF and EMC is that with EMC the stochastic force is delta-correlated in time and not in space.

GLMEF is a particular case of the Nonlinear Fluctuating Hydrodynamic (NFHD) equations that have been derived by Nakamura and Yoshimori [12] from the underdamped Langevin equation in the Lagrangian reference frame. NFHD and thus GLMEF are based on earlier work by Dean [13] and share similarities with the Landau–Lifshitz Navier–Stokes (LLNS) equations [12,14–17]. GLMEF and LLNS differ by their dissipative mechanism and by the fact that with LLNS the stochastic force is expressed in divergence form. Due to these differences GLMEF and LLNS have different ways of satisfying a fluctuation–dissipation balance and thus may complement each other as models for nonequilibrium fluctuations in fluids. This is the reason that in the current paper we investigate the numerical discretization of GLMEF in order to enable future numerical experimentation similarly as has been done in previous work on LLNS.

2. GLMEF model equations

In order to facilitate analytical understanding and numerical accessibility we will in this paper restrict ourselves to spatially one-dimensional (1D) configurations. The underlying NFHD equations can be written in the following form

$$\frac{\partial n(x,t)}{\partial t} + \frac{1}{m}\frac{\partial g(x,t)}{\partial x} = 0 \tag{1a}$$

$$\frac{\partial g(x,t)}{\partial t} + \frac{\partial}{\partial x}\frac{g^2(x,t)}{m\, n(x,t)} = -n(x,t)\frac{\partial}{\partial x}\left(\frac{\delta H_V[n(x,t)]}{\delta n(x,t)}\right) - \gamma_n g(x,t) + \sqrt{D n(x,t)\gamma_n}\,\zeta(x,t)\,, \tag{1b}$$

where m is the constant mass of the notional sample particles, D and γ_n correspond to fluctuation and dissipation coefficients (considered as constant in the following). $n(x,t)$, $g(x,t) := mn(x,t)u(x,t)$ denote number density and momentum fields respectively and are defined at the position x_j and for the momentum p_j of the notional particles $j = 1,\ldots,N_p$ in the Lagrangian reference frame as

$$n(x,t) = \sum_{j=1}^{N_p}\delta(x - x_j(t)); \quad g(x,t) = \sum_{j=1}^{N_p} p_j(t)\delta(x - x_j(t))\,.$$

$H_V[n(x,t)]$ is a functional for the internal energy of the system. $\zeta(x,t)$ is a Gaussian white noise uncorrelated in time and space

$$\overline{\zeta(x,t)\zeta(x',t')} = 2\delta(x - x')(t - t').$$

The Generalized Langevin Model in Eulerian frame (GLMEF) follows from equations (1) by setting

$$\rho(x,t) := n(x,t)m\,,$$

$$\gamma := \gamma_n/m\,, \tag{2}$$

$$n(x,t)\frac{\partial}{\partial x}\left(\frac{\delta H_V[n(x,t)]}{\delta n(x,t)}\right) := c_s^2\frac{\partial \rho(x,t)}{\partial x}\,. \tag{3}$$

The definition in (3) is motivated by weakly-compressible approaches in macroscopic and mesoscopic particle discretizations of transport equations (smoothed-particle hydrodynamics) [18]. As explained in [9], for consistency of the GLMEF derivation with the underlying Lagrangian form it is necessary to ensure that no two notional particles occupy the same location at the same time, which can be accomplished by a repulsive potential implied through relation (3). In Eulerian reference frame, the situation that two notional particles occupy the same location corresponds to crossing of characteristic curves which can occur even for smooth initial values [7,8]. The resulting GLMEF equations result from taking into consideration a mean velocity $u_0(x,t)$ which in the current work is assumed to be known

$$\frac{\partial \rho(x,t)}{\partial t} + \frac{\partial g(x,t)}{\partial x} = 0 \tag{4a}$$

$$\frac{\partial g(x,t)}{\partial t} + \frac{\partial}{\partial x}\frac{g^2(x,t)}{\rho(x,t)} = -\frac{\partial p(x,t)}{\partial x} - \gamma\rho(x,t)\,(u(x,t) - u_0(x,t)) + \sqrt{\rho(x,t)D\gamma}\,\zeta(x,t)\,, \tag{4b}$$

with the weakly compressible equation of state

$$p(x,t) = \rho(x,t)c_s^2 \,. \tag{4c}$$

In these equations $\rho(x,t)$ and $p(x,t)$ denote mass density and pressure fields, respectively, and c_s is the isothermal speed of sound.

In a first straightforward application of GLMEF [9] the same numerical discretization scheme (pseudo spectral in space and three-stage Runge–Kutta scheme in time) was applied as for the underlying macroscopic (filtered) flow-evolution equations (compressible Navier–Stokes equations). However, no analyses have been performed on the accuracy of this scheme with respect to reproducing statistical properties of GLMEF. Furthermore, pseudo-spectral schemes are difficult to apply to more complex configurations than the triply periodic domains considered in that paper. The objective of this paper is to revisit the issue of suitable and accurate discretization of GLMEF, following the analyses of numerical schemes for the LLNS due to their similarity with GLMEF.

GLMEF is a system of coupled nonlinear Stochastic Partial Differential Equations. In recent years significant progress on solving nonlinear SPDE in a Eulerian reference frame has been achieved. Bell et al. [15] compared different numerical methods for the compressible LLNS equations. Several equilibrium and nonequilibrium cases were considered. With respect to time integration, best results were obtained with a variance-preserving third-order Runge–Kutta (VP RK3) scheme employing third-order, total variation diminishing (TVD RK3) Stratonovich time integration. Spatial discretization was done by a fourth-order finite-volume scheme. Donev et al. [19] proposed a new approach to examine grid-based spatiotemporal schemes for nonlinear SPDEs in a Eulerian reference frame. The analysis relies on static and dynamic structure factors (SSF and DSF) in Fourier space. SSF and DSF were derived analytically from the linearization of the underlying SPDEs. Upon satisfying the fluctuation dissipation balance for LLNS, the equilibrium SSF should be unity, which Donev et al. have used to modify the original TVD Runge–Kutta time integration scheme. Balboa et al. [20] used a staggered-grid discretization for isothermal compressible and incompressible LLNS. Different types of temporal discretizations were examined for the fluctuating Burgers equation with staggered grid spatial discretization by Delong et al. [21].

An important difference between LLNS, which previous numerical method development has focused on, and GLMEF is that for LLNS the stochastic forcing term appears in divergence form. The GLMEF equations satisfy a fluctuation–dissipation relation of the second kind [12], with the stochastic forcing term being in non-conservative form. The GLMEF equations are derived from the underdamped Langevin equation and do not imply the assumption of local equilibrium. Moreover, the GLMEF equations can represent phenomena with non-Gaussian probability distribution function (PDF) of the density and velocity fields. Such properties differ from that of LLNS considered in [19–21], and motivate the derivation and analysis of suitable discretization schemes for their numerical solution. Due to their different properties, it cannot be expected that discretization schemes derived for the LLNS equations transfer their properties when applied to GLMEF. The purpose of our work is to analyze the performance of methods derived for LLNS and stochastic Burgers equations upon their application to GLMEF. We address deficits of these methods and propose an alternative scheme which delivers considerably improved results. As this is the first investigation, to our knowledge, of numerical discretizations for GLMEF, we follow the approach of previous work on LLNS of a stepwise increase in complexity, and will restrict the work in this paper to GLMEF in one spatial dimension.

3. Properties of GLMEF

Several criteria have been proposed for the analysis of discretization schemes for the LLNS equations. We follow these concepts and provide in this section the corresponding properties of GLMEF in terms of the static and dynamic structure factor. Furthermore, we extend previous analyses by considering also the non-Gaussian property of the PDF.

3.1. Static and dynamic structure factor

For the analysis of discretization schemes it is convenient to consider a spectral-space description rather than real space. For this purpose one derives analytical relations for dynamic and static structure factors for the corresponding linearized SPDEs. Here we follow the general procedures presented in [19,22] to derive dynamic and static structure factors for the linearized GLMEF. Linearization is performed around a uniform reference equilibrium state $\rho(x,t) = \rho_0 + \rho_1(x,t)$ and $u(x,t) = u_0 + u_1(x,t)$. Furthermore, we assume $\rho_1 \ll |u_1|$. Upon linearization, equations (4) can be written as

$$dU(t) = LU(t) + KdB(x,t) \,, \tag{5}$$

with definitions

$$L(\mathbf{x}) = \begin{pmatrix} 0 & \rho_0 \frac{\partial}{\partial \mathbf{x}} \\ c_s^2 \frac{\partial}{\partial \mathbf{x}} & -\gamma\rho_0 \end{pmatrix} \quad K(\mathbf{x}) = \begin{pmatrix} 0 & 0 \\ 0 & \sqrt{D\gamma\rho_0} \end{pmatrix} \quad U(\mathbf{x},t) = \begin{pmatrix} \rho(\mathbf{x},t) \\ u(\mathbf{x},t) \end{pmatrix}$$

and $dB(x,t)$ is a Gaussian-noise forcing.

For simplicity we consider stationary fluctuations and a domain with periodic boundaries, so that the linearized GLMEF can be Fourier transformed in space and time and becomes

$$i\omega\hat{U}(k,\omega) = \hat{L}(k)\hat{U}(k,\omega) + \hat{K}d\hat{B}(k,\omega)\ . \tag{6}$$

ω and k are the dual independent variables in Fourier space, i.e. frequency and wave number. The dynamic structure factor characterizes the statistical properties of eq. (5). It is given by the covariance matrix

$$\mathbf{S}(k,\omega) = \frac{1}{D}\langle\hat{U}(k,\omega)\hat{U}^{\star}(k,\omega)\rangle = (\hat{L}(k) - i\omega I)^{-1}(\hat{K}\hat{K}^{\star})(\hat{L}^{\star}(k) + i\omega I)^{-1}\ . \tag{7}$$

We denote the dynamic structure factor as $S_{\phi_1\phi_2}(k,\omega)$ and the static structure factor as $S_{\phi_1\phi_2}(k)$ for the respective scalar fields $\phi_1(k,\omega)$ and $\phi_2(k,\omega)$. Accordingly, for the GLMEF equation in one space dimension we obtain two scalar fields $\hat{\rho}(k,\omega)$ and $\hat{u}(k,\omega)$, and eq. (7) becomes

$$\mathbf{S}(k,\omega) = \begin{pmatrix} S_{uu}(k,\omega) & S_{u\rho}(k,\omega) \\ S_{\rho u}(k,\omega) & S_{\rho\rho}(k,\omega) \end{pmatrix} \tag{8}$$

with the components

$$S_{uu}(k,\omega) = \frac{\gamma\,\omega^2}{\left(c_s{}^2\,k^2 - \omega^2\right)^2 + \gamma^2\,\omega^2}\ , \tag{9a}$$

$$S_{\rho\rho}(k,\omega) = \frac{\gamma\,c_s{}^2\,k^2}{\left(c_s{}^2\,k^2 - \omega^2\right)^2 + \gamma^2\,\omega^2}\ , \tag{9b}$$

$$S_{\rho u}(k,\omega) = S_{u\rho}(k,\omega) = 0\ . \tag{9c}$$

For equilibrium fluctuations the static structure-factor components are obtained by averaging over ω as

$$S_{uu}(k) = \frac{1}{2\pi}\int_{-\infty}^{+\infty} S_{uu}(k,\omega)d\omega = 1\ , \tag{10a}$$

$$S_{\rho\rho}(k) = \frac{1}{2\pi}\int_{-\infty}^{+\infty} S_{\rho\rho}(k,\omega)d\omega = 1\ . \tag{10b}$$

The static structure factors of velocity and density fluctuations is unity, which is consistent with the fluctuation–dissipation theorem (FDT).

From the dynamic structure factor one can derive an equation for the spectral correlation of the density field in time upon inverse Fourier transform of (9b) for the case of stationary equilibrium fluctuations

$$\frac{\langle\hat{\rho}(k,t)\,\hat{\rho}(k,t+\tau)\rangle}{\langle\hat{\rho}^2(k,t)\rangle} = \frac{\gamma}{\sqrt{4\,c_s{}^2\,k^2 - \gamma^2}}e^{-\frac{\gamma\,\tau}{2}}\sin\left(\frac{\sqrt{4\,c_s{}^2\,k^2 - \gamma^2}\,\tau}{2}\right) + e^{-\frac{\gamma\,\tau}{2}}\cos\left(\frac{\sqrt{4\,c_s{}^2\,k^2 - \gamma^2}\,\tau}{2}\right)\ , \tag{11}$$

where $\langle\bullet\rangle$ denotes averaging over time. The term $-\gamma^2$ under the square root originates from the derivative of the dissipation term. When $0 \le \gamma \ll 1$ this contribution can be neglected in comparison to $4c_s^2k^2$, and we obtain

$$\left.\frac{\langle\hat{\rho}(k,t)\hat{\rho}(k,t+\tau)\rangle}{\langle\hat{\rho}^2(k,t)\rangle}\right|_{GLMEF} = e^{-\frac{\gamma}{2}\tau}\cos(c_sk\tau) + \frac{\gamma}{2kc_s}e^{-\frac{\gamma}{2}\tau}\sin(c_sk\tau)\ . \tag{12}$$

A similar analysis is performed for the velocity field. The spectral correlation of the velocity field in time is

$$\left.\frac{\langle\hat{u}(k,t)\hat{u}(k,t+\tau)\rangle}{\langle\hat{u}^2(k,t)\rangle}\right|_{GLMEF} = e^{-\frac{\gamma}{2}\tau}\cos(c_sk\tau) - \frac{\gamma}{2kc_s}e^{-\frac{\gamma}{2}\tau}\sin(c_sk\tau)\ . \tag{13}$$

Eq. (12) can be compared with the two-point time correlation of density obtained for LLNS. For this purpose, we use the expression derived for the compressible LLNS in [23,24] and set the ratio of specific heats to unity. This corresponds an isothermal form of the LLNS with a weakly compressible equation of state that we also use for GLMEF. We do not consider bulk viscosity, and $\nu = \frac{\eta}{\rho}$ denotes the kinematic viscosity. We follow [15] to obtain

$$\left.\frac{\langle\rho(k,t)\rho(k,t+\tau)\rangle}{\delta\rho^2(k,t)}\right|_{LLNS} = e^{-k^2\frac{2\nu}{3}\tau}\cos(c_sk\tau) + \frac{k\nu}{2c_s}e^{-k^2\frac{2\nu}{3}\tau}\sin(c_sk\tau)\ . \tag{14}$$

Upon comparison of (12) and (14) it is apparent that the equations are identical for the wave number $k = k_0$ which satisfies

$$\gamma = \frac{4}{3}\nu k_0^2 = \frac{4}{3}\frac{\eta}{\bar{\rho}}\left(\frac{2\pi n_0}{L}\right)^2 , \tag{15}$$

where n_0 is the corresponding integer wave number. In the following we set $n_0 = 1$ and adjust the parameters ν and γ accordingly.

3.2. Probability density functions

The Fokker–Planck equation for GLMEF has been derived in [12] as

$$\frac{\partial P([\rho, g], t)}{\partial x} = \hat{L}([\rho, g])P([\rho, g], t) ,$$

with the linear operator

$$\hat{L}([\rho, g]) = \int dx \left(\frac{\delta}{\delta \rho(x)} \nabla \cdot g(x) + \frac{\delta}{\delta g(x)} \cdot \left(\rho(x) \nabla \left(\frac{\delta H_V[\rho]}{\delta \rho(x)} \right) + \nabla \cdot \left(\frac{g^2(x)}{\rho(x)} \right) \right) + \frac{\delta}{\delta g(x)} \cdot \gamma \rho(x) \left(D \frac{\delta}{\delta g(x)} + \frac{\delta H_K[\rho, g]}{\delta g(x)} \right) \right) .$$

In this equation H_V and H_K are functionals for the internal and the kinetic energy, respectively. As stated in [12], the corresponding steady-state probability-density function (PDF) is given by

$$P_{eq}[\rho, g] = \frac{1}{Z} \exp\left(-\frac{H_V[\rho] + H_K[\rho, g]}{D} \right) , \tag{16}$$

where Z is a normalization coefficient. For the 1D GLMEF (4) we obtain the steady-state PDF for a H_V that is consistent with the underlying weakly compressible model

$$n(x, t) \frac{\partial}{\partial x} \frac{\delta H_V[n]}{\delta n(x, t)} = m c_s^2 \frac{\partial n(x, t)}{\partial x} . \tag{17}$$

The solution of this equation is

$$H_V[n] = m c_s^2 n(x, t) \left(\log(n(x, t)) - 1 + C_1 \right) + C_2 , \tag{18}$$

with integration constants C_1 and C_2. C_2 can be merged with the normalization coefficient Z in Eq. (16). For determining C_1 we stipulate that for $n(x, t) = \bar{n}$, where $\bar{n}$ is the spatial average number density, the internal energy becomes $H_V[\bar{n}] = -m c_s^2 \bar{n}$, resulting in

$$C_1 = -\log(\bar{n}) ,$$

and

$$H_V[n] = m c_s^2 n(x, t) \left(\log\left(\frac{n(x, t)}{\bar{n}} \right) - 1 \right) ,$$

or alternatively written as mass density

$$H_V[\rho] = c^2 \rho(x, t) \log\left(\frac{\rho(x, t)}{\bar{\rho}} \right) - c^2 \rho(x, t).$$

As the kinetic energy functional is given by

$$H_K[\rho, g] = \frac{g^2(x, t)}{2\rho(x, t)} ,$$

the steady-state PDF becomes

$$P_{eq}[\rho, g] = \frac{1}{Z} \exp\left(-\frac{c^2 \rho(x, t) \log\left(\frac{\rho(x,t)}{\bar{\rho}} \right) - c^2 \rho(x, t) + \frac{g^2(x,t)}{2\rho(x,t)}}{D} \right) . \tag{19}$$

The marginal steady-state PDF for momentum and mass density are obtained from

$$P_{eq}[\rho] = \int du(x, t) P_{eq}[\rho, g] \tag{20}$$

and

$$P_{eq}[g] = \int d\rho(x,t) P_{eq}[\rho, g] \,. \tag{21}$$

For analytic derivations we have relied on the Maxima computer algebra system [25].

4. Spatial discretization schemes

For the discretization of the convective term of the GLMEF different classes of spatial schemes can be considered. One option is a staggered scheme that has improved stability and accuracy properties for small-scale fluctuations of LLNS (characterized by a stochastic force in divergence form) as compared to collocated schemes [20,26]. A drawback of staggered schemes is that they require interpolation operations to transform between cell-center and cell-vertex variables. Motivated by previous research we will assess in the following three different spatial discretizations schemes for GLMEF: (i) the fourth-order finite-volume scheme proposed by Bell et al. [15], (ii) a second-order energy-conservative skew-symmetric scheme based on a staggered grid, and (iii) a second-order energy-conservative skew-symmetric scheme based on a collocated grid [27].

4.1. Fourth-order finite-volume scheme in a collocated grid

A fourth-order finite-volume spatial discretization scheme was studied by Bell et al. [15]. The scheme is similar to the piece-wise parabolic discretization method, however does not employ a characteristic-projection reconstruction procedure. Conservative variables at cell-faces are reconstructed by

$$g_{i+1/2} = \alpha_1(g_j + g_{j+1}) - \alpha_2(g_{j-1} + g_{j+2})$$

and

$$\rho_{i+1/2} = \alpha_1(\rho_j + \rho_{j+1}) - \alpha_2(\rho_{j-1} + \rho_{j+2}) \,,$$

with coefficients

$$\alpha_1 = \frac{7}{12};\ \alpha_2 = \frac{1}{12} \,.$$

4.2. Compact finite-difference schemes for staggered grid

The advantage of staggered grids is due to their stability in the incompressible limit, as they preclude the so-called odd-even decoupling during pressure-projection. Moreover, staggered compact schemes have better wave-resolution properties than collocated schemes of like order [28], and it was demonstrated that skew-symmetric staggered schemes maintain a discrete fluctuation–dissipation balance [20]. The staggered-grid scheme of Voulgarakis and Chu [26] shows improved predictions of the spatial density-field correlation for nonlinear SPDEs with a noise term in divergence form (as for LLNS).

These results indicate that advantages of staggered schemes for deterministic transport equations may transfer to stochastic equations. For this reason we consider a family of skew-symmetric schemes proposed by Morinishi [27]. The convective term for a transported scalar ϕ is re-written in skew-symmetric form as

$$(Skew.)_\phi = \sqrt{\rho}\frac{\partial\sqrt{\rho}\phi}{\partial t} + \frac{1}{2}\left(\frac{\partial \rho u_j \phi}{\partial x_j} + \rho u_j \frac{\partial \phi}{\partial x_j}\right) \,.$$

A second-order, skew-symmetric, staggered, energy conservative scheme results as

$$\begin{aligned}(Skew.-SC_2) = &\sqrt{\frac{1}{2}(\rho_{i+1}+\rho_i)}\frac{\partial\sqrt{\frac{1}{2}(\rho_{i+1}+\rho_i)}u_{i+1/2}}{\partial t} + \\ &+ \frac{1}{8dx}\Big((\rho_{i+2}+\rho_{i+1})u_{i+3/2}^2 - (\rho_{i-1}+\rho_i)u_{i-1/2}^2 + \\ &+ (\rho_{i+1}+\rho_i)u_{i+1/2}u_{i+3/2} - (\rho_{i+1}+\rho_i)u_{i+1/2}u_{i-1/2}\Big) \,.\end{aligned}$$

4.3. Semi-discrete compact finite difference scheme in a regular grid

Staggered grids increase implementational complexity and require the definition of consistent interpolation operators between variables at cell centers and at cell vertices. We also consider a second-order, conservative, skew-symmetric scheme on a collocated grid, as proposed by Morinishi in order to analyze whether the staggered formulation exhibits advantages over the collocated also for GLMEF,

$$(Skew.-RC_2) = \sqrt{\rho_i}\frac{\partial\sqrt{\rho_i}u_i}{\partial t} + \frac{1}{4dx}\left(\rho_{i+1}u_{i+1}^2 - \rho_{i-1}u_{i-1}^2 + \rho_i u_i u_{i+1} - \rho_i u_i u_{i-1}\right) \,.$$

5. Temporal integration scheme

For time integration we employ a strongly stable (for deterministic equations) Runge–Kutta temporal integrator (RK3) [29,30]. This time-integration scheme was shown to represent accurately statistical properties for LLNS [15,19]. RK3 has three substeps

$$U^{n+1/3} = U^n - dtdU^n + \sqrt{dt}K^n ,$$
$$U^{n+2/3} = \frac{3}{4}U^n + \frac{1}{4}U^{n+1/3} - \frac{1}{4}dtdU^{n+1/3} + \sqrt{dt}K^{n+1/3} ,$$
$$U^{n+1} = \frac{1}{3}U^n + \frac{2}{3}U^{n+2/3} - \frac{2}{3}dtdU^{n+2/3} + \sqrt{dt}K^{n+2/3} ,$$

where dU is the solution vector, and K is the stochastic-force vector. There are several possibilities for evaluating K at intermediate time steps [19,21]. The following formulation requires only two independent random fields (W_A and W_B)

$$K^{n+1/3} = \alpha_1 W_A + \beta_1 W_B , \quad K^{n+2/3} = \alpha_2 W_A + \beta_2 W_B ,$$
$$K^{n+1} = \alpha_3 W_A + \beta_3 W_B , \tag{22}$$

with the coefficients

$$\alpha_1 = \alpha_2 = \alpha_3 = 1, \ \beta_1 = \frac{2\sqrt{2} \pm \sqrt{3}}{5},$$
$$\beta_2 = \frac{-4\sqrt{2} \pm 3\sqrt{3}}{5}, \ \beta_3 = \frac{\sqrt{2} \mp 2\sqrt{3}}{10} . \tag{23}$$

In the skew-symmetric form we transport $\sqrt{\rho}u$, and at each substep of the RK3 time integration we evaluate

$$(\sqrt{\rho}u)^{n+1} = \frac{1}{\sqrt{\rho^n}}(\rho^n u^n + dtR^n_{skew}) , \tag{24}$$

where R_{skew} is the right-hand side of the semi-discretized GLMEF using one of the spatial schemes given above.

6. Numerical experiments

6.1. Equilibrium

In this section we test numerical methods for GLMEF for the case of stationary fluctuations. For this purpose we choose dissipation and fluctuation coefficients for Argon thermal fluctuations in equilibrium [15]. This case was considered to test numerical methods for the compressible LLNS equations. Here, we want to assess in a similar fashion numerical schemes for the GLMEF equations. The particular choice of parameters is not meant to represent a real physical model of Argon equilibrium fluctuations but rather should facilitate the comparison between LLNS and GLMEF which have different dissipation mechanisms. For that purpose we consider fluctuations around a given mean velocity $u_0(x,t) = 0$

$$\frac{\partial \rho(x,t)}{\partial t} + \frac{\partial g(x,t)}{\partial x} = 0 \tag{25}$$
$$\frac{\partial g(x,t)}{\partial t} + \frac{\partial}{\partial x}\frac{g^2(x,t)}{\rho(x,t)} = -\frac{\partial p(x,t)}{\partial x} - \gamma\rho(x,t)\,(u(x,t) - u_0(x,t)) + \sqrt{\rho(x,t)D\gamma}\,\zeta_c . \tag{26}$$

We take the dissipation coefficient from eq. (15), and the fluctuation coefficient is chosen such that we have the same fluctuation magnitude within the velocity and density fields for GLMEF as for the LLNS in [15]

$$\gamma = \frac{4}{3}\frac{\eta}{\bar{\rho}}k_0^2 ,$$
$$D = \frac{2\sigma_g^2}{\bar{\rho}}, \quad \sigma_g^2 \propto \frac{1}{V_c} . \tag{27}$$

Here, σ_g^2 is the variance of the momentum, k_b is the Boltzmann constant, η is the dynamic viscosity, $\bar{T}$ is a constant temperature, $\bar{\rho}$ denotes the average density, V_c is the constant cell volume. In [15] V_c was chosen to be compatible with DSMC particle simulations. In this paper we choose the same system volume to allow for a comparison of results with [15]. L is the domain size, $k_0 = 2\pi n/L$ is a chosen wave number. The factor of $\sqrt{\frac{2}{\Delta t}}$, originating from Stratonovich integration (time-centered fluxes), is accounted for by the coefficients (23) in eq. (22). $N = 10^7$ time steps for the autocorrelation, PDF and static-structure factor analysis were simulated with $dt = 10^{-11}$. In analogy to LLNS we define the Courant–Friedrichs–Lewy (CFL) numbers as

Table 1
System parameters (in cgs units) for simulation of thermal fluctuations in periodic domain.

Molecular diameter (argon)	3.66×10^{-8}
Molecular mass (argon)	6.63×10^{-23}
Reference mass density ($\bar{\rho}$)	1.78×10^{-3}
Temperature ($\bar{T}$)	273
Artificial sound speed	23843.86
System length (L)	1.25×10^{-4}
Reference mean free path	6.26×10^{-6}
System volume (V_c)	1.96×10^{-16}
Time step (dt)	1.0×10^{-11}
Number of cells (N_c)	40
Number of time steps (N)	10^7
Grid size (dx)	3.13×10^{-6}
Variance of momentum (σ_g^2)	13.34
Fluctuation coefficient (D)	14988.76

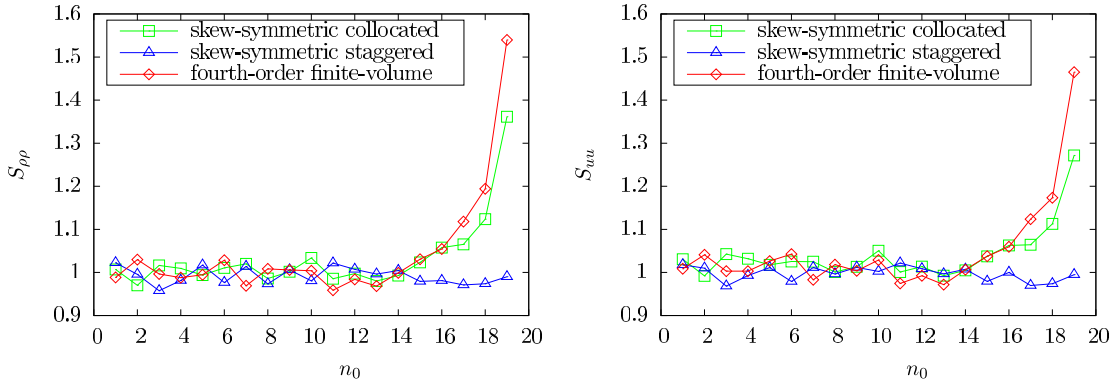

Fig. 1. Comparison of static structure factor $S_{uu}(k)$ and $S_{\rho\rho}(k)$ in thermodynamic equilibrium for different spatial discretization schemes.

$$\alpha_2 = \frac{dx}{(c_s + u_{max})dt} \leq 1, \quad \alpha_1 = \gamma dt \leq \frac{1}{2}.$$

A small CFL number ensures that the spatial truncation error is dominant, and that differences in results originate primarily from the spatial discretization scheme. Parameters are chosen such that the PDF of momentum and velocity are consistent with that of isothermal LLNS. The full set of parameters is given in Table 1.

Eq. (26) has a stochastic forcing in non-conservative (non-divergence) form. As result a non-zero mean velocity u_{av} with variance $\sigma_{av} = \frac{D}{N_c}$ occurs. We suppress this effect by enforcing zero mean of the stochastic force over the (finite) domain. The corrected stochastic force is

$$\zeta_{cor}(x,t) = \zeta(x,t) - L^{-1} \int_L \zeta(x,t)dx$$

at each Runge–Kutta substep. We use the GNU Scientific Library to generate a normal distribution [31].

6.1.1. Static structure factor at equilibrium

An appropriate discretization of the convective term should maintain a discrete fluctuation–dissipation balance, i.e. the computed static structure factor (SSF) should agree with the analytical solution. In section 3.1 it was determined that the SSF for GLMEF is unity, which is consistent with a fluctuation dissipation balance. Fig. 1 shows the results for the numerical solution of the GLMEF equations at equilibrium, discretized with different spatial schemes. We observe that the skew-symmetric staggered schemes results in the best agreement with theory. We also observe that the skew-symmetric collocated scheme for a wide range of wave numbers agrees well with theory and only at large wave numbers, where collocated schemes are known to have inferior wave-resolution properties to staggered schemes, deviates. Both skew-symmetric schemes give better agreement with theory than the fourth-order finite-volume scheme.

We also tested other staggered formulations proposed in [27], i.e. the staggered divergence and advective formulations, which gave results worse than the skew-symmetric staggered and slightly better than the skew-symmetric collocated formulation.

6.1.2. Time correlation at equilibrium

The spectral autocorrelation of density can be derived from the dynamic structure factor (DSF) by applying an inverse Fourier transform. An analytical solution for the spectral autocorrelation can be derived and thus serves also to assess the

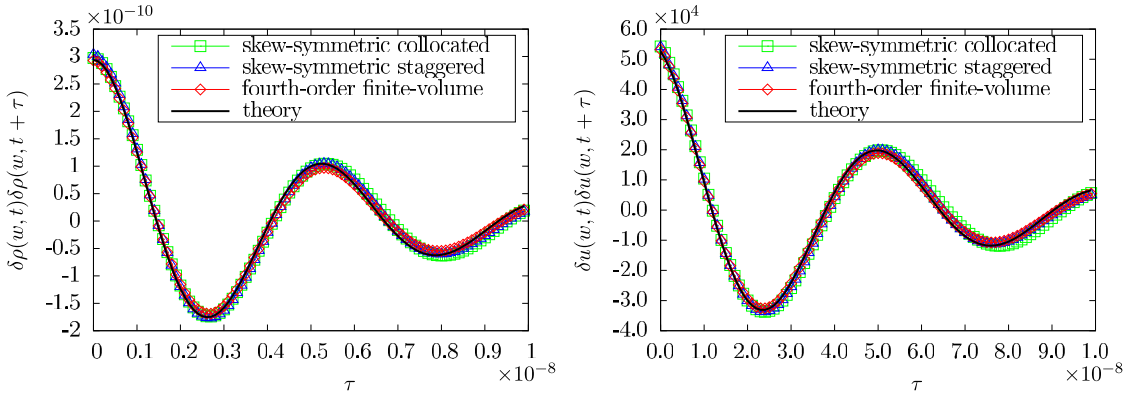

Fig. 2. Time correlation of density and velocity fluctuations at equilibrium for GLMEF for different schemes in comparison with the exact solution Eqs. (12), (13).

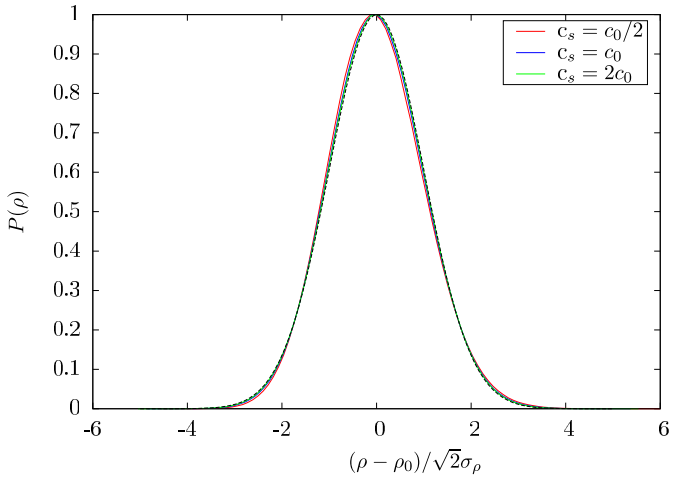

Fig. 3. Density field PDF of GLMEF with skew-symmetric spatial discretization on a staggered grid. Results of simulations with different isothermal speed of sound are compared with a Gaussian function (dashed lines).

prediction accuracy for the DSF. Following [15] we consider the wave number $n_0 = 1$. The dissipation coefficient in GLMEF is chose such that the spectral autocorrelation for GLMEF is equal that isothermal LLNS at wave number $n_0 = 1$. The spectral autocorrelation of density is computed from node values ρ_i by

$$\langle \delta\rho(k,t)\delta\rho(k,t+\tau)\rangle = \frac{1}{N}\sum_{\text{samples}=1}^{N} R(t)R(t+\tau)$$

with

$$R(t) = \frac{1}{N_c}\sum_{l=1}^{N_c} \rho_l \sin(2\pi n x_l/L)\ ,$$

where ρ_l is a cell average of the density field, $l = 1,\ldots,N_c$ is the number of a cell, and N is the number of time steps. Fig. 2 shows a comparison of the different spatial schemes for the spectral autocorrelation of density. We find overall good agreement with theory for all schemes.

6.2. Density probability density function

In this section we consider the PDF of density. We restrict our attention to the skew-symmetric scheme on a staggered grid that gives the best results for the SSF. The difference between the density field PDF of GLMEF $P(\rho)$ and the Gaussian distribution appears to be only minor, irrespective of a variation of the speed of sound, see Fig. 3. Reference speed of sound is $c_0 = 23843.86$ cm/s. Closer inspection is facilitated by a logarithmic plot of

$$\ln[P(\rho)] \sim \left(\frac{\rho - \bar{\rho}}{2\sigma_\rho}\right)^2$$

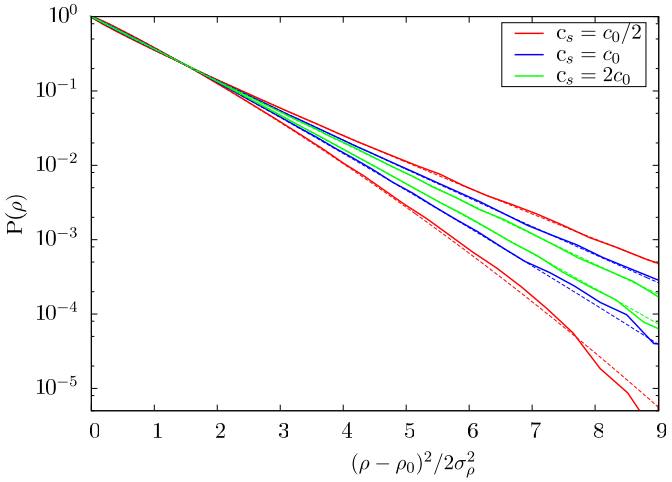

Fig. 4. Solid lines: density PDF of GLMEF with skew-symmetric staggered spatial scheme measured from simulations. Dashed lines: analytical solution eq. (20). Different colors correspond to different values of the speed of sound. Both positive and negative tails are shown. For the variables shown positive and negative tails of the Gaussian PDF coincide. The figure demonstrates that the PDF of GLMEF has non-Gaussian properties.

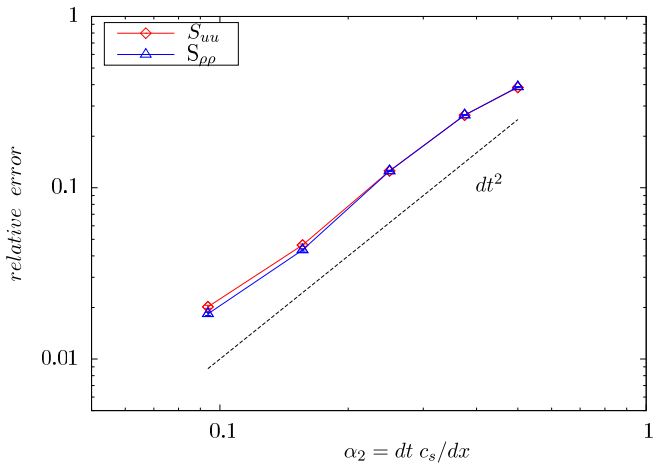

Fig. 5. Convergence study in time of static structure factor $S_{uu}(k)$ and $S_{\rho\rho}(k)$ in thermodynamic equilibrium. Grey dashed line is the theoretical order of convergence $O(dt^2)$.

in Fig. 4. A purely Gaussian distribution would exhibit a straight line. Dashed lines in the figure indicate analytical results, eq. (19), for different isothermal speeds of sound, solid lines are the simulation results for the skew-symmetric staggered scheme. The results show that the scheme correctly predicts skewness and non-Gaussian tails of the density PDF: the deviation from Gaussian behavior increases with decreasing speed of sound. For rare events we observe increasing deviation from the analytical result.

6.3. Weak convergence study

For assessing the weak convergence of the method we consider the deviation of static structure factors $S_{uu}(k)$ and $S_{\rho\rho}(k)$ from their analytical solutions. We vary the time-step size to verify that the solution exhibits the convergence order $\mathcal{O}(dt^2)$. We use the same parameters as given in Table 1. Averaging is performed by sampling results from up to $N = 6.4 \times 10^7$ time steps. Fig. 5 shows the dependence of the relative errors of $S_{uu}(k)$ and $S_{\rho\rho}(k)$ on CFL number α_2 with decreasing time-step size. It can be seen that the algorithm is weakly second-order accurate in time. The skew-symmetric scheme on a staggered grid satisfies the discrete fluctuation–dissipation balance (DFDB) [20] and thus predicts the static structure factors $S_{uu}(k)$ and $S_{\rho\rho}(k)$ within statistical error for the given parameters.

6.4. Nonequilibrium

The problem of standing-shock diffusion was studied previously with DSMC [32] and with lattice–gas simulations [33, 34]. It also has served as test case for investigating nonequilibrium diffusion for different discretization schemes of the LLNS [15,35]. Motivated by this previous research, we simulate fluctuations around a stationary isothermal standing-shock profile for GLMEF. We consider density fluctuations around a given mean shock profile $u_0(x)$. Pre-shock conditions are prescribed as for the previous equilibrium case. Post-shock conditions result from the isothermal Rankine–Hugoniot conditions for two

Table 2
System parameters (in cgs units) for computation of standing isothermal shock, Ma 1.4.

System length (L)	4.0×10^{-3}
RHS mass density	1.78×10^{-3}
LHS mass density	5.81×10^{-3}
RHS velocity (U_{RHS})	-43093.4
LHS velocity (U_{LHS})	-13191.9
Sound speed	23842.86
Time step	1.0×10^{-11}
Number of cells	1280
Collision grid size	3.13×10^{-6}

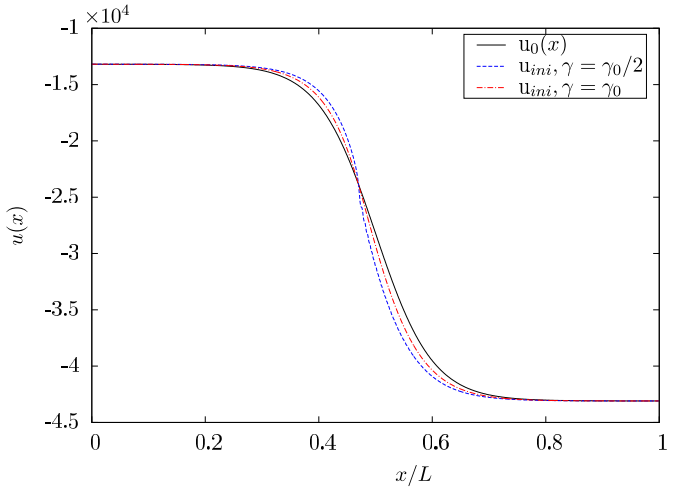

Fig. 6. Initial shock velocity profile $u_0(x)$ (black line) and stationary solution of GLMEF with zero fluctuation coefficient $u_{ini}(x)$. Blue line and red line denote the case of dissipation coefficient equal to $\gamma_0/2$ and γ_0 respectively. Case of $Ma = 1.4$ is presented, $\gamma_0 = 3.9 \times 10^8 \frac{1}{s}$. (For interpretation of the references to color in this figure legend, the reader is referred to the web version of this article.)

different shock strengths at Mach numbers $Ma = 1.2$, $Ma = 1.4$. We approximate infinite reservoir boundaries by setting a constant corresponding velocity at the left and right domain boundaries. To reduce the boundary effect on the fluctuating evolution the domain size is 32 times larger than for the equilibrium case, while keeping the same grid size dx and fluctuation coefficient.

In the absence of physical diffusion the discontinuous initial shock profile tends to develop small-scale disturbances due to truncation errors at large wave numbers. Finite diffusion damps such spurious disturbances and non-dissipative numerical schemes can recover smoothed shock profiles. We consider a smooth initial shock profile that can be well resolved by a non-dissipative scheme by blending pre- and post-shock states with a hyperbolic tangent

$$u_0(x) = \frac{1}{2}\left(U_{LHS} - U_{RHS}\right)\left(1 - \tanh\left(C_{shock}\frac{x - L}{L}\right)\right).$$

This prevents spurious errors from polluting density fluctuations around the standing shock. The parameters for the standing isothermal shock are given in Table 2. We choose $C_{shock} = 10$ to maintain a smooth stationary solution in case of vanishing fluctuations. To avoid initial velocity and density relaxation, we initialize domain with velocity $u(x, 0) = u_{ini}(x)$ that is derived from a precursor simulation of GLMEF with zero fluctuating coefficient, Fig. 6.

We measure the shock location at every time step from the average density field by

$$\sigma_\rho(t) = L\frac{\bar{\rho}(t) - (1/2)(\rho_L + \rho_R)}{\rho_L - \rho_R},$$

where

$$\bar{\rho} = L^{-1}\int_{-L/2}^{L/2}\rho(x, t)dx \tag{28}$$

is the instantaneous spatially averaged density.

We emphasize that the setup should not be considered as an accurate representation for the shock-diffusion problem. It serves here rather as a simple configuration to assess isothermal nonequilibrium fluctuations. The equation of state was

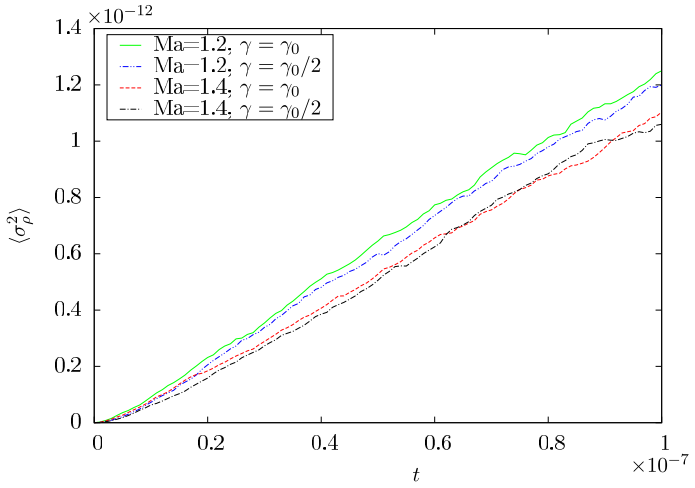

Fig. 7. Variance of shock location for density field in case of isothermal shock set up for weakly compressible GLMEF. The late-time growth rate of the density field variance in case of GLMEF keeps constant in time as for random walk model and depends neither on Mach number nor dissipation coefficient. $\gamma_0 = 3.9 \times 10^8 \frac{1}{s}$.

chosen for simplicity and with the objective of analyzing the weakly compressible form of GLMEF. Moreover, the setup of simulation does not take into account fluctuations of the mean shock profile $u_0(x,t)$. Nevertheless, the setup serves to investigate diffusion properties of GLMEF fluctuations around a non-trivial one-dimensional mean flow with steep gradients. The shock location fluctuates in time, and we are interested in changes of the variance of shock-location. If the numerical model properly captures thermal fluctuations of the shock, the shock location should diffuse similar to that of a simple random walk [34,15].

Fig. 7 shows the results for the late-time location variance of the isothermal shock over time. The variance is estimated by averaging over 1000 simulation samples. In comparison with the compressible equation of state, the location variance for the weakly compressible equation of state does not depend on shock strength when GLMEF is considered. The variance of shock location has the same slopes for $Ma = 1.2$ and $Ma = 1.4$

7. Discussion

We have addressed the question of suitable numerical discretization schemes for GLMEF which has structural similarity with an isothermal version of the Landau–Lifshitz Navier–Stokes equations, albeit the dissipative mechanism and stochastic force are different. This similarity has motivated us to follow a similar analysis for GLMEF as other authors previously have performed for LLNS, and propose a combination of a staggered skew-symmetric finite-difference discretization of convective terms and a strongly stable (for deterministic equations) three-stage Runge–Kutta scheme. We find that previous approaches suggested for LLNS do not necessarily perform well for GLMEF. By considering finite-difference schemes that have been designed particularly for good wave resolution and discrete conservation properties [27] we find that the better wave-resolution properties that staggered schemes have over their collocated counterparts for deterministic equations transfer to the stochastic equations. Furthermore, the reduction of aliasing errors due to the skew-symmetric formulation [36] also leads in the stochastic case to improved numerical stability.

The proposed staggered skew-symmetric spatial discretization gives a correct prediction of the static structure factor and recovers non-Gaussian behavior of the density PDF. A finite-volume fourth-order spatial discretization scheme [15] results in a significant deviation from the analytical solution. This observation is consistent with the results for LLNS [19]. The observation that a staggered scheme is superior to a collocated scheme for the GLMEF also is consistent with previous studies for LLNS [20]. The choice of a suitable scheme for the spatial discretization is particularly important for GLMEF. We show that the considered collocated schemes exhibit a larger deviation from analytical results for GLMEF than for isothermal LLNS, and that only the staggered scheme in both cases equations returns satisfactory predictions. The fact that GLMEF is more sensitive to numerical errors may be due to the dissipation mechanism differing from that of LLNS.

The Generalized Langevin Model without repulsive potential is widely used to model turbulent flows. Its relation to intermittency effects on the velocity structure factor and energy-dissipation-rate structure function was shown in [37]. The difference from GLMEF considered in this paper is due to the presence of a repulsive potential by including a pressure from a weakly-compressible equation of state in GLMEF. One objective of this extension is to regularize the SPDEs in order to facilitate stable numerical solution.

The GLMEF model considered in this paper has the potential to capture non-Gaussian density PDF when discretized with a grid-based method. We consider this property as important for an application as subgrid-scale model for turbulent flows. We have employed in this paper only a very simple weakly-compressible equation of state to model the repulsive potential between notional particles. The analysis of other equations of state is the subject of future work. The further development of GLMEF might help to merge the well established subgrid-scale reconstruction properties of the particle

based Lagrangian-frame numerical solution approaches [38] with the efficiency of grid-based Eulerian methods [9], and thus offers a unified approach to Large-Eddy and Reynolds-averaged modeling of turbulent flows. It can be speculated that GLMEF with repulsive potential might extend the applicability of GLMEF-based subgrid-scale models to more complex turbulent flows than considered so far.

GLMEF may also lead to new applications as mesoscale models for nonequilibrium thermodynamics in liquids. There is a correspondence between Landau–Lifshitz Navier–Stokes and the overdamped Langevin equation described by R.F. Fox and G.E. Uhlenbeck [39,40]. In the manuscript we consider the underdamped Langevin equation which has the potential to extend the numerical investigation of nonequilibrium fluctuating phenomena in liquids [12]. These developments are subject of current work.

Acknowledgements

The authors wish to thank Vladimir Sabelnikov, Xiangyu Hu and Felix S. Schranner for helpful discussions. The first author acknowledges travel support due to the TUM Graduate School. We thank the Munich Center of Advanced Computing for providing computational resources. We thank Anna Lukyanovich for proofreading.

References

[1] S. Pope, PDF methods for turbulent reactive flows, Prog. Energy Combust. Sci. 11 (2) (1985) 119–192, http://dx.doi.org/10.1016/0360-1285(85)90002-4, http://www.sciencedirect.com/science/article/pii/0360128585900024, 01876.
[2] D.C. Haworth, Progress in probability density function methods for turbulent reacting flows, Prog. Energy Combust. Sci. 36 (2) (2010) 168–259, http://dx.doi.org/10.1016/j.pecs.2009.09.003, http://www.sciencedirect.com/science/article/pii/S036012850900046X, 00230.
[3] L. Valiño, A field Monte Carlo formulation for calculating the probability density function of a single scalar in a turbulent flow, Flow Turbul. Combust. 60 (2) (1998) 157–172, http://dx.doi.org/10.1023/A:1009968902446, http://link.springer.com/article/10.1023/A%3A1009968902446, 00125.
[4] V. Sabelnikov, O. Soulard, Rapidly decorrelating velocity-field model as a tool for solving one-point Fokker–Planck equations for probability density functions of turbulent reactive scalars, Phys. Rev. E 72 (1) (2005) 016301, http://dx.doi.org/10.1103/PhysRevE.72.016301, 00068.
[5] O. Soulard, V.A. Sabelnikov, Eulerian Monte Carlo method for the joint velocity and mass-fraction probability density function in turbulent reactive gas flows, Combust. Explos. Shock Waves 42 (6) (2006) 753–762, http://dx.doi.org/10.1007/s10573-006-0111-x, http://link.springer.com/article/10.1007/s10573-006-0111-x, 00018.
[6] V. Sabel'nikov, O. Soulard, Eulerian (field) Monte Carlo methods for solving PDF transport equations in turbulent reacting flows, in: Handbook of Combustion, Wiley-VCH Verlag GmbH & Co. KGaA, 2010, http://onlinelibrary.wiley.com/doi/10.1002/9783527628148.hoc043/abstract, 00004.
[7] C. Emako, V. Letizia, N. Petrova, R. Sainct, R. Duclous, O. Soulard, Diffusion limit of the simplified Langevin PDF model in weakly inhomogeneous turbulence, ESAIM: Proc. Surv. 48 (2015) 400–419, http://dx.doi.org/10.1051/proc/201448019, http://www.esaim-proc.org/10.1051/proc/201448019.
[8] N. Petrova, Turbulence–chemistry interaction models for numerical simulation of aeronautical propulsion systems, PhD thesis Ecole Polytechnique X, Jan. 2015, https://pastel.archives-ouvertes.fr/tel-01113856/document, 00001.
[9] N.A. Adams, A stochastic extension of the approximate deconvolution model, Phys. Fluids 23 (5) (2011) 055103, http://dx.doi.org/10.1063/1.3584129, http://link.aip.org/link/PHFLE6/v23/i5/p055103/s1&Agg=doi, 00001.
[10] S. Stolz, N.A. Adams, An approximate deconvolution procedure for large-eddy simulation, Phys. Fluids 11 (7) (1999) 1699–1701, http://dx.doi.org/10.1063/1.869867, http://pof.aip.org/resource/1/phfle6/v11/i7/p1699_s1.
[11] S. Stolz, N.A. Adams, L. Kleiser, An approximate deconvolution model for large-eddy simulation with application to incompressible wall-bounded flows, Phys. Fluids 13 (4) (2001) 997–1015, http://dx.doi.org/10.1063/1.1350896, http://pof.aip.org/resource/1/phfle6/v13/i4/p997_s1, 00369.
[12] T. Nakamura, A. Yoshimori, Derivation of the nonlinear fluctuating hydrodynamic equation from the underdamped Langevin equation, J. Phys. A, Math. Theor. 42 (6) (2009) 065001, http://dx.doi.org/10.1088/1751-8113/42/6/065001, http://iopscience.iop.org/1751-8113/42/6/065001, 00006.
[13] D.S. Dean, Langevin equation for the density of a system of interacting Langevin processes, J. Phys. A, Math. Gen. 29 (24) (1996) L613–L617, http://dx.doi.org/10.1088/0305-4470/29/24/001, http://iopscience.iop.org/0305-4470/29/24/001, 00068.
[14] G. De Fabritiis, M. Serrano, R. Delgado-Buscalioni, P.V. Coveney, Fluctuating hydrodynamic modeling of fluids at the nanoscale, Phys. Rev. E 75 (2) (2007) 026307, http://dx.doi.org/10.1103/PhysRevE.75.026307, 00051.
[15] J.B. Bell, A.L. Garcia, S.A. Williams, Numerical methods for the stochastic Landau–Lifshitz Navier–Stokes equations, Phys. Rev. E 76 (1) (2007) 016708, http://dx.doi.org/10.1103/PhysRevE.76.016708, 00038.
[16] J.B. Bell, A.L. Garcia, S.A. Williams, Computational fluctuating fluid dynamics, ESAIM: Math. Model. Numer. Anal. 44 (5) (2010) 1085–1105, http://dx.doi.org/10.1051/m2an/2010053, http://www.esaim-m2an.org/10.1051/m2an/2010053, 00035.
[17] A. Donev, J.B. Bell, A. de la Fuente, A.L. Garcia, Diffusive transport by thermal velocity fluctuations, Phys. Rev. Lett. 106 (20) (2011) 204501, http://dx.doi.org/10.1103/PhysRevLett.106.204501, 00031.
[18] J. Monaghan, Smoothed particle hydrodynamics and its diverse applications, Annu. Rev. Fluid Mech. 44 (1) (2012) 323–346, http://dx.doi.org/10.1146/annurev-fluid-120710-101220, 00148.
[19] A. Donev, E. Vanden-Eijnden, A. Garcia, J. Bell, On the accuracy of finite-volume schemes for fluctuating hydrodynamics, Commun. Appl. Math. Comput. Sci. 5 (2) (2010) 149–197, http://dx.doi.org/10.2140/camcos.2010.5.149, http://msp.org/camcos/2010/5-2/p01.xhtml.
[20] F. Balboa, J.B. Bell, R. Delgado-Buscalioni, A. Donev, T.G. Fai, B.E. Griffith, C.S. Peskin, Staggered schemes for fluctuating hydrodynamics, Multiscale Model. Simul. 10 (4) (2012) 1369–1408, http://dx.doi.org/10.1137/120864520, http://epubs.siam.org/doi/abs/10.1137/120864520, 00024.
[21] S. Delong, B.E. Griffith, E. Vanden-Eijnden, A. Donev, Temporal integrators for fluctuating hydrodynamics, Phys. Rev. E 87 (3) (2013) 033302, http://dx.doi.org/10.1103/PhysRevE.87.033302, 00010.
[22] P.J. Atzberger, Spatially adaptive stochastic numerical methods for intrinsic fluctuations in reaction–diffusion systems, J. Comput. Phys. 229 (9) (2010) 3474–3501, http://dx.doi.org/10.1016/j.jcp.2010.01.012, http://www.sciencedirect.com/science/article/pii/S0021999110000276, 00022.
[23] B.J. Berne, R. Pecora, Physics, Dynamic Light Scattering: With Applications to Chemistry, Biology, and Physics, unabridged edition, Dover Publications, 2000.
[24] J.P. Boon, S. Yip, Molecular Hydrodynamics, Dover Publications, 1992.
[25] Maxima, Maxima, a computer algebra system, version 5.34.1, http://maxima.sourceforge.net/.
[26] N.K. Voulgarakis, J.-W. Chu, Bridging fluctuating hydrodynamics and molecular dynamics simulations of fluids, J. Chem. Phys. 130 (13) (2009) 134111, http://dx.doi.org/10.1063/1.3106717, http://scitation.aip.org/content/aip/journal/jcp/130/13/10.1063/1.3106717, 00037.

[27] Y. Morinishi, Skew-symmetric form of convective terms and fully conservative finite difference schemes for variable density low-Mach number flows, J. Comput. Phys. 229 (2) (2010) 276–300, http://dx.doi.org/10.1016/j.jcp.2009.09.021, http://www.sciencedirect.com/science/article/pii/S0021999109005130, 00026.
[28] S.K. Lele, Compact finite difference schemes with spectral-like resolution, J. Comput. Phys. 103 (1) (1992) 16–42, http://dx.doi.org/10.1016/0021-9991(92)90324-R, http://www.sciencedirect.com/science/article/pii/002199919290324R.
[29] S. Gottlieb, C.W. Shu, Total variation diminishing Runge–Kutta schemes, Math. Comput. 67 (221) (1998) 73–85, http://dx.doi.org/10.1090/S0025-5718-98-00913-2, 00941, WOS:000071947700004.
[30] J.X. Qiu, C.W. Shu, Runge–Kutta discontinuous Galerkin method using WENO limiters, SIAM J. Sci. Comput. 26 (3) (2005) 907–929, http://dx.doi.org/10.1137/S1064827503425298, 00125, WOS:000227761300009.
[31] B. Gough, GNU Scientific Library Reference Manual, 3rd edition, Network Theory Ltd., 2009.
[32] G.A. Bird, Molecular Gas Dynamics and the Direct Simulation of Gas Flows, 2nd edition, Oxford University Press, USA, 1994, 00054.
[33] F.J. Alexander, S.A. Janowsky, J.L. Lebowitz, H. van Beijeren, Shock fluctuations in one-dimensional lattice fluids, Phys. Rev. E 47 (1) (1993) 403–410, http://dx.doi.org/10.1103/PhysRevE.47.403, 00017.
[34] P.A. Ferrari, L.R.G. Fontes, Shock fluctuations in the asymmetric simple exclusion process, Probab. Theory Relat. Fields 99 (2) (1994) 305–319, http://dx.doi.org/10.1007/BF01199027.
[35] A. Pandey, A. Klar, S. Tiwari, Meshfree method for fluctuating hydrodynamics, Math. Comput. Simul. 82 (11) (2012) 2157–2166, http://dx.doi.org/10.1016/j.matcom.2012.06.002, http://www.sciencedirect.com/science/article/pii/S0378475412001310.
[36] G.A. Blaisdell, N.N. Mansour, W.C. Reynolds, Compressibility effects on the growth and structure of homogeneous turbulent shear flow, J. Fluid Mech. 256 (1993) 443–485, http://dx.doi.org/10.1017/S0022112093002848, http://journals.cambridge.org/article_S0022112093002848, 00140.
[37] H. Fujisaka, Y. Nakayama, Intermittency and exponent field dynamics in developed turbulence, Phys. Rev. E 67 (2) (2003) 026305, http://dx.doi.org/10.1103/PhysRevE.67.026305, 00003.
[38] S.B. Pope, Turbulent Flows, Cambridge University Press, 2000, 05223.
[39] R.F. Fox, G.E. Uhlenbeck, Contributions to non-equilibrium thermodynamics. I. Theory of hydrodynamical fluctuations, Phys. Fluids 13 (8) (1970) 1893–1902, http://dx.doi.org/10.1063/1.1693183, http://pof.aip.org/resource/1/pfldas/v13/i8/p1893_s1, 00246.
[40] R.F. Fox, G.E. Uhlenbeck, Contributions to nonequilibrium thermodynamics. II. Fluctuation theory for the Boltzmann equation, Phys. Fluids 13 (12) (1970) 2881–2890, http://dx.doi.org/10.1063/1.1692878, http://pof.aip.org/resource/1/pfldas/v13/i12/p2881_s1, 00123.

A.2 Determination of macroscopic transport coefficients of dissipative particle dynamics solvent

As of October 25, 2018 the American Physical Society (APS) regulations state that "the author has the right to use the article or a portion of the article in a thesis or dissertation without requesting permission from APS, provided the bibliographic citation and the APS copyright credit line are given on the appropriate pages."

Determination of macroscopic transport coefficients of a dissipative particle dynamics solvent

Dmitrii Azarnykh,[1,*] Sergey Litvinov,[2] Xin Bian,[3] and Nikolaus A. Adams[1]
[1]*Institute of Aerodynamics and Fluid Mechanics, Technische Universität München, Garching, Germany*
[2]*Chair for Computational Science, Eidgenössische Technische Hochschule Zürich, Zurich, Switzerland*
[3]*Division of Applied Mathematics, Brown University, Providence, Rhode Island 02912, USA*
(Received 30 September 2015; revised manuscript received 15 December 2015; published 11 January 2016)

We present an approach to determine macroscopic transport coefficients of a dissipative particle dynamics (DPD) solvent. Shear viscosity, isothermal speed of sound, and bulk viscosity result from DPD-model input parameters and can be determined only *a posteriori*. For this reason approximate predictions of these quantities are desirable in order to set appropriate DPD input parameters. For the purpose of deriving an improved approximate prediction we analyze the autocorrelation of shear and longitudinal modes in Fourier space of a DPD solvent for Kolmogorov flow. We propose a fitting function with nonexponential properties which gives a good approximation to these autocorrelation functions. Given this fitting function we improve significantly the capability of *a priori* determination of macroscopic solvent transport coefficients in comparison to previously used exponential fitting functions.

DOI: 10.1103/PhysRevE.93.013302

I. INTRODUCTION

The dissipative particle dynamics (DPD) method is a stochastic numerical model for the representation of mesoscale phenomena in fluids. It was first suggested by Hoogerbrugge and Koelman [1]. DPD is widely applied in physics and engineering science. It has been used for, among others, modeling of polymer solutions [2], red blood cells [3], and colloidal suspensions [4,5]. One of the main complications of the DPD method lies in determining effective macroscopic fluid coefficients, such as viscosity and compressibility. Such macroscopic transport coefficients are indirectly determined by a set of DPD input parameters which are essentially of microscopic nature. A relation between DPD and molecular dynamics with Lennard-Jones potential was demonstrated in [6]. In contrast to DPD, smoothed dissipative particle dynamics (SDPD) has an inherently macroscopic nature, and macroscopic transport coefficients characterized by shear and bulk viscosities and isothermal speed of sound have a direct correspondence to SDPD input parameters. SDPD was first proposed in [7] as a stochastic extension of the smoothed particle hydrodynamics (SPH) method to the mesoscale [8]. For that reason SDPD is limited to the classical hydrodynamic regime of fluids, where macroscopic transport coefficients do not depend on length scales. It should be pointed out that the SDPD model and the Landau-Lifshitz Navier-Stokes (LLNS) equations are related to each other for certain input-parameter ranges [9]. As SDPD and LLNS are limited to the classical hydrodynamic regime, the challenge of finding a relation between macroscopic and DPD input parameters cannot be solved through modeling a DPD solvent with SDPD or LLNS. A variety of methods have been proposed to estimate macroscopic transport coefficients for a DPD solvent. The common approach is to expose a DPD solvent to a body force which is constant in time. The shear viscosity can then be derived directly from the response of the solvent to such a perturbation. Fan *et al.* [10] used wall-bounded Poiseuille flow to asses the viscosity of a DPD solvent in a microchannel. A constant body force was applied in the wall-parallel direction, and the channel walls were modeled as frozen solvent particles. The same method was used to estimate the viscosity of a polymer suspension in a microchannel. It is also possible to estimate the viscosity of a DPD solvent by using a reverse Poiseuille flow [11–13], which implies the application of equal body forces with opposite direction in each half of the periodic domain. Another approach to estimate shear viscosity is to employ the Green-Kubo method which can lead to inaccuracies at small scales and may require additional corrections [14]. The Green-Kubo method as well as Poiseuille flow allow us to estimate the shear viscosity only on the length scale which is predefined by the initial conditions. If the shear viscosity does not depend on the length scale, as is the case for the Navier-Stokes equations, this approach is sufficient to predict dissipation on the different length scales. However, a DPD solvent has a more complicated relation between dissipation and length scales which is defined by the DPD weighting function and DPD dissipation as well as the repulsive potential. Another limitation is that stationary Poiseuille flow methods are unable to predict other macroscopic transport coefficients such as the bulk viscosity of a DPD solvent or its isothermal speed of sound. The dissipation in a DPD solvent without potential was widely analyzed in the classical works on DPD [15–17]. Predictions for the length scale dependency of macroscopic transport coefficients have been derived analytically from the DPD Fokker-Planck equation. In the analytical derivation of macroscopic transport coefficients some assumptions were imposed such as the absence of a potential between DPD particles. The main disadvantage of a DPD fluid without conservative force is due to the fact that the equation of state of such a fluid becomes that of an ideal gas [17]. It thus limits the model applicability. In [17] it was suggested to estimate macroscopic transport coefficients of a DPD solvent from the approximation of the Fourier transform of the velocity autocorrelation functions (FTVACF) with an exponential function. The approximation of FTVACF modes with an exponential function might introduce additional errors in the

*d.azarnykh@tum.de

estimation of shear viscosity [11]. It was demonstrated that when FTVACF modes are exponential (in the limit of long time and large length scale $\omega \to 0, k \to 0$) the viscosity estimated with the Green-Kubo method equals that estimated from the first FTVACF mode [14,20]. In principle one can consider the Green-Kubo method as a particular case of the more general FTVACF analysis. In this work we consider a DPD solvent with repulsive potential and show that an assumption of exponential decay of FTVACF modes implies additional errors in the estimation of macroscopic transport coefficients for a DPD solvent. The estimation of viscosity from FTVACF modes is well established for particle methods. The analysis of FTVACF in a multiparticle collision dynamics (MPC) solvent is described in [18], where an exponential function was used to estimate macroscopic transport coefficients of MPC. When the FTVACF-mode decay is not purely exponential, it may be useful to introduce a so-called memory function. Palmer [14] analyzed the transverse-current autocorrelation function for molecular dynamics with an exponential model of the memory function. The method also was compared with an estimate of the shear viscosity from Green-Kubo and Poiseuille flows for molecular dynamics [19]. Other models for the memory function are described in [20]. In this paper we analyze FTVACF modes of a DPD solvent in three spatial dimensions. We approximate the nonexponential evolution of FTVACF modes in a DPD solvent. For that purpose we introduce a function with nonexponential decay and calibrate its transport coefficients. This function gives a good approximation to the modes of FTVACF of a DPD solvent. We show that the analysis of FTVACF modes can be used to derive the wave-number dependence of the shear viscosity, the isothermal speed of sound, and the bulk viscosity of a DPD solvent. The paper is structured in the following way. After summarizing the DPD solvent model in the second section, we derive the shear viscosity on different scales from an analysis of Kolmogorov flows in the third section. In the fourth section we analyze the response of a DPD solvent on linear perturbations. We perform simulations for the decay of sinusoidal waves in longitudinal and transverse directions. For the case of sinusoidal wave decay we compare the maximum velocities at different wave numbers. In the same section the nonexponential nature of FTVACF is shown. We define the Fourier transform of the density autocorrelation function (FTDACF) to estimate the accuracy of prediction of macroscopic transport coefficients. We also introduce a function that improves the approximation of FTVACF modes of a DPD solvent in comparison with an exponential function. In the fifth section we compare the accuracy of the methods that can be used to derive macroscopic transport coefficients. We change the input parameters of the DPD solvent in the sixth section in order to assess applicability limits of the approach.

II. THE DPD METHOD

We consider a set of identical particles interacting with each other with a pairwise force F_{ij}. The law of motion for the ith particle is described by

$$\frac{d\boldsymbol{r}_i}{dt} = \boldsymbol{v}_i, \quad \frac{d\boldsymbol{v}_i}{dt} = \frac{1}{m}\sum_{j\neq i} \boldsymbol{F}_{ij}. \tag{1}$$

Here we take mass of the particle equal to unity. The force can be split into three parts:

$$\boldsymbol{F}_{ij} = \boldsymbol{F}^C_{ij} + \boldsymbol{F}^D_{ij} + \boldsymbol{F}^R_{ij}. \tag{2}$$

The pairwise forces have a cutoff radius r_c which we take as unity as well. The conservative force is repulsive between particles and acts along the connecting line between two particles:

$$\boldsymbol{F}^C_{ij} = \begin{cases} a_{ij} m(1 - r_{ij})\hat{\boldsymbol{r}}_{ij}, & r_{ij} < r_c \\ 0, & r_{ij} \geqslant r_c \end{cases}, \tag{3}$$

where a_{ij} is the maximum repulsion between the particles; $\boldsymbol{r}_{ij} = \boldsymbol{r}_i - \boldsymbol{r}_j$, $r_{ij} = |\boldsymbol{r}_{ij}|$, and $\hat{\boldsymbol{r}}_{ij} = \boldsymbol{r}_{ij}/r_{ij}$ are relative position, distance, and unit vector between two particles i and j, respectively. Dissipative and random forces are

$$\boldsymbol{F}^D_{ij} = -\gamma m w_D(r_{ij})(\hat{\boldsymbol{r}}_{ij} \cdot \boldsymbol{v}_{ij})\hat{\boldsymbol{r}}_{ij} \tag{4}$$

and

$$\boldsymbol{F}^R_{ij} = \sigma m w_R(r_{ij})\theta_{ij}\hat{\boldsymbol{r}}_{ij}, \tag{5}$$

respectively, where γ and σ are dissipative and random coefficients. $w^D(r_{ij})$ and $w^R(r_{ij})$ are weighting functions, $\boldsymbol{v}_{ij} = \boldsymbol{v}_i - \boldsymbol{v}_j$ is the relative velocity, and θ_{ij} is a random function with the properties

$$\langle \theta_{ij}(t) \rangle = 0, \tag{6}$$

$$\langle \theta_{ij}(t)\theta_{kl}(t') \rangle = (\delta_{ik}\delta_{jl} + \delta_{il}\delta_{jk})\delta(t - t'), \tag{7}$$

with $i \neq j$, $k \neq l$. The coefficients of the random and dissipative forces are related such that they satisfy the fluctuation-dissipation balance [21]

$$w^D(r_{ij}) = [w^R(r_{ij})]^2, \quad \gamma = \frac{\sigma^2}{2k_B T}, \tag{8}$$

where k_B is the Boltzmann constant and T is the temperature. We choose the standard weighting functions [2]

$$w^D(r_{ij}) = [w^R(r_{ij})]^2 = \begin{cases} (1 - r_{ij})^2, & r_{ij} < r_c \\ 0, & r_{ij} \geqslant r_c \end{cases}. \tag{9}$$

The velocity Verlet algorithm is used for time integration. Simulations in this work are performed with the LAMMPS open-source code [22].

Nondimensional transport coefficients

DPD can represent dynamics of a fluid in different scale regimes. On the large scales DPD obeys laws of classical hydrodynamics. On the small scales the dynamics of a DPD solvent differ from classical hydrodynamics. As scaling parameters that separate the dynamic regimes of a DPD solvent one may take a decorrelation length of DPD particles l_0 and the cutoff length r_c. Here we follow [17] and choose nondimensional transport coefficients as presented in Table I. We choose the mass of DPD particles m as a mass unit, the collision time t_0 as time unit, and the dynamic length l_0 as a length unit. We nondimensionalize transport coefficients such as kinematic shear viscosity, kinematic bulk viscosity, and isothermal speed of sound according to the chosen system of units. Nondimensional transport coefficients will be used in Sec. VI.

TABLE I. Scaling ratios for DPD nondimensional transport coefficients.

ν	Kinematic shear viscosity	$\nu = \frac{\eta_s}{\rho}$
ζ	Kinematic bulk viscosity	$\zeta = \frac{\eta_v}{\rho}$
v_0	Thermal velocity	$\sqrt{k_B T/m}$
$[\boldsymbol{r} w_D]_r$	Integral of w_D	$[\boldsymbol{r} w_D]_r = \int_0^{r_c} w_D(\boldsymbol{r}) d\boldsymbol{r}$
ω_0	Collision frequency	$\omega_0 = \rho[\boldsymbol{r} w_D]_r \gamma/d$
t_0	Collision time	$t_0 = \frac{1}{\omega_0}$
l_0	Dynamic distance	$l_0 = t_0 v_0$
Ω_0	Dynamic overlapping	$\Omega_0 = \frac{r_c}{l_0}$
$\tilde{k}$	Nondimensional wave number	$\tilde{k} = k l_0$
$\tilde{\nu}$	Nondimensional ν	$\tilde{\nu} = \frac{\nu}{\omega_0 l_0^2}$
$\tilde{\zeta}$	Nondimensional ζ	$\tilde{\zeta} = \frac{\zeta}{\omega_0 l_0^2}$
$\tilde{c}_t$	Nondimensional c_t	$\tilde{c}_t = \frac{c_t}{\omega_0 l_0}$

III. KOLMOGOROV FLOW OF SIMPLE DPD FLUID

One common approach to asses shear viscosity of a DPD system is to expose the DPD solvent to a temporally constant body force [10]. In this work we choose a sinusoidal spatial dependence for the body force that acts on the solvent. This particular choice of the force is motivated by convenience: sinusoidal waves have simple Fourier representations. We are interested in the low Reynolds number regime where nonlinear effects of the solvent are negligible. The choice of sinusoidal waves corresponds to the Kolmogorov-flow configuration which allows us to measure viscosity at any prescribed wave number [23,24]. We consider a body force

$$\boldsymbol{F} = F_0(k_z)\sin(k_z x)\hat{\boldsymbol{x}}, \tag{10}$$

where $k_z = 2\pi n/L_z$ is the z component of a wave-number vector, L_z is the extent of the simulation box in the z direction, n is an integer wave number, and $F_0(k_z)$ is a body force that depends on the wave-number vector in a way that will be described below. For small Reynolds number $\mathrm{Re} < \sqrt{2}$, one can obtain an analytical stationary solution

$$\boldsymbol{v} = v_0 \sin(k_z x)\hat{\boldsymbol{x}}, \tag{11}$$

with $v_0 = \frac{F_0(k_z)\rho}{m\eta_s k_z^2}$. The Reynolds number is defined as

$$\mathrm{Re} = \frac{F_0(k_z)}{m\nu^2 k_z^3}. \tag{12}$$

To estimate the viscosity law $\eta_s(k)$ we perform separate simulations for different k_z. For every simulation we take the body force $F_0(k_z)$ in such a way as to maintain $\mathrm{Re} \in [0.2, 0.3]$ for $L_z = 40$. An empirical expression for $F_0(k_z)$ is

$$F_0(k_z) = \begin{cases} 0.0199\, k_z^3, & k_z < \frac{2\pi\times 14}{40} \\ 0.00125\, k_z^2, & k_z \geqslant \frac{2\pi\times 14}{40} \end{cases}. \tag{13}$$

The simulation input parameters are described in Table II and are taken from [10]. To assess the shear viscosity, for every k_z we perform a preliminary simulation for a sufficiently long time until the Kolmogorov flow becomes stationary. Subsequently, for the developed stationary flow we evaluate

TABLE II. Input parameters of the DPD solvent for Kolmogorov flow.

Domain size ($L_x \times L_y \times L_z$)	$40 \times 40 \times 40$
Mass (m)	1
Temperature ($k_B T$)	1
Stochastic coefficient (σ)	3
Dissipative coefficient (γ)	$\sigma^2/(2k_B T)$
Repulsion coefficient (a_{ij})	18.75
Time step (dt)	0.01
Density (ρ)	4
Prerun length in time steps	4×10^5
Simulation length in time steps (N_t)	32×10^5

N_i samples from every simulation. Every sample represents an independent instantaneous velocity profile. We approximate each sample of the velocity profiles with a sinusoidal function (11) to extract the maximum velocity v_0. From the value of v_0 we estimate the shear viscosity η_s for every k_z. We find the statistical error of the shear viscosity estimation from the standard deviation of η_s. To achieve an error in viscosity estimation of less than 1%, we extend the simulation for the first integer wave number $n = 1$ up to $16 \times N_t$ time steps and for the second integer wave number $n = 2$ up to $8 \times N_t$ time steps, and so forth, where N_t is given in Table II. Figure 1 shows the velocity profiles averaged from N_i samples for $n = 1$ and 4. We consider the shear viscosity, estimated from Kolmogorov flow as a reference for the remainder of the paper. The viscosity law $\eta_s(k)$ which has been derived from this method is shown in Fig. 5.

IV. DPD RESPONSE ON LINEAR PERTURBATIONS

In this section we consider the linear response of a DPD solvent on perturbations. Such perturbations can be imposed by initial conditions in terms of longitudinal and transverse waves. Another option is to consider the transport and dissipation of equilibrium fluctuations. In the linear case the dissipation of random velocity fluctuations obeys the same dissipative evolution as the relaxation of an initially imposed velocity field. The correspondence of the two approaches was shown in [25] for fluctuating hydrodynamics. For a DPD solvent such a correspondence will be shown below. From the linear response of a DPD solvent one can derive the length scale dependence of macroscopic transport coefficients.

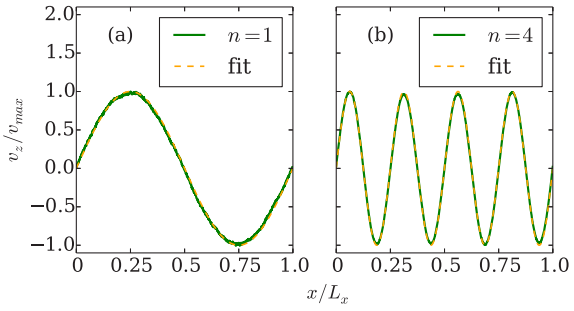

FIG. 1. Velocity profiles for different integer wave numbers and their analytical approximation (11). The statistical error is less than 1%.

TABLE III. Input parameters of the DPD solvent for the decay of sinusoidal waves.

Domain size ($L_x \times L_y \times L_z$)	$20 \times 20 \times 20$
Mass (m)	1
Temperature (k_BT)	1
Stochastic coefficient (σ)	3
Dissipative coefficient (γ)	$\sigma^2/(2k_BT)$
Repulsion coefficient (a_{ij})	18.75
Time step (dt)	0.01
Density (ρ)	4
Prerun length in time steps (N_{prerun})	4.8×10^4
Simulation length in time steps (N_{run})	1.2×10^4
Number of realization (N_{seed})	1000

A. Decay of sinusoidal waves

Considering the decay of sinusoidal waves allows us to asses the scale dependence not only of shear viscosity but also of other macroscopic transport coefficients such as bulk viscosity and isothermal speed of sound [25,26]. To analyze the evolution of dissipation of velocity modes in time one can consider the decay of the initial velocity perturbations. The dissipation rate of such perturbations can be determined for the different length scales. For convenience we impose initial velocity perturbations as sinusoidal waves at low Reynolds number. We opt to initialize sinusoidal waves of the velocity field in two directions, transverse and longitudinal with respect to the initial velocity field. For transverse perturbations the initial velocity field is given by

$$\boldsymbol{v}_\perp = \boldsymbol{v_r} + v_{\max}(k_z)\rho^2 \sin(k_z z)\hat{\boldsymbol{e}_x}, \tag{14}$$

where $\boldsymbol{v_r}$ is a random velocity field, and $\hat{\boldsymbol{e}_x}$ is the unit vector in the x direction. To generate the random velocity field we run simulations with zero initial conditions for N_{prerun} time steps. $k_z = 2\pi n_z/L_z$ is the wave number of interest. For the case of longitudinal perturbations the initial velocity field is

$$\boldsymbol{v}_\parallel = \boldsymbol{v_r} + v_{\max}(k_x)\rho^2 \sin(k_x x)\hat{\boldsymbol{e}_x}. \tag{15}$$

As a solution for longitudinal and transverse perturbations we expect to have

$$\boldsymbol{v}_\perp = v_{\max}(k_z)\rho^2 \sin(k_z z) f_\perp(k_z,t) \tag{16}$$

and

$$\boldsymbol{v}_\parallel = v_{\max}(k_x)\rho^2 \sin(k_x x) f_\parallel(k_x,t), \tag{17}$$

respectively. At the standard hydrodynamic regime (in the limit of long time and large length scale) $f_\perp(k_z,t)$ and $f_\parallel(k_z,t)$ have analytical expressions, which assume exponential decay. As shown in Fig. 3, the exponential approximation of such functions can result in additional errors in the estimation of macroscopic parameters. We run DPD simulations with initial conditions defined by Eqs. (14) and (15) for integer wave numbers $n_x, n_z = 1,4,11,21$. Simulation input parameters are given in Table III. For each integer wave number we perform independent simulations $N_{\text{seed}} = 1000$ and ensemble average the transient velocity profiles. Subsequently, for each averaged velocity profile we determine the decay of sinusoidal waves by assessing the functions $f_\perp(k_x,t)$ and $f_\parallel(k_x,t)$. Results are shown in Fig. 2 and are discussed below.

B. Stationary fluctuations

Now we consider the dissipation of random fluctuations of the velocity field without adding a mean flow. A convenient

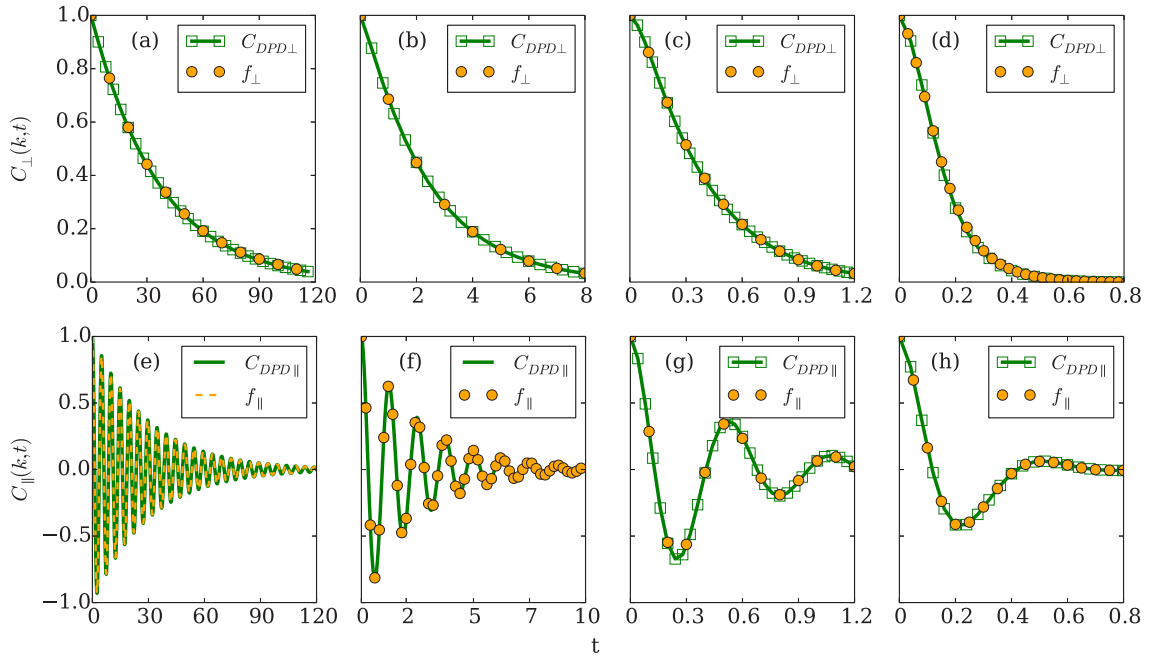

FIG. 2. Functions of decay of sinusoidal waves in parallel and perpendicular directions $f_\parallel$ and $f_\perp$ defined in Eqs. (16) and (17) compared with longitudinal $C_{\text{DPD}\parallel}$ and transverse $C_{\text{DPD}\perp}$ FTVACF measured in simulation. The comparison for different wave numbers is depicted from left to right as $n = 1,4,11,21$. We find a good agreement between the functions for different wave numbers.

way to derive the decay rate directly from the fluctuating velocity of the DPD solvent is to represent the random fluctuations of the particle velocity field as $\sum_{k_s} A_{k_s} f(k_s)$ where k_s is a length scale parameter. The dependence of macroscopic transport coefficients can be derived from the autocorrelation function of coefficients A_{k_s}. For zero mean flow, the common approach is to expand random fluctuations of the velocity field in space as Fourier series and to assess the dependency of macroscopic transport coefficients on the length scale from FTVACF. It is convenient to set

$$\hat{v}_l(k_m,t) = \sum_{j=1}^{N} v_{l,j}(m,t)\sin(m_j k_m). \tag{18}$$

For FTVACF $C(k_m,t)$ one can write

$$C(k_m,t) = \frac{\langle \hat{v}_l(k_m,t_0)\hat{v}_l(k_m,t_0+t)\rangle}{\delta \hat{v}_l^2(k_m,t)}. \tag{19}$$

Here $m = x,y,z$ and $l = x,y,z$ are direction indices and indicate the wave-number vector and velocity-vector components in the coordinate directions x,y,z, respectively. $m = l$ indicates longitudinal FTVACF with $C_\parallel(k,t)$, and $m \neq l$ indicates transverse FTVACF $C_\perp(k,t)$. $\delta \hat{v}_l^2(k_m,t)$ is the variance of the respective Fourier mode. It is possible to measure the functions $C_\perp(k,t)$ and $C_\parallel(k,t)$ from numerical simulations. We will denote FTVACF that are measured in simulations of a DPD solvent as $C_{\mathrm{DPD}\perp}(k,t)$ and $C_{\mathrm{DPD}\parallel}(k,t)$. To compare the functions $C_{\mathrm{DPD}\perp}(k,t)$ and $C_{\mathrm{DPD}\parallel}(k,t)$ with the decay of sinusoidal waves, we run DPD simulations with input parameters as given in Table III. After relaxation to stationary equilibrium, we transform the Lagrangian velocity distribution to a Eulerian field and then to Fourier space and measure FTVACF $C_{\mathrm{DPD}\perp}(k,t)$ and $C_{\mathrm{DPD}\parallel}(k,t)$. To minimize statistical error, we perform simulations with $N = 10^7$ time steps. Independent simulations are performed with different seeds $N_s = 32$ times to assess a statistical error. Figure 2 shows comparison of transverse $C_{\mathrm{DPD}\perp}(k,t)$ and longitudinal $C_{\mathrm{DPD}\parallel}(k,t)$ FTVACF exposed to the decay of an initial sinusoidal velocity field in transverse and longitudinal directions. FTVACF agrees with the decay of maximum velocities of sinusoidal waves from the previous subsection. There is neither numerical nor phenomenological difference between FTVACF and decay of sinusoidal waves. For convenience we choose to analyze longitudinal and transverse FTVACF in the remainder of the paper. In the following subsections we describe several methods of derivation of macroscopic transport coefficients from FTVACF. These methods will be compared in Sec. V.

C. Assumption of exponential decay

The behavior of a fluid on large scales can be described by the Navier-Stokes equations. An extension of the Navier-Stokes equations by a divergence of a random stress is able to capture many physical phenomena of thermal fluctuations on mesoscales such as multispecies mixing [27], diffusion enhancement and giant fluctuations [28,29], or the random walk of stationary shock [30]. Landau and Lifshitz first proposed this extension [31]. The velocity autocorrelation function is one of the main quantities to describe the statistical properties of the solvent. For the transverse and longitudinal FTVACF in case of LLNS we write [25]

$$C_{\mathrm{LLNS}\perp}(k,t) = e^{-k^2\frac{\eta_s}{\rho}t} \tag{20}$$

and

$$C_{\mathrm{LLNS}\parallel}(k,t) = e^{-k^2\Gamma t}\cos(\Theta k t) - \frac{k\Gamma}{\Theta}e^{-k^2\Gamma t}\sin(\Theta k t), \tag{21}$$

respectively, where

$$\Theta = \frac{\sqrt{4c_t^2 - k^2\Gamma^2}}{2}, \quad \Gamma = \left(1-\frac{1}{d}\right)\frac{\eta_s}{\rho} + \frac{1}{2}\frac{\eta_v}{\rho}, \tag{22}$$

and $d = 3$ is the number of dimensions. The DPD method is able to represent phenomena beyond the standard hydrodynamic limit and capture the mesoscopic hydrodynamics regime as well as N-particle Langevin dynamics [15,17]. To extend the analysis of collective properties of a DPD solvent to small scales we follow [17] and introduce the functions $\eta_s(k)$, $\eta_v(k)$, $c_t(k)$ instead of constant values of the macroscopic transport coefficients. The wave-number dependence in this case serves to describe the macroscopic properties of a DPD solvent on different wave numbers k. An accurate approximation of $C_{\mathrm{DPD}\parallel}(k,t)$ and $C_{\mathrm{DPD}\perp}(k,t)$ that are measured in the simulation allows us to estimate transport coefficients on different wave numbers k. To extend the functions $C_{\mathrm{LLNS}\perp}(k,t)$ and $C_{\mathrm{LLNS}\parallel}(k,t)$ to small scales one may consider wave-number dependent transport coefficients in Eqs. (20) and (21):

$$C_\perp(k,t) = e^{-k^2\frac{\eta_s(k)}{\rho}t} \tag{23}$$

and

$$C_\parallel(k,t) = e^{-k^2\Gamma(k)t}\cos[\Theta(k)kt] - \frac{k\Gamma(k)}{\Theta(k)}e^{-k^2\Gamma(k)t}\sin[\Theta(k)kt], \tag{24}$$

respectively, with

$$\Theta(k) = \frac{\sqrt{4c_t^2(k) - k^2\Gamma^2(k)}}{2}, \quad \Gamma(k) = \left(1-\frac{1}{d}\right)\frac{\eta_s(k)}{\rho} + \frac{1}{2}\frac{\eta_v(k)}{\rho}. \tag{25}$$

The FTVACF quantities $C_{\mathrm{DPD}\parallel}(k,t)$ and $C_{\mathrm{DPD}\perp}(k,t)$ that are measured from simulations can be approximated by Eqs. (23) and (24). From the result of the approximation one can derive the wave-number dependence of macroscopic transport coefficients $\eta_s(k)$, $\eta_v(k)$, $c_t(k)$. The results of the approximation for different wave numbers $n = 1,4,11,21$ are shown in Fig. 3. The results reveal that the approximation of FTVACF of a DPD solvent by the functions $C_\parallel(k,t)$ and $C_\perp(k,t)$ introduces approximation errors that affect the assessment of macroscopic transport coefficients. This error will be demonstrated and discussed in Sec. V.

D. Integral characteristics of FTVACF

Another approach to estimate shear viscosity is to integrate numerically FTVACF $C_{\mathrm{DPD}\perp}(k,t)$ in time. For transverse

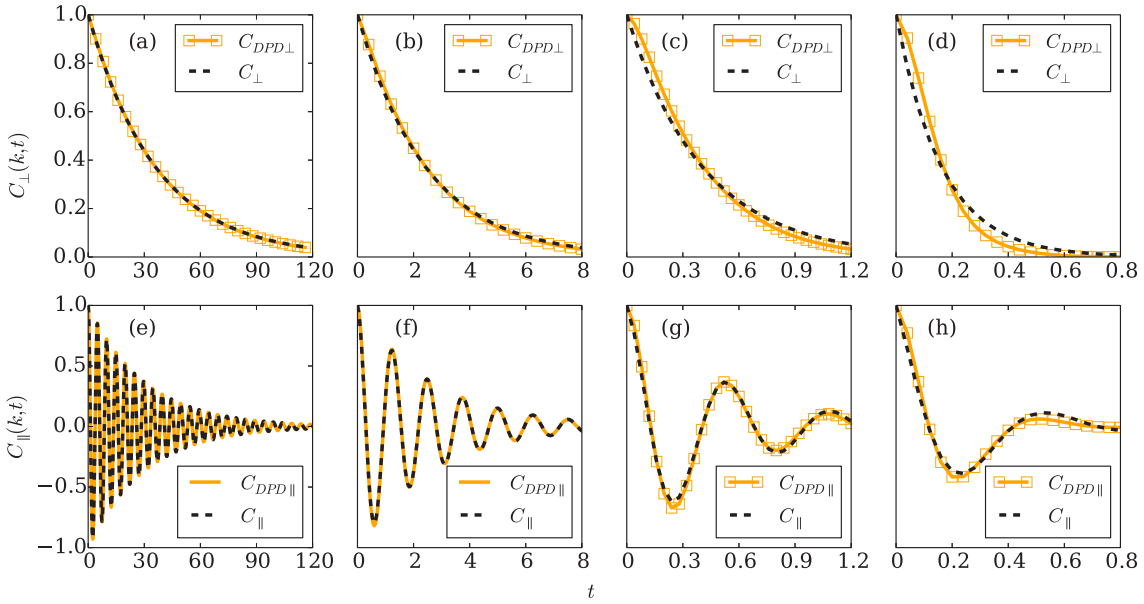

FIG. 3. FTVACF of DPD solvent $C_{\mathrm{DPD}\perp}$ and $C_{\mathrm{DPD}\parallel}$ which are measured from simulations compared with exponential approximations $C_\perp$ Eq. (23) and $C_\parallel$ Eq. (24). The comparison for different integer wave numbers is depicted (from left to right) as $n = 1,4,11,21$. We observe a deviation of the approximation functions and FTVACF of the DPD solvent for integer wave numbers $n \geqslant 11$.

FTVACF we write

$$\int_0^{t_1} C_{\mathrm{DPD}\perp}(k,t)dt = \int_0^{t_1} e^{-k^2\frac{\eta_s(k)}{\rho}t}dt \overset{t_1\to\infty}{=} \frac{\rho}{\eta_s(k)k^2}, \tag{26}$$

where t_1 is the maximum time difference for which we measure transverse and longitudinal FTVACF. The wave-number dependence of the shear viscosity $\eta_s(k)$ is given by

$$\eta_s(k) = \frac{\rho}{k^2}\left(\int_0^{t_1} C_{\mathrm{DPD}\perp}dt\right)^{-1}. \tag{27}$$

The longitudinal FTVACF depends on two transport coefficients and both isothermal speed of sound and bulk viscosity cannot be directly derived from integration of longitudinal FTVACF. A disadvantage of the method is related to finite time t_1. FTVACF is measured in the following way: during the simulation at every time step δt we measure the correlation between the instantaneous velocity $v(k,t_0+\delta t)$ in Fourier space and stored ones from the previous velocity field that consists of $N_v = t_1/\delta t$ elements. δt is a time step of FTVACF that could in principle be larger than the time step of the DPD computation dt. Computational cost of measuring modes of FTVACF directly relates to N_v. To minimize errors in the numerical evaluation of the integral (26) it is important to keep t_1 as large as possible. One way to decrease t_1 is to approximate $C_{\mathrm{DPD}\perp}(k,t)$ by some suitable function $g_\perp(k,t)$ and then compute the integral (26) for $t_1 = \infty$. Section IV F describes suitable choices for the function $g_\perp(k,t)$ in detail.

E. Fourier transform of the density autocorrelation functions

Equations (23) and (24) are derived from isothermal linearized LLNS equations which have macroscopic nature. Characteristics of DPD solvent $C_{\mathrm{DPD}\perp}(k,t)$ and $C_{\mathrm{DPD}\parallel}(k,t)$ might differ from Eqs. (23), (24), and (30) due to microscopic properties of a DPD solvent as well as truncation errors. For the shear mode one can compare the prediction of shear viscosity derived from $C_{\mathrm{DPD}\perp}(k,t)$ with the prediction derived from Kolmogorov flow. To estimate the accuracy of bulk viscosity and isothermal speed of sound derived from longitudinal FTVACF $C_{\mathrm{DPD}\parallel}(k,t)$ we consider Fourier transform of the density autocorrelation function (FTDACF). Unlike other particle methods such as SPH and SDPD the the DPD method does not model density field explicitly. Each particle of the DPD solvent has constant mass. The mass density of the DPD solvent can be introduced through the kernel approximation at every point of the DPD solvent. For simplicity we assume that the mass density is unity at the locations of DPD particles and introduce FTDACF similarly as FTVACF:

$$\hat{\rho}(k_m,t) = \sum_{j=1}^{N} \rho_j \sin(m_j k_m), \tag{28}$$

where $\rho_j = 4$ is a mass density of a DPD particle with index j. For FTDACF we write

$$C_{\mathrm{DPD}\rho}(k_m,t) = \frac{\langle\hat{\rho}(k_m,t_0)\hat{\rho}(k_m,t_0+t)\rangle}{\delta\hat{\rho}^2(k_m,t)}. \tag{29}$$

As mass density is a scalar we have only a single FTDACF component. Similarly to Eq. (24) we write

$$C_\rho(k,t) = e^{-k^2\Gamma(k)t}\cos[\Theta(k)kt] + \frac{k\Gamma(k)}{\Theta(k)}e^{-k^2\Gamma(k)t}\sin[\Theta(k)kt]. \tag{30}$$

In the following section we introduce the function $g_\parallel$ that may improve accuracy of prediction of bulk viscosity and isothermal speed of sound.

F. Nonexponential approximation of FTVACF modes

Figure 3 demonstrates that transverse and longitudinal FTVACF exhibit nonexponential behavior on small scales. Note that it has been established that the deviation from exponential decay on small scales is physically sound [14,19,20,32–35]. Such a deviation may be approximated by the introduction of a memory function. Consider the time correlation function $C(t)$. Its memory function can be defined as

$$\frac{\partial}{\partial t}C(t) = -\int_0^t dt'\phi(t')C(t-t'). \tag{31}$$

On the large time scales where fluid dynamics is described by the Navier-Stokes equations, the memory function coincides with the Dirac delta function. On small scales the memory function is usually approximated by some phenomenological model. Given such a model one can derive a closed approximation for FTVACF modes. We suggest another approach: instead of introducing a memory function one can introduce functions to approximate the FTVACF modes. To derive macroscopic transport coefficients of the DPD solvent from measured FTVACF $C_{\mathrm{DPD}\perp}(k,t)$ and $C_{\mathrm{DPD}\parallel}(k,t)$, we modify the exponential functions $C_\perp(k,t)$ and $C_\parallel(k,t)$. The functions are modified by introducing a parameter that allows us to further reduce the approximation error. The approximation function of transverse FTVACF is $g(k,t)_\perp$ and is defined as

$$g(k,t)_\perp = e^{-k^2 A_k \frac{t^2}{t+B_k}}. \tag{32}$$

The parameters $A_k > 0$ and $B_k > 0$ depend on k and are calibrated to predict FTVACF. A_k has the dimension of kinematic viscosity and B_k has the dimension of time. To derive the shear viscosity one can compute the integral of the function (32):

$$\eta_s(k) = \frac{\rho}{k^2}\left(\int_0^\infty e^{-k^2 A_k \frac{t^2}{t+B_k}}\, dt\right)^{-1}. \tag{33}$$

It is important to emphasize that with $t \gg B_k$ the function $g(k,t)_\perp$ corresponds to the exponential function $C_\perp(k,t)$, and $\eta_s(k) = \rho A_k$. When t and B_k have the same order one can represent the integral of the function $g(k,t)_\perp$ as

$$\int_0^\infty g(k,t)_\perp dt = B_k e^{2k^2 A_k/B_k} K_{-1}\left(\frac{k^2 A_k}{B_k}, \frac{k^2 A_k}{B_k}\right), \tag{34}$$

where $K_{-1}(\frac{A_k}{B_k}, \frac{A_k}{B_k}) = \int_1^\infty e^{-\frac{A_k}{B_k}(t+\frac{1}{t})}\, dt$ is an incomplete Bessel function. In this work we evaluate the integral $\int_0^\infty g(k,t)_\perp dt$ numerically. To fit longitudinal FTVACF and FTDACF we write

$$g(k,t)_\parallel = e^{-k^2 C_k \frac{t^2}{t+D_k}}\left[\cos(\Theta_k kt) - \frac{kC_k}{\Theta_k}\sin(\Theta_k kt)\right], \tag{35}$$

$$g(k,t)_\rho = e^{-k^2 C_k \frac{t^2}{t+D_k}}\left[\cos(\Theta_k kt) + \frac{kC_k}{\Theta_k}\sin(\Theta_k kt)\right]. \tag{36}$$

For sufficiently large time differences $t \gg D_k$ Eq. (35) reduces to Eq. (21). The isothermal speed of sound $c_t(k)$ and the coefficients C_k and D_k may be derived directly from the approximation with function $g_\parallel(k,t)$ of the longitudinal FTVACF $C_{\mathrm{DPD}\parallel}(k,t)$ that is measured from the computational experiment. The parameter C_k has the dimension of sound attenuation and D_k has the dimension of time. For sound attenuation

$$\Gamma(k) = \frac{1}{k^2}\left(\int_0^\infty e^{-k^2 C_k \frac{t^2}{t+D_k}} dt\right)^{-1}. \tag{37}$$

The bulk viscosity relates to sound attenuation in three dimensions as

$$\eta_v(k) = 2\rho\Gamma(k) - \tfrac{4}{3}\eta_s(k). \tag{38}$$

Figure 4 shows the approximation of transverse and longitudinal FTVACF with the functions $g(k,t)_\perp$ and $g(k,t)_\parallel$. $g(k,t)_\perp$ gives a good approximation to the nonexponential decay of $C(k,t)_{\mathrm{DPD}\perp}$. The longitudinal approximation $g(k,t)_\parallel$ slightly differs from $C(k,t)_{\mathrm{DPD}\parallel}$ for large wave numbers. However, it improves the results in comparison to the exponential approximation $C(k,t)_\parallel$. A similar result, however not demonstrated here, was observed for approximation of $C(k,t)_{\mathrm{DPD}\rho}$.

V. PREDICTIVE CAPABILITY OF NONEXPONENTIAL APPROXIMATIONS

In this section we compare the predictive capability of nonexponential approximations of macroscopic transport coefficients with exponential approximations in terms of the wave-number dependence of $\eta_s(k)$, $\eta_v(k)$, and $c_t(k)$. Specifically, we compare four different measures and approximations of $\eta_s(k)$: (1) exact evaluation of Kolmogorov flow described in Sec. III; (2) approximation of FTVACF $C_{\mathrm{DPD}\perp}(k,t)$ with exponential function $C_\perp(k,t)$ from Sec. IV C; (3) integration of $C_{\mathrm{DPD}\perp}(k,t)$ described in Sec. IV D; and (4) nonexponential approximation of $C_{\mathrm{DPD}\perp}(k,t)$ described in Sec. IV F.

We perform three-dimensional simulations using the input parameters given in Table III and assess the dependence of the shear viscosity on wave number. The results are shown in Fig. 5. Simulation lengths are chosen such as to achieve a statistical error in the estimation of shear viscosity of less than 1%. As reference $\eta_s(k)$ we consider the shear viscosity that has been derived from the analysis of Kolmogorov flow. The estimation error is computed as

$$E|_{\eta_s}(k) = 100\frac{\eta_s(k) - \eta_s|_{KF\perp}(k)}{\frac{1}{N_k}\sum_k \eta_s|_{KF\perp}(k)}, \tag{39}$$

where $\eta_s(k)$ is the shear viscosity given by one of the approximations above, and $\eta_s|_{KF\perp}(k)$ is the reference shear viscosity. We observe that the shear viscosity derived from the exponential approximation $C_\perp$ deviates from the reference. This deviation originates from the fact that the transverse FTVACF of a DPD solvent is nonexponential as shown in Fig. 3. The estimation of $\eta_s(k)$ directly from an integration of $C_{\mathrm{DPD}\perp}(k,t)$ agrees with the reference for large wave numbers and should be exact as $t_1 \to \infty$. However, due to finite time t_1 the numerical value is slightly smaller. In the simulation we choose the same $t_1 = \text{const.}$ for all wave numbers. For small wave numbers t_1 should be larger than the current value which leads to an overestimation according to Eq. (27). However, this overestimation does not invalidate our general observation. When the shear viscosity is estimated from the nonexponential approximation of FTVACF using Eq. (32) we obtain a much better agreement with the exact value. From an analysis of the longitudinal FTVACF one can assess

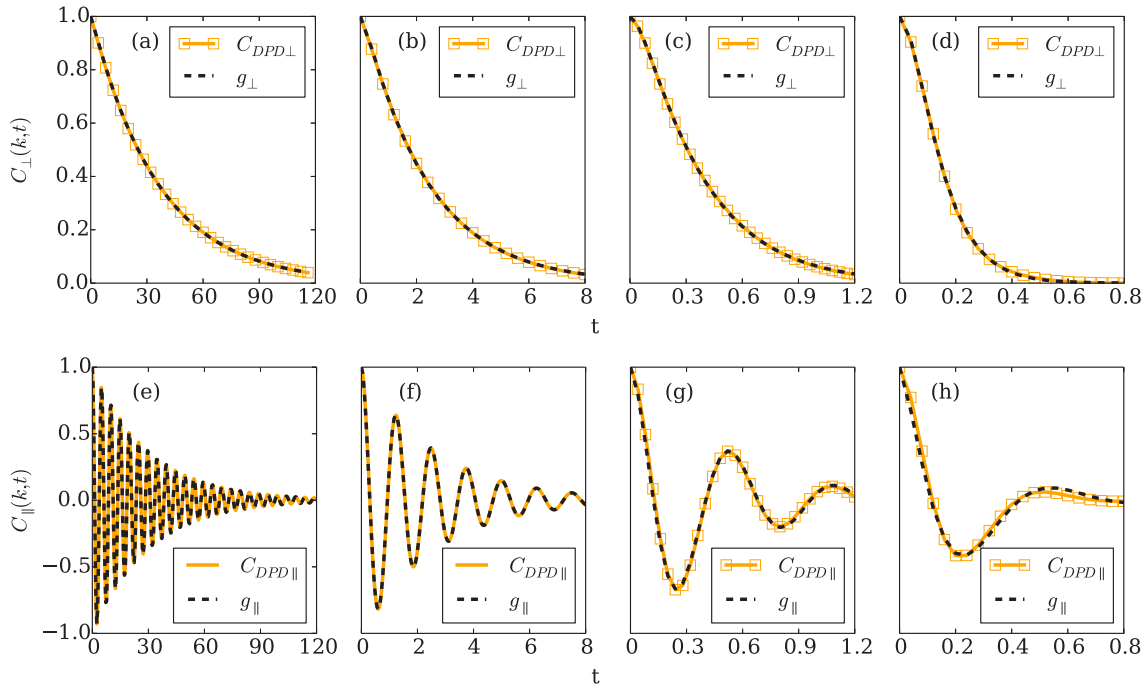

FIG. 4. FTVACF of DPD solvent $C_{\mathrm{DPD}\perp}$ and $C_{\mathrm{DPD}\parallel}$ which are measured in simulation compared with nonexponential approximations $g_\perp$ Eq. (32) and $g_\parallel$ Eq. (35). The comparison for different wave numbers is shown as $n = 1,4,11,21$ (from left to right).

the dependence on wave number of macroscopic transport coefficients such as the bulk viscosity $\eta_v(k)$ and the isothermal speed of sound $c_t(k)$. Aside from analytical estimations of such dependencies for the case of noninteracting DPD particles ($a_{ij} = 0$) in [17], no methods have been reported in literature so far for an estimation of $\eta_v(k)$ and $c_t(k)$ of a DPD solvent. For such purposes one can analyze the decay of sinusoidal longitudinal waves, which agrees, as has been shown in Fig. 2, with longitudinal FTVACF $C_{\mathrm{DPD}\parallel}(k,t)$ for low Reynolds numbers in the linear regime. In order to estimate the accuracy of estimates for $\eta_v(k)$ we compare four different methods that are based on the estimation of the bulk viscosity from longitudinal FTVACF $C_{\mathrm{DPD}\parallel}(k,t)$ and FTDACF $C_{\mathrm{DPD}\rho}(k,t)$: (1) approximation of FTVACF $C_{\mathrm{DPD}\parallel}(k,t)$ with exponential function $C_\parallel(k,t)$ from Sec. IV C; (2) nonexponential approximation of $C_{\mathrm{DPD}\parallel}(k,t)$ described in Sec. IV F; (3) approximation of FTDACF $C_{\mathrm{DPD}\rho}(k,t)$ with exponential function $C_\rho(k,t)$ from Sec. IV C; and (4) nonexponential approximation of $C_{\mathrm{DPD}\rho}(k,t)$ with function $g_\rho(k,t)$ described in Sec. IV F.

For assessment of $c_t(k)$ we consider four similar possibilities of using exponential and nonexponential approximations for $C_{\mathrm{DPD}\parallel}(k,t)$ and $C_{\mathrm{DPD}\rho}(k,t)$. Figure 6 shows the dependence of the bulk viscosity and the isothermal speed of sound on wave number that was estimated with the different methods. The statistical errors on both plots are smaller than the symbol size. Differences between approximations are quantified according to

$$D|_{c_t}(k) = c_t(k) - c_t|_{g\parallel}(k) \tag{40}$$

and

$$D|_{\eta_v}(k) = \eta_v(k) - \eta_v|_{g\parallel}(k). \tag{41}$$

For the assessment of the relative differences $D|_{c_t}(k)$ and $D|_{\eta_v}(k)$ in the approximations of $c_t(k)$ and $\eta_v(k)$ with the different methods we take the estimation derived from the nonexponential approximation of the longitudinal mode of FTVACF as reference. For the approximating error in the isothermal speed of sound, exponential $c_t(k)|_\parallel$ and nonexponential approximation $c_t(k)|_{g\parallel}$ from both FTVACF and FTDACF give similar results at small wave numbers. For large wave numbers the difference $D|_{c_t}$, the difference between estimation of $c_t(k)$ from FTVACF and FTDACF, is smaller for approximation with the nonexponential function. Moreover, in Fig. 4 we show that the nonexponential function $g(k,t)_\parallel$ improves the approximation of longitudinal FTVACF $C_{\mathrm{DPD}\parallel}(k,t)$ in comparison with the exponential function $C_\parallel$. For these reasons we consider results derived from the nonexponential approximation as more accurate for estimating $c_t(k)$.

The shear viscosity $\eta_s(k)$ and the isothermal speed of sound $c_t(k)$ are estimated directly from the transverse and the longitudinal FTVACF. However, to estimate the bulk viscosity from $C_{\mathrm{DPD}\parallel}(k,t)$ that is measured in simulations, one first needs to determine shear viscosity and isothermal speed of sound. Figure 6 shows the dependence of bulk viscosity, that is estimated with four different methods, on the wave number. We observe significant discrepancy between estimation of bulk viscosity from FTVACF and FTDACF. For the smallest wave number, difference is about 9% and it rises with larger wave numbers. The discrepancy is due to imperfections of the fitting function that is not able to incorporate the microscopic properties of the DPD solvent in the longitudinal direction. The improvement of the accuracy for the bulk viscosity prediction is a subject of future work. For both estimates the statistical error is smaller than the symbol size, quantitatively less than 1%. We show that the nonexponential approximations $g(k,t)_\perp$

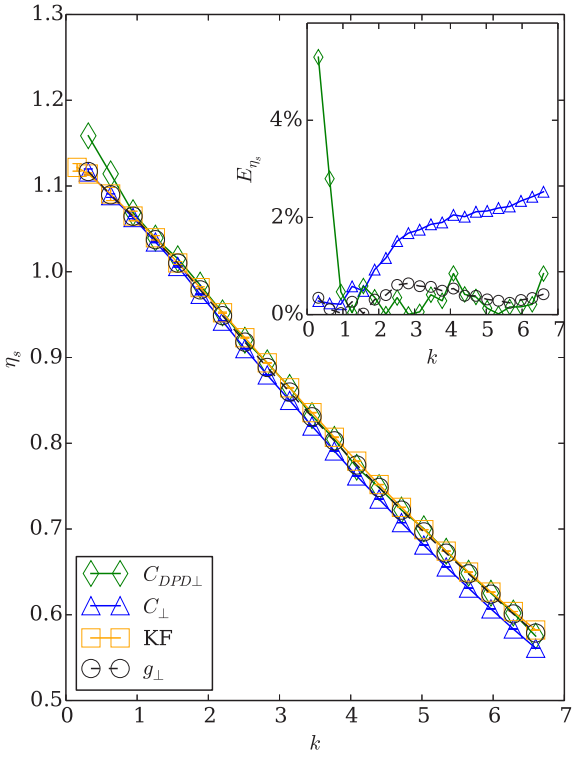

FIG. 5. Dependence of shear viscosity on wave number that is estimated with different methods. The exponential fit $C_\perp$ (blue lines with triangles) implies significant errors compared with the reference for Kolmogorov flow (orange line with squares) for large wave numbers. The large deviation at small wave numbers of the estimation that is derived by numerical integration of transverse FTVACF (green line with diamonds) can be explained by the limited time of measurement t_1. The black line with circles denotes the estimation from the exponential fit with function $g_\perp$. The error E_{η_s} is measured according to Eq. (39).

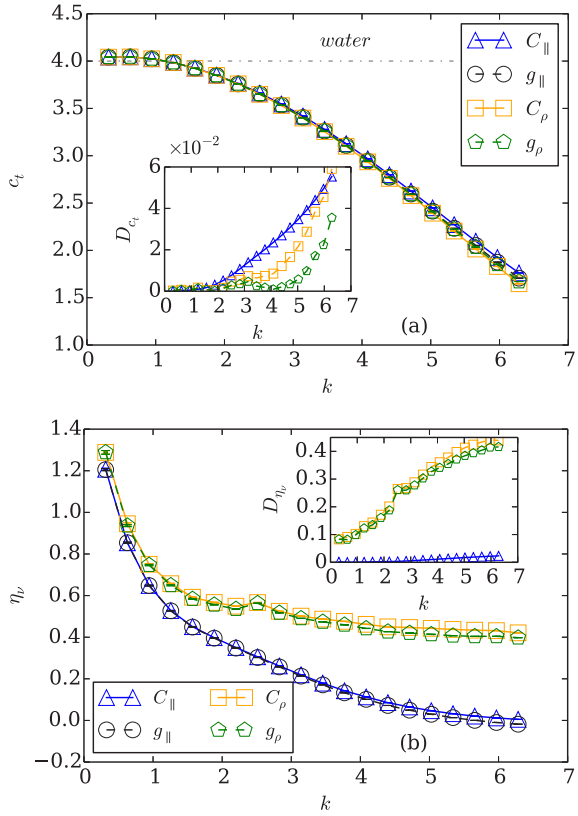

FIG. 6. Dependence of isothermal speed of sound and bulk viscosity on wave number, estimated with different methods. Differences between estimates D_{η_v} and D_{c_t} are computed from Eqs. (40) and (41).

and $g(k,t)_\parallel$ allow us to derive the wave-number dependence of macroscopic transport coefficients $c_t(k)$, $\eta_s(k)$, and $\eta_v(k)$. We also show that these predictions are more accurate than those derived from exponential approximations. Up to this point our attention was restricted to a single set of DPD input parameters. The following section is devoted to an extension of the approach to a wider range of DPD input parameters.

VI. NUMERICAL EXPERIMENTS

In this section we analyze the approximation capability of FTVACF with nonexponential functions $g_\perp(k,t)$ and $g_\parallel(k,t)$ for different sets of nondimensional DPD input parameters. We also estimate bulk viscosity and isothermal speed of sound for different Ω_0 (see Table I). To facilitate computations we shorten the domain size to $[L_x,L_y,L_z]=[10,10,10]$. We set the number density as $\rho=4$, temperature as $k_BT=1$, cutoff radius as $r_c=1$, and $\gamma=\frac{\sigma^2}{2k_BT}$. The number of time steps in the stationary regime is $N_t=4\times10^6$. For each set of input parameters we perform $N_{\text{seed}}=16$ independent simulations. The DPD input parameter k_BT is related to the nondimensional parameter Ω_0. For the kernel (9) the relation is

$$k_BT=\left(\frac{\pi m^{3/2}\rho r_c^4\sigma^2}{45\Omega_0}\right)^{\frac{2}{3}}. \tag{42}$$

A detailed derivation is provided in the Appendix. For the DPD input parameters of the previous section we have $\Omega_0=2.5$. In this section we take $\Omega_0=[0.1;0.3;1;5;10;20;50;100]$ with the corresponding k_BT. We choose a time-step size according to the relation $dt=0.01\sqrt{\frac{mr_c^2}{k_BT}}$ as in [36] for all cases except for $\Omega_0=[50;100]$ where $dt=0.01$. We vary the repulsive parameter of the DPD solvent $a_{ij}=[0;18.75k_BT]$. The particular choices of the repulsive potential are motivated by the fact that $a_{ij}=18.75k_BT$ is widely used for modeling water [2] and that for $a_{ij}=0$ analytical predictions of macroscopic transport coefficients in the classical hydrodynamics regime are possible [17].

A. Approximation error analysis

For each simulation we estimate the dependency $\eta_s(k)$ by three different methods: (i) from direct integration of $C_{\text{DPD}\perp}(k,t)$, (ii) by approximating $C_{\text{DPD}\perp}(k,t)$ with an exponential function $C_\perp(k,t)$, and (iii) by a nonexponential function $g_\perp(k,t)$. We take t_1 sufficiently large in order to obtain an accurate prediction of the shear viscosity dependence upon integration of $C_{\text{DPD}\perp}(k,t)$. We consider the shear viscosity obtained by integration of $C_{\text{DPD}\perp}(k,t)$ as reference. We

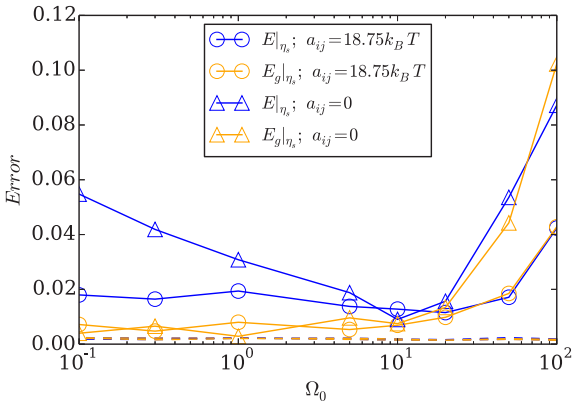

FIG. 7. Approximation errors (43) and (44) derived from different shear viscosity estimates for different values of Ω_0. As reference we integrate the transverse FTVACF measured in the simulation. Statistical errors are indicated with dashed lines.

estimate approximation errors for exponential and nonexponential approximations as

$$E|_{\eta_s} = \frac{\left[\sum_{k=2\pi/L}^{2\pi/r_c} \frac{r_c}{L}(\eta_s|_{\perp}(k) - \eta_s|_{\mathrm{DPD}\perp}(k))^2\right]^{\frac{1}{2}}}{\sum_{k=2\pi/L}^{2\pi/r_c} \eta_s|_{\mathrm{DPD}\perp}(k)} \tag{43}$$

and

$$E_g|_{\eta_s} = \frac{\left[\sum_{k=2\pi/L}^{2\pi/r_c} \frac{r_c}{L}(\eta_s|_{g\perp}(k) - \eta_s|_{\mathrm{DPD}\perp}(k))^2\right]^{\frac{1}{2}}}{\sum_{k=2\pi/L}^{2\pi/r_c} \eta_s|_{\mathrm{DPD}\perp}(k)}, \tag{44}$$

respectively. Figure 7 shows differences in the estimation of $\eta_s(k)$ by exponential and nonexponential functions. It demonstrates that for $\Omega_0 \leqslant 10$ the nonexponential function gives a better prediction than the exponential function. For $\Omega_0 \geqslant 10$ the prediction of $\eta_s(k)$ has a similar error. Large errors in the estimations of shear viscosity for the case $\Omega_0 \geqslant 20$ relate to the different shape of FTVACF for large Ω_0; consider the transverse FTVACF for the case of $\Omega_0 = 100$ shown in Fig. 8. As was mentioned in the previous section, no method to determine DPD solvent bulk viscosity and isothermal speed of sound except for that from FTVACF and FTDACF can be found in current literature. One can analyze the decay of sinusoidal waves for such purposes. However, this will result in the same $C_{\mathrm{DPD}\parallel}$ and it does not resolve the main issue of how to estimate $c_t(k)$ and $\eta_v(k)$ from longitudinal FTVACF and FTDACF. For that reason we do not estimate the approximation error for the isothermal speed of sound and bulk viscosity.

B. Simulation results

On the small scales of the DPD solvent shear and bulk viscosities are lower. With decreasing k the magnitudes of $\eta_s(k)$ and $\eta_v(k)$ increase until a certain plateau is reached. For the plateau, the dynamics of DPD particles can be described by classical hydrodynamics. To estimate the classical hydrodynamic level of viscosities it has been proposed to use the following expressions [15]:

$$\eta_s = \frac{\gamma\rho^2[\boldsymbol{r}w_d]_{\boldsymbol{r}}}{2d(d+2)} + \frac{dmk_BT}{2\gamma[\boldsymbol{r}w_d]_{\boldsymbol{r}}}, \tag{45}$$

and

$$\eta_v = \frac{\gamma\rho^2[\boldsymbol{r}w_d]_{\boldsymbol{r}}}{2d^2} + \frac{mk_BT}{\gamma[\boldsymbol{r}w_d]_{\boldsymbol{r}}}. \tag{46}$$

For nondimensional kinematic shear and bulk viscosity these expressions correspond to

$$\tilde{\nu} = \tfrac{1}{2} + a_2\Omega_0^2 \tag{47}$$

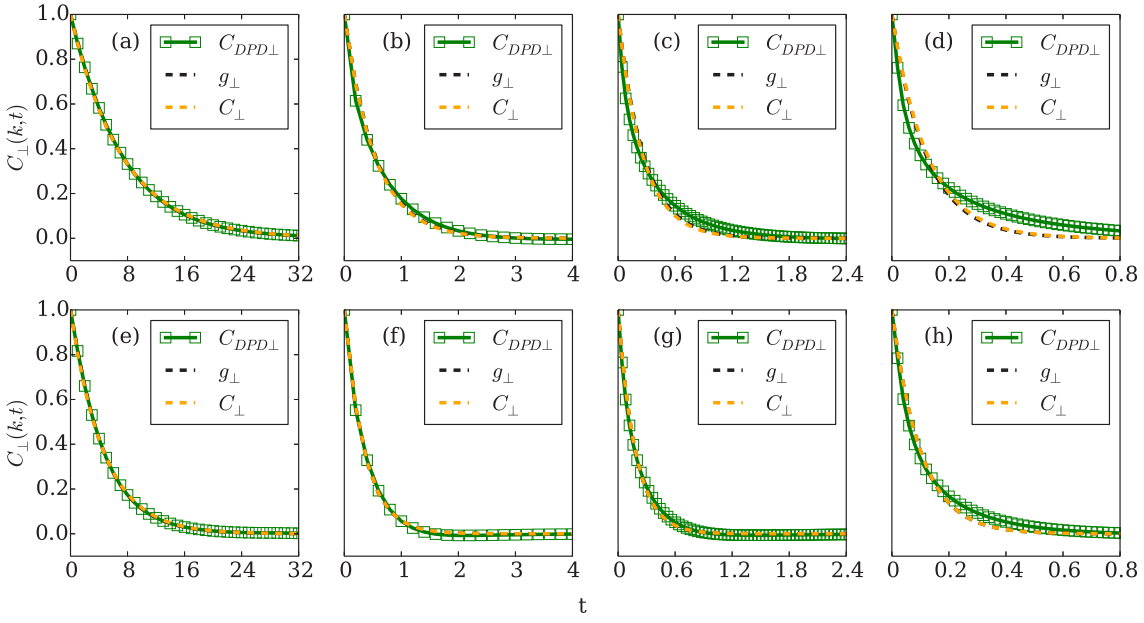

FIG. 8. Transverse FTVACF for $\Omega_0 = 100$ compared with exponential and nonexponential approximations for different wave numbers (from left to right) $n = 1,4,6,10$. Two cases considered: $a_{ij} = 0$ (top) and $a_{ij} = 18.75k_BT$ (bottom).

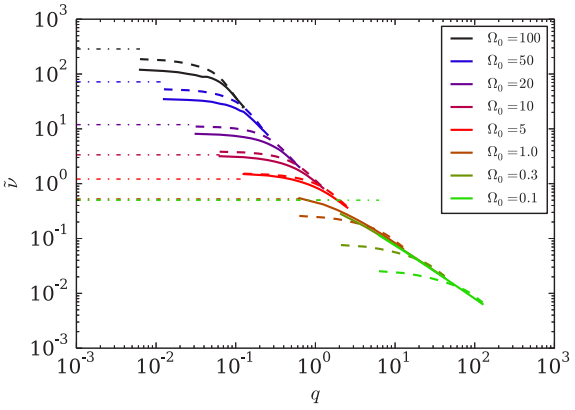

FIG. 9. Nondimensional kinematic shear viscosity $\tilde{\nu}$ dependence on nondimensional wave number $q = kl_0$ for different Ω_0 and different a_{ij}. Solid lines correspond to the case of $a_{ij} = 0$ and dashed lines correspond to $a_{ij} = 18.75k_BT$. Dash-dotted lines are estimations of the shear viscosity from Eq. (47) for the plateau values.

and

$$\tilde{\zeta} = \tfrac{1}{2} + \tfrac{1}{2}b_2\Omega_0^2, \tag{48}$$

respectively, where the coefficients a_2 and b_2 with kernel (9) are

$$b_2 = 3a_2 = \frac{3[\boldsymbol{r}w_D]_{\boldsymbol{r}}}{2(d+2)r_c^2[w_D]_{\boldsymbol{r}}} = \frac{3}{35}. \tag{49}$$

Figure 9 illustrates the dependence of the nondimensional kinematic shear viscosity on nondimensional wave number q. We compare simulations with $a_{ij} = 0$ and $18.75k_BT$ with the estimation of the kinematic shear viscosity from Eq. (47). The estimation (47) was derived for the case of $a_{ij} = 0$. We find that Eq. (47) may not give a good prediction for the plateau level of the kinematic shear viscosity even for the case without repulsive potential. For $\Omega_0 \geqslant 10$ Eq. (47) overestimates the shear viscosity measured from the simulation. For $10 > \Omega_0 \geqslant 1$ Eq. (47) underestimates shear viscosity measured from the simulation. For $\Omega_0 < 1$ the shear viscosity is far from the classical hydrodynamic limit due to the limitations in domain size, so that no definite conclusions can be drawn on the prediction (47) for the case of $a_{ij} = 0$. The kinematic shear viscosity measured from the simulation for the case of $a_{ij} = 18.75k_BT$ differs from that for $a_{ij} = 0$. For $\Omega_0 < 5$ the DPD solvent with repulsive potential has lower shear viscosity in comparison with the case without repulsive potential. For $\Omega_0 > 5$ the repulsive potential enhances shear viscosity.

Figure 10 shows the dependence of the nondimensional isothermal speed of sound on nondimensional wave number q. Two different values for the repulsive potential are considered, and two different estimation methods were used. For the case of zero repulsive potential and small Ω_0 the isothermal speed of sound remains constant. With increasing Ω_0 one can observe a deviation of $\tilde{c}_t(k)$ from the constant value. For the case of nonzero repulsive potential the estimation of the isothermal speed of sound with two different methods is similar for $\Omega_0 < 50$. The estimated isothermal speed of sound corresponds to the speed of sound in water $\tilde{c}_t = 4$ [2]. The small difference in the largest wave numbers between two methods may be due

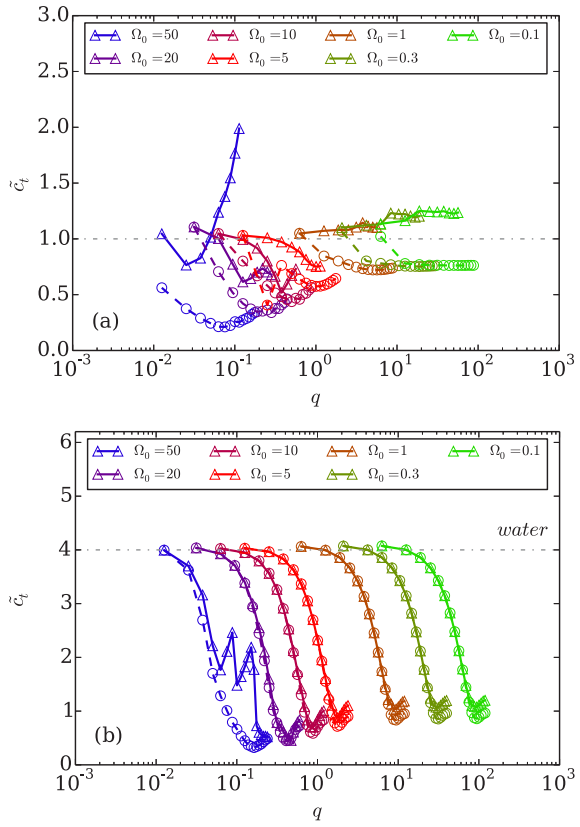

FIG. 10. Nondimensional isothermal speed of sound $\tilde{c}_t$ dependence on nondimensional wave numbers $q = kl_0$ for different Ω_0 and different $a_{ij} = 0$ (upper plot) and $a_{ij} = 18.75$ (lower plot). Solid lines with circles correspond to the measurements derived from analysis of longitudinal FTVACF and dashed lines with triangles correspond to measurements from FTDACF. The dash-dotted line is the nondimensional speed of sound in water on the lower plot [2] and analytical estimation for the case of zero repulsive potential $\tilde{c}_t = 1$ on the upper plot.

to truncation errors. The estimation of the isothermal speed of sound from longitudinal FTVACF and FTDACF differs for the case $a_{ij} = 0$ and is similar only for the largest wave number when $\Omega_0 \leqslant 20$. This may be related to the approximation error of FTVACF in the case of $a_{ij} = 0$. An approximation error was also found for large Ω_0. A further improvement of the estimation accuracy of $\tilde{c}_t(k)$ for the case of large Ω_0 as well as small a_{ij} is subject of future work.

In contrast to the estimation of the isothermal speed of sound we find that the kinematic bulk viscosity measured from simulations with different methods results in significant discrepancies for the case of both nonzero and zero repulsive potential on small scales and cannot be considered as accurate. For large scales the discrepancy between the two methods is smaller. We found a better agreement of the kinematic bulk viscosity with its estimation from Eq. (48) for large scales in comparison with measurements and predictions for kinematic shear viscosity. The results are given in Fig.11. Moreover, on large scales no differences in the bulk viscosity for $a_{ij} = 0$ and 18.75 was found for $\Omega_0 > 5$. When $\Omega_0 < 5$ we find that the bulk viscosity does not approach a plateau on the smallest

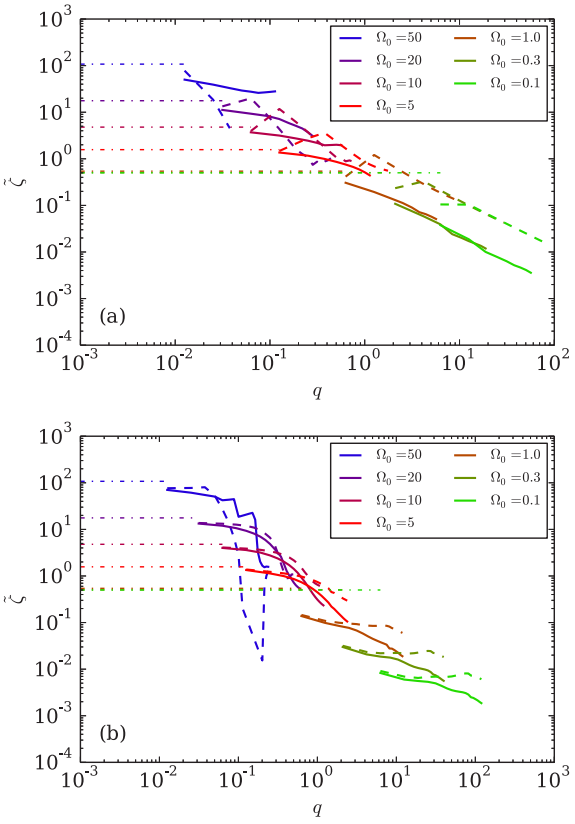

FIG. 11. Nondimensional kinematic bulk viscosity $\tilde{\eta}_v$ dependence on nondimensional wave number $q = kl_0$ for different Ω_0 and different $a_{ij} = 0$ (upper plot) and $a_{ij} = 18.75$ (lower plot). The legend is the same as that of Fig. 9. Dash-dotted lines are estimations of the shear viscosity from Eq. (48) for the plateau values. The solid line is the estimation from longitudinal FTVACF. The dashed line is the estimation from FTDACF.

measured wave number $k = \frac{2\pi}{L}$ and thus cannot be compared with the prediction.

VII. SUMMARY AND DISCUSSION

We start our analysis of a DPD solvent with the derivation of the dependence of the stationary shear viscosity on wave number with dynamic overlapping coefficient $\Omega_0 = 2.5$. For this purpose we use the Kolmogorov flow. Subsequently, we consider the decay of sinusoidal waves to estimate dynamic properties of shear viscosity. We show that the decay of sinusoidal waves for the case of parallel and perpendicular directions corresponds to longitudinal and transverse FTVACF. The dynamic overlapping is a nondimensional parameter that defines the dynamic regime of the DPD solvent [17]. For $\Omega_0 = 2.5$, the DPD solvent corresponds to the case considered in [10]. For the case of $\Omega_0 = 2.5$ we demonstrate the nonexponential character of transverse and longitudinal FTVACF. The estimation of stationary shear viscosity from the exponential approximation shows a significant deviation from the stationary shear viscosity, derived from an analysis of Kolmogorov flow. To fit both longitudinal and transverse FTVACF we propose nonexponential functions $g_\perp(k,t)$ and $g_\parallel(k,t)$, which recover exponential functions for small parameters B_k and D_k. We show that the shear viscosity which is estimated from an approximation of FTVACF modes with nonexponential functions agrees with the stationary shear viscosity computed for Kolmogorov flow. We use the same method to derive the dependence of other macroscopic transport coefficients, such as bulk viscosity and isothermal speed of sound, on wave number.

In order to assess the applicability limits of the approach, we perform simulations with different DPD input parameters. We show that the method of derivation of the shear viscosity from a nonexponential fit of FTVACF is suitable for a wide range of input parameters $\Omega_0 < 20$. The proposed method is more accurate than the derivation of macroscopic transport coefficients from exponential functions for $\Omega_0 \leqslant 10$ and gives the same approximation errors for $\Omega_0 > 10$. We assess the accuracy of the prediction of shear viscosity in the classical hydrodynamic limit Eqs. (47) and (48) that was proposed in [15] which matches neither the case of the DPD solvent without repulsive potential nor that with repulsive potential $a_{ij} = 18.75 k_B T$. In contrast, the prediction of the classical hydrodynamics limit of the bulk viscosity shows better agreement with the bulk viscosity measured from the simulation on the largest scale. The nondimensional isothermal speed of sound for the DPD solvent with repulsive potential is similar to that for waterlike fluid on large scales. In the case of zero repulsive potential the isothermal speed of sound corresponds to unity, the value that was derived from analysis [17].

The analyses described in the paper allow us to asses macroscopic transport properties on different scales. The estimation can help in coupling the DPD solvent with other mesoscale methods such as LLNS or SDPD. Moreover, for the case of $\Omega_0 < 20$ the analysis is accurate for shear viscosity on the small scale and may be useful to couple the DPD solvent with molecular dynamics. One may also assess the accuracy of the DPD solvent in representing phenomena beyond the standard hydrodynamic limit. Modes of FTVACF can be measured in the experiment and compared with the simulation of the DPD solvent and with simulations of molecular dynamics.

Introducing $g_\perp(k,t)$ and $g_\parallel(k,t)$ can be interpreted as an attempt to construct a surrogate model for the memory function of a DPD solvent. The analytical derivation of the exact memory function is tedious and not necessarily possible. However, an accurate approximation by a model of the memory function of the solvent allows us to predict the k dependence of the solvent *a priori*. For that purpose, it can be useful to consider the dependence of the fitting parameters A_k, B_k, C_k, D_k on different scale ranges, which may allow us to derive an empirical dependence of macroscopic transport coefficients of a DPD solvent on wave number from Eqs. (33) and (34).

We have considered so far only the classical DPD solvent. However, we believe that the analysis can be readily extended to measure the k dependence of macroscopic parameters for other variants of the DPD solvent, such as multibody DPD [37], energy-conserving DPD [38], and smoothed DPD (SDPD)[7]. For a classical DPD solvent we observe k dependence of macroscopic coefficients. This finding is in an agreement with the previous work on the topic [17]. On large scales, liquid behavior can be described by the Landau-Lifshitz

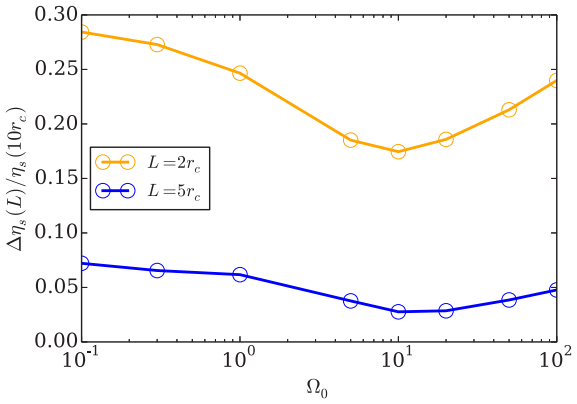

FIG. 12. Decreasing of viscosity for the case $a_{ij} = 18.75k_BT$ relative to the viscosity with wavelength $L = 10r_c$. In the legend $\eta_s(L)$ is a shear viscosity on wavelength L and relative error is estimated as $[\eta_s(L) - \eta_s(10r_c)]/\eta_s(10r_c)$. Different Ω_0 are considered.

Navier-Stokes equations, where viscosity does not depend on k. Beyond a certain scale, macroscopic parameters depend on k, and one has to account for such a dependence in the underlying model. One possibility is offered by the Lennard-Jones molecular dynamics (L-J MD) solvent. L-J MD has k-dependent macroscopic parameters and describes small-scale behavior of liquids [20]. DPD is a mesoscale model which has a wide range of applications and often is used to represent complex microfluidics phenomena where thermal fluctuations are important. We demonstrate the k dependency of macroscopic parameters of a DPD solvent which can be interpreted in two different ways: as a numerical artifact which one would like to avoid when DPD is used to model hydrodynamic length scales, or as an additional feature which allows us to model phenomena beyond the hydrodynamic limit. The described analysis can be applied in both cases, in order to modify the DPD solvent to minimize modeling artifacts, or to model small length scales beyond the hydrodynamic limit.

To minimize numerical artifacts when the length scales of interest are large enough and macroscopic parameters in liquids are known to be constant, one may consider other variants of the DPD solvent, such as SDPD. Another way to avoid the k dependence of macroscopic parameters may be to consider different kinds of DPD kernel functions. These studies are beyond the scope of the current paper.

On the other hand, the k dependence of macroscopic parameters is directly related to memory effects [20]. In recent studies the possibility of a physically motivated model for memory functions with a DPD solvent was demonstrated [39,40]. Using techniques described in the current paper, one can compare a classical DPD solvent with L-J MD simulations for different length scales and model memory effects of L-J MD according to such approaches. This allows us to increase the scale where a DPD model represents physical phenomena.

We observe no sharp critical limit beyond which DPD macroscopic parameters become constant. The evolution of macroscopic parameters losing their k dependence with increasing length scale is rather smooth. Figure 12 shows a comparison of relative viscosity differences of that at wavelength $L = 10r_c$ with that at wavelengths $L = 5r_c$ and $2r_c$. Different parameters Ω_0 are considered. One can observe that the viscosity at $L = 2r_c$ is smaller by 20–30% in comparison with the viscosity at wavelength $L = 10r_c$. Further investigations are needed to establish whether the k dependence of the viscosity affects the diffusion of colloids and polymers in DPD simulations.

The approach for assessing the isothermal speed of sound and the bulk viscosity may be improved for the case of zero repulsive potential by considering a more suitable approximation function for longitudinal FTVACF and FTDACF. For an accurate approximation function one would expect a similar prediction of macroscopic transport coefficients for both methods. With the nonexponential approximation we find a good agreement between predictions of the isothermal speed of sound derived from an analysis of FTVACF and FTDACF for the case of nonzero repulsive potential. The analyses show similar results for the prediction of bulk viscosity from FTVACF and FTDACF only for large length scales. The truncation error on small scales or on large scales can be estimated to improve the accuracy of the DPD solvent prediction, which is the subject of future work. For a DPD solvent with $\Omega_0 > 20$ new approximation functions which account for the long tail of DPD FTVACF should be introduced. In principle one can consider using machine-learning algorithms for the prediction of FTVACF in order to reduce the statistical error as well as the simulation length which is necessary for the derivation of macroscopic transport coefficients of particle methods.

ACKNOWLEDGMENTS

X.B. acknowledges George Em Karniadakis for both discussion and support for visiting Technische Universität München (TUM). The first author acknowledges travel support due to the TUM Graduate School. We thank the Munich Center of Advanced Computing for providing computational resources.

APPENDIX: RELATION OF DYNAMIC OVERLAP AND TEMPERATURE

We follow [17] and introduce the dynamic distance as

$$l_0 := t_0 v_0. \tag{A1}$$

Upon taking corresponding expressions for t_0 and v_0, one obtains

$$l_0 = \frac{1}{\omega_0}\sqrt{k_BT/m}. \tag{A2}$$

We insert the expressions for $\omega_0 := \frac{1}{d}\rho[\boldsymbol{r}w_D]_{\boldsymbol{r}}\gamma$ from Table I and $\gamma = \frac{\sigma^2}{2k_BT}$ from Table II into Eq. (A2) to get

$$l_0 = \frac{2k_BT}{\frac{1}{d}[\boldsymbol{r}w_D]_{\boldsymbol{r}}\rho\sigma^2}\sqrt{k_BT/m}. \tag{A3}$$

A typical DPD kernel is

$$w^D(r_{ij}) = [w^R(r_{ij})]^2 = \begin{cases} (1 - r_{ij})^{2\kappa}, & r_{ij} < r_c \\ 0, & r_{ij} \geqslant r_c \end{cases}, \quad \text{(A4)}$$

where κ is the parameter that controls kernel smoothness. Integration between zero and cutoff radius gives

$$[\boldsymbol{r} w_D]_{\boldsymbol{r}} = \int_0^{r_c} w_D(\boldsymbol{r}) d\boldsymbol{r} = \frac{8\pi r_c^3}{(2\kappa+1)(2\kappa+2)(2\kappa+3)}. \quad \text{(A5)}$$

We use $\kappa = 1$ and obtain

$$[\boldsymbol{r} w_D]_{\boldsymbol{r}} = \frac{8\pi r_c^3}{60}. \quad \text{(A6)}$$

Equation (A3) for the case of $d = 3$ dimensions becomes

$$l_0 = \frac{45 k_B T}{\pi r_c^3 \rho \sigma^2} \sqrt{k_B T / m}. \quad \text{(A7)}$$

Consequently, we obtain Eq. (42):

$$k_B T = \left(\frac{\pi m^{3/2} \rho r_c^3 l_0 \sigma^2}{45} \right)^{\frac{2}{3}}, \quad \text{(A8)}$$

where $\Omega_0 := \frac{r_c}{l_0}$. From that the relation between $k_B T$ and the nondimensional parameter Ω_0 follows as

$$k_B T = \left(\frac{\pi m^{3/2} \rho r_c^4 \sigma^2}{45 \Omega_0} \right)^{\frac{2}{3}}. \quad \text{(A9)}$$

[1] P. J. Hoogerbrugge and J. M. V. A. Koelman, Europhys. Lett. **19**, 155 (1992).
[2] R. D. Groot and P. B. Warren, J. Chem. Phys. **107**, 4423 (1997).
[3] D. A. Fedosov, B. Caswell, and G. E. Karniadakis, Biophys. J. **98**, 2215 (2010).
[4] E. S. Boek, P. V. Coveney, H. N. W. Lekkerkerker, and P. van der Schoot, Phys. Rev. E **55**, 3124 (1997).
[5] E. S. Boek, P. V. Coveney, and H. N. W. Lekkerkerker, J. Phys.: Condens. Matter **8**, 9509 (1996).
[6] E. E. Keaveny, I. V. Pivkin, M. Maxey, and G. E. Karniadakis, J. Chem. Phys. **123**, 104107 (2005).
[7] P. Espanol and M. Revenga, Phys. Rev. E **67**, 026705 (2003).
[8] J. Monaghan, Annu. Rev. Fluid Mech. **44**, 323 (2012).
[9] J. Kordilla, W. Pan, and A. Tartakovsky, J. Chem. Phys. **141**, 224112 (2014).
[10] X. Fan, N. Phan-Thien, N. T. Yong, X. Wu, and D. Xu, Phys. Fluids **15**, 11 (2003).
[11] J. A. Backer, Ph.D. thesis, University of Amsterdam, 2006.
[12] J. A. Backer, C. P. Lowe, H. C. J. Hoefsloot, and P. D. Iedema, J. Chem. Phys. **122**, 154503 (2005).
[13] D. A. Fedosov, G. E. Karniadakis, and B. Caswell, J. Chem. Phys. **132**, 144103 (2010).
[14] B. J. Palmer, Phys. Rev. E **49**, 359 (1994).
[15] C. A. Marsh, Ph.D. thesis, University of Oxford, 1998.
[16] C. A. Marsh, G. Backx, and M. H. Ernst, Phys. Rev. E **56**, 1676 (1997).
[17] M. Ripoll, M. H. Ernst, and P. Espanol, J. Chem. Phys. **115**, 7271 (2001).
[18] C.-C. Huang, G. Gompper, and R. G. Winkler, Phys. Rev. E **86**, 056711 (2012).
[19] B. Hess, J. Chem. Phys. **116**, 209 (2002).
[20] J. P. Boon and S. Yip, *Molecular Hydrodynamics* (Dover, New York, 1992).
[21] P. Espanol and P. Warren, Europhys. Lett. **30**, 191 (1995).
[22] S. Plimpton, J. Comput. Phys. **117**, 1 (1995).
[23] A. Vazquez-Quesada, M. Ellero, and P. Espanol, Phys. Rev. E **79**, 056707 (2009).
[24] H. A. Posch and W. G. Hoover, Physica A **240**, 286 (1997).
[25] G. De Fabritiis, M. Serrano, R. Delgado-Buscalioni, and P. V. Coveney, Phys. Rev. E **75**, 026307 (2007).
[26] X. Bian, Z. Li, and G. E. Karniadakis, J. Comput. Phys. **297**, 132 (2015).
[27] K. Balakrishnan, A. L. Garcia, A. Donev, and J. B. Bell, Phys. Rev. E **89**, 013017 (2014).
[28] A. Donev, J. B. Bell, A. de la Fuente, and A. L. Garcia, Phys. Rev. Lett. **106**, 204501 (2011).
[29] F. Balboa, J. B. Bell, R. Delgado-Buscalioni, A. Donev, T. G. Fai, B. E. Griffith, and C. S. Peskin, Multiscale Model. Simul. **10**, 1369 (2012).
[30] J. B. Bell, A. L. Garcia, and S. A. Williams, Phys. Rev. E **76**, 016708 (2007).
[31] L. D. Landau and E. M. Lifshitz, *Fluid Mechanics*, Course of Theoretical Physics Vol. 6 (Pergamon, London, 1959).
[32] B. J. Berne and G. D. Harp, *Advances in Chemical Physics* (Wiley, New York, 2007).
[33] B. J. Berne and R. Pecora, *Dynamic Light Scattering: With Applications to Chemistry, Biology, and Physics*, unabridged ed. (Dover, New York, 2000).
[34] P. Espanol and M. Serrano, Phys. Rev. E **59**, 6340 (1999).
[35] R. Zwanzig, Annu. Rev. Phys. Chem. **16**, 67 (1965).
[36] A. Boromand, S. Jamali, and J. M. Maia, Comput. Phys. Commun. **196**, 149 (2015).
[37] I. Pagonabarraga and D. Frenkel, J. Chem. Phys. **115**, 5015 (2001).
[38] Z. Li, Y.-H. Tang, H. Lei, B. Caswell, and G. E. Karniadakis, J. Comput. Phys. **265**, 113 (2014).
[39] Z. Li, X. Bian, B. Caswell, and G. E. Karniadakis, Soft Matter **10**, 8659 (2014).
[40] Z. Li, X. Bian, X. Li, and G. E. Karniadakis, J. Chem. Phys. **143**, 243128 (2015).

A.3 Discussions on the correspondence of dissipative particle dynamics and Langevin dynamics at small scales

SPRINGER NATURE LICENSE
TERMS AND CONDITIONS

Jan 16, 2018

This Agreement between Mr. Dmitrii Azarnykh ("You") and Springer Nature ("Springer Nature") consists of your license details and the terms and conditions provided by Springer Nature and Copyright Clearance Center.

License Number	4270591441391
License date	Jan 16, 2018
Licensed Content Publisher	Springer Nature
Licensed Content Publication	Applied Mathematics and Mechanics
Licensed Content Title	Discussions on the correspondence of dissipative particle dynamics and Langevin dynamics at small scales
Licensed Content Author	D. Azarnykh, S. Litvinov, X. Bian et al
Licensed Content Date	Jan 1, 2018
Licensed Content Volume	39
Licensed Content Issue	1
Type of Use	Thesis/Dissertation
Requestor type	academic/university or research institute
Format	print and electronic
Portion	full article/chapter
Will you be translating?	no
Circulation/distribution	>50,000
Author of this Springer Nature content	yes
Title	Mr.
Instructor name	Dmitrii Azarnykh
Institution name	Technical University of Munich
Expected presentation date	Mar 2018
Portions	As I am going to submit cumulative thesis, I would like to include the full article to my thesis. The version is the same as it is available online, without any changes or comments.
Requestor Location	Mr. Dmitrii Azarnykh Strassbergerstr. 24 Munich, Bayern 80809 Germany Attn: Mr. Dmitrii Azarnykh
Billing Type	Invoice
Billing Address	Mr. Dmitrii Azarnykh Strassbergerstr. 24 Munich, Germany 80809 Attn: Mr. Dmitrii Azarnykh
Total	0.00 EUR

Terms and Conditions

Springer Nature Terms and Conditions for RightsLink Permissions

Springer Customer Service Centre GmbH (the Licensor) hereby grants you a non-exclusive, world-wide licence to reproduce the material and for the purpose and requirements specified in the attached copy of your order form, and for no other use, subject to the conditions below:

1. The Licensor warrants that it has, to the best of its knowledge, the rights to license reuse of this material. However, you should ensure that the material you are requesting is original to the Licensor and does not carry the copyright of another entity (as credited in the published version).

   If the credit line on any part of the material you have requested indicates that it was reprinted or adapted with permission from another source, then you should also seek permission from that source to reuse the material.

2. Where **print only** permission has been granted for a fee, separate permission must be obtained for any additional electronic re-use.

3. Permission granted **free of charge** for material in print is also usually granted for any electronic version of that work, provided that the material is incidental to your work as a whole and that the electronic version is essentially equivalent to, or substitutes for, the print version.

4. A licence for 'post on a website' is valid for 12 months from the licence date. This licence does not cover use of full text articles on websites.

5. Where **'reuse in a dissertation/thesis'** has been selected the following terms apply: Print rights for up to 100 copies, electronic rights for use only on a personal website or institutional repository as defined by the Sherpa guideline (www.sherpa.ac.uk/romeo/).

6. Permission granted for books and journals is granted for the lifetime of the first edition and does not apply to second and subsequent editions (except where the first edition permission was granted free of charge or for signatories to the STM Permissions Guidelines http://www.stm-assoc.org/copyright-legal-affairs/permissions/permissions-guidelines/), and does not apply for editions in other languages unless additional translation rights have been granted separately in the licence.

7. Rights for additional components such as custom editions and derivatives require additional permission and may be subject to an additional fee. Please apply to

Journalpermissions@springernature.com/bookpermissions@springernature.com for these rights.

8. The Licensor's permission must be acknowledged next to the licensed material in print. In electronic form, this acknowledgement must be visible at the same time as the figures/tables /illustrations or abstract, and must be hyperlinked to the journal/book's homepage. Our required acknowledgement format is in the Appendix below.
9. Use of the material for incidental promotional use, minor editing privileges (this does not include cropping, adapting, omitting material or any other changes that affect the meaning, intention or moral rights of the author) and copies for the disabled are permitted under this licence.
10. Minor adaptations of single figures (changes of format, colour and style) do not require the Licensor's approval. However, the adaptation should be credited as shown in Appendix below.

Appendix — Acknowledgements:

For Journal Content:
Reprinted by permission from [**the Licensor**]: [**Journal Publisher** (e.g. Nature/Springer/Palgrave)] [**JOURNAL NAME**] [**REFERENCE CITATION** (Article name, Author(s) Name), [**COPYRIGHT**] (year of publication)

For **Advance Online Publication papers:**
Reprinted by permission from [**the Licensor**]: [**Journal Publisher** (e.g. Nature/Springer/Palgrave)] [**JOURNAL NAME**] [**REFERENCE CITATION** (Article name, Author(s) Name), [**COPYRIGHT**] (year of publication), advance online publication, day month year (doi: 10.1038/sj.[JOURNAL ACRONYM].)

For Adaptations/Translations:
Adapted/Translated by permission from [**the Licensor**]: [**Journal Publisher** (e.g. Nature/Springer/Palgrave)] [**JOURNAL NAME**] [**REFERENCE CITATION** (Article name, Author(s) Name), [**COPYRIGHT**] (year of publication)

Note: For any republication from the British Journal of Cancer, the following credit line style applies:

Reprinted/adapted/translated by permission from [**the Licensor**]: on behalf of Cancer Research UK: : [**Journal Publisher** (e.g. Nature/Springer/Palgrave)] [**JOURNAL NAME**] [**REFERENCE CITATION** (Article name, Author(s) Name), [**COPYRIGHT]** (year of publication)

For **Advance Online Publication** papers:
Reprinted by permission from The [**the Licensor**]: on behalf of Cancer Research UK: [**Journal Publisher** (e.g. Nature/Springer/Palgrave)] [**JOURNAL NAME**] [**REFERENCE CITATION** (Article name, Author(s) Name), [**COPYRIGHT**] (year of publication), advance online publication, day month year (doi: 10.1038/sj.[JOURNAL ACRONYM])

For Book content:
Reprinted/adapted by permission from [**the Licensor**]: [**Book Publisher** (e.g. Palgrave Macmillan, Springer etc) [**Book Title**] by [**Book author**(s)] [**COPYRIGHT**] (year of publication)

Other Conditions:

Version 1.0

Appl. Math. Mech. -Engl. Ed., **39**(1), 31–46 (2018)

Applied Mathematics and Mechanics (English Edition)

https://doi.org/10.1007/s10483-018-2258-9

Discussions on the correspondence of dissipative particle dynamics and Langevin dynamics at small scales*

D. AZARNYKH[1], S. LITVINOV[2], X. BIAN[1,†], N. A. ADAMS[1]

1. Chair of Aerodynamics and Fluid Mechanics, Department of Mechanical Engineering, Technical University of Munich, München 85748, Germany;
2. Chair of Computational Science, Eidgenössische Technische Hochschule Zürich, Zurich CH-8092, Switzerland

(Received Aug. 10, 2017 / Revised Nov. 10, 2017)

Abstract We investigate the behavior of dissipative particle dynamics (DPD) within different scaling regimes by numerical simulations. The paper extends earlier analytical findings of Ripoll, M., Ernst, M. H., and Español, P. (Large scale and mesoscopic hydrodynamics for dissipative particle dynamics. *Journal of Chemical Physics*, **115**(15), 7271–7281 (2001)) by evaluation of numerical data for the particle and collective scaling regimes and the four different subregimes. DPD simulations are performed for a range of dynamic overlapping parameters. Based on analyses of the current auto-correlation functions (CACFs), we demonstrate that within the particle regime at scales smaller than its force cut-off radius, DPD follows Langevin dynamics. For the collective regime, we show that the small-scale behavior of DPD differs from Langevin dynamics. For the wavenumber-dependent effective shear viscosity, universal scaling regimes are observed in the microscopic and mesoscopic wavenumber ranges over the considered range of dynamic overlapping parameters.

Key words dissipative particle dynamics (DPD), mesoscopic dynamics, fluctuating hydrodynamics

Chinese Library Classification O352
2010 Mathematics Subject Classification 82-08, 82C31, 76M28

1 Introduction

For the modeling of fluid flow, different methodologies are employed when the interest is on macroscopic or on microscopic scales. Macroscopic scales typically are described by the continuum or Navier-Stokes (NS) equations, whereas for microscopic scales, the molecular dynamics (MD) method with realistic potentials can be used. For the intermediate mesoscopic scales, NS and MD cannot be applied directly. The NS equations may be extended to the mesoscopic range by adding a stochastic stress, which results in the Landau-Lifshitz Navier-Stokes (LLNS) equations[1]. Since the LLNS equations are based on the continuum hypothesis, they are still

* Citation: Azarnykh, D., Litvinov, S., Bian, X., and Adams, N. A. Discussions on the correspondence of dissipative particle dynamics and Langevin dynamics at small scales. *Applied Mathematics and Mechanics* (*English Edition*), **39**(1), 31–46 (2018) https://doi.org/10.1007/s10483-018-2258-9

† Corresponding author, E-mail: xin.bian@tum.de

inappropriate when the spatial scales approach the dimension of molecules. Given an accurate force field, MD is valid at any length scale. However, it is computationally unfeasible to simulate a reasonably complex fluid flow with MD. A gap exists between the length scales that can be efficiently simulated by MD and those where the NS or LLNS equations become valid. As an attempt to bridge the gap, dissipative particle dynamics (DPD) was invented[2–4]. It is a Lagrangian particle method operating at the mesoscopic scales. DPD has been successfully applied to study a wide range of phenomena, such as solubility of polymers[4], rheology of colloids[5], and dynamics of membranes[6].

As the mesoscopic scales described by the DPD method overlap with macroscopic and microscopic scales, it is necessary to establish relations between DPD and MD for the small-scale limit and between DPD and NS/LLNS for the large-scale limit. It is difficult to develop generally valid formal relations for these limits. Assumptions and restrictions have always been made for each individual scenario. For example, a formal connection between DPD and MD has been established for structured fluids[7–8] using the Mori-Zwanzig projection formalism[9–10]. However, for a simple fluid, a correspondence between DPD particles and MD particles is unclear, and a formal connection is still under development[11]. Other attempts to develop a formal relation between DPD and NS equations have also been made in several early studies. In Refs. [12] and [13], a kinetic theory was used to connect the DPD input parameters (without conservative force) to output transport coefficients. In Ref. [14], analytical expressions of wavenumber-dependent macroscopic properties have been derived for a two-dimensional system. The extension of such analysis to three dimensions is difficult. Moreover, often the assumption of exponential decay of the current auto-correlation function (CACF) is invoked to proceed with analytical derivations, which may be invalid, however, for small scales of DPD. Hence, the relations derived so far cannot cover the entire range of DPD parameters.

An interpretation of DPD from a top-down perspective has enabled a successful alternative approach. In a seminal paper[15], Español and Revenga started with a Lagrangian discretization of the NS equations using the smoothed particle hydrodynamics (SPH) method[16–17] and introduced thermal fluctuations directly on the Lagrangian particles following the general equation for non-equilibrium reversible-irreversible coupling (GENERIC) framework[18]. To reflect that it bridges DPD and SPH, this method is called smoothed dissipative particle dynamics (SDPD). Soon after its invention, SDPD has been applied to many problems, such as flows of red blood cells[19], colloidal particles[20], DNA chains[21], and viscoelastic liquids[22]. However, to capture unconventional phenomena beyond the continuum limit, SDPD has to be modified or extended[23–24].

In this paper, we choose to analyze DPD. To be more specific about the possible significance of analyzing the small scale dynamics of DPD, we outline three illustrative examples as motivation for our work.

Soddemann et al.[25] realized that DPD equations (with only friction and stochastic forces) can be utilized as an effective thermostat as alternative to the Langevin equations (LEs) for MD simulations. Due to momentum conservation, DPD indeed provides correct and unscreened hydrodynamic correlations of the MD system. Moreover, the effect of the DPD friction parameter on the intrinsic viscosity of microcanonical MD was studied extensively[25–27]. Nevertheless, at least two questions remain open: (i) it is unclear how the friction parameter may affect small-scale dynamics of microcanonical systems, (ii) whether the DPD thermostat effects are comparable to the Langevin thermostat at these small scales.

In another study[28], the equation of motion for DPD particles without conservative force was rewritten as (see Eq. (13) in Ref. [28])

$$\mathrm{d}\boldsymbol{v}_i = -\frac{\gamma}{d}(\boldsymbol{v}_i - \boldsymbol{V}_i)\mathrm{d}t + \breve{\boldsymbol{F}}\mathrm{d}t, \tag{1}$$

where an environment velocity $\boldsymbol{V}_i$ and the random force $\breve{\boldsymbol{F}}$ are defined using properties of the

neighboring particles (the other terms are defined in Section 2). Equation (1) suggests that DPD shares similarities with the LE. Furthermore, in the regime of large overlapping parameter, or large number of neighboring particles, the velocity auto-correlation of a tagged particle is predicted well by the analytical expressions derived from Eq. (1). In other regimes, however, the relation between DPD and the LE is unknown.

DPD is a dissipative system with conservation of the momentum. Another well-known model with such properties is the hybrid Lagrangian-Eulerian approach[29]. The Eulerian part serves to conserve momentum of the particle-based system, which is usually described by the LEs. A similar approach can also be applied to model rarefied gases[30]. It appears that the application range of DPD may be extended to such situations, provided that the small-scale behavior of DPD is fully understood.

In the current work, we apply numerical analysis to investigate the behavior of DPD on small scales in three dimensions. In particular, we measure the CACFs of DPD in Fourier space and compare them with analytical expressions that can be derived for LLNS and LEs. We demonstrate similarities and differences of DPD with other systems and come to conclusions about the correspondence between DPD and LEs. The remainder of the paper is structured as follows: in Section 2, we describe the DPD method with a short review of previous findings on DPD macroscopic properties; in Section 3, we discuss properties of the CACFs of the LLNS equations and the LEs; in Section 4, the CACFs of DPD obtained from simulations are compared with the analytical solutions of CACF for the LE; in Section 5, we summarize our results and come to conclusions.

2 DPD model

DPD is a multi-particle model. A pairwise force $\boldsymbol{F}_{ij}$ acts on each particle i and shifts its locations

$$\frac{\mathrm{d}\boldsymbol{r}_i}{\mathrm{d}t} = \boldsymbol{v}_i, \quad \frac{\mathrm{d}\boldsymbol{v}_i}{\mathrm{d}t} = \frac{1}{m}\sum_{j\neq i}\boldsymbol{F}_{ij}. \tag{2}$$

The force $\boldsymbol{F}_{ij}$ consists of three different parts: conservative force $\boldsymbol{F}_{ij}^{\mathrm{C}}$, dissipative force $\boldsymbol{F}_{ij}^{\mathrm{D}}$, and random force $\boldsymbol{F}_{ij}^{\mathrm{R}}$, that is,

$$\boldsymbol{F}_{ij} = \boldsymbol{F}_{ij}^{\mathrm{C}} + \boldsymbol{F}_{ij}^{\mathrm{D}} + \boldsymbol{F}_{ij}^{\mathrm{R}}. \tag{3}$$

In this paper, we consider DPD without the conservative force, $\boldsymbol{F}_{ij}^{\mathrm{C}} = 0$. This choice is motivated by the objective of comparing thermostat characteristics of LEs with that of DPD. In addition, analytical properties of the corresponding LEs (without conservative force) can be derived straightforwardly.

Dissipative and random forces in DPD are defined as

$$\boldsymbol{F}_{ij}^{\mathrm{D}} = -m\gamma w^{\mathrm{D}}(r_{ij})(\widehat{\boldsymbol{r}}_{ij}\cdot\boldsymbol{v}_{ij})\widehat{\boldsymbol{r}}_{ij}, \tag{4}$$

$$\boldsymbol{F}_{ij}^{\mathrm{R}} = m\sigma w^{\mathrm{R}}(r_{ij})\theta_{ij}\widehat{\boldsymbol{r}}_{ij}, \tag{5}$$

where the weighting functions $w^{\mathrm{D}}(r_{ij})$ and $w^{\mathrm{R}}(r_{ij})$ as well as the dissipation coefficient γ and the random coefficient σ are related so that they satisfy the fluctuation-dissipation balance[3]

$$w^{\mathrm{D}}(r_{ij}) = (w^{\mathrm{R}}(r_{ij}))^2, \quad \gamma = \frac{\sigma^2}{2k_{\mathrm{B}}T}. \tag{6}$$

We define $\boldsymbol{r}_{ij} = \boldsymbol{r}_i - \boldsymbol{r}_j$, $r_{ij} = |\boldsymbol{r}_{ij}|$, and $\widehat{\boldsymbol{r}}_{ij} = \boldsymbol{r}_{ij}/r_{ij}$ as relative position, distance, and unit vector between two particles i and j, respectively. k_{B} is the Boltzmann constant, and T is the temperature. $\boldsymbol{v}_{ij} = \boldsymbol{v}_i - \boldsymbol{v}_j$ is the relative velocity, and θ_{ij} is a Gaussian random variable with the properties[3]

$$\langle\theta_{ij}(t)\rangle = 0, \tag{7}$$

$$\langle \theta_{ij}(t)\theta_{kl}(t')\rangle = (\delta_{ik}\delta_{jl} + \delta_{il}\delta_{jk})\delta(t-t'), \tag{8}$$

where $\delta(t)$ is the Dirac delta, and δ_{ij} is the Kronecker delta. We choose the standard weighting functions as[4]

$$w^{\mathrm{D}}(r_{ij}) = (w^{\mathrm{R}}(r_{ij}))^2 = \begin{cases} \left(1 - \dfrac{r_{ij}}{r_{\mathrm{c}}}\right)^2, & r_{ij} < r_{\mathrm{c}}, \\ 0, & r_{ij} \geqslant r_{\mathrm{c}}. \end{cases} \tag{9}$$

Properties of DPD are determined by a priori chosen parameters, which relate microscopic, macroscopic, and mesoscopic scales of motion. We follow previous works[14,31–32] by considering wavenumber dependent macroscopic properties. The wavenumber $q = 2\pi/\lambda$ corresponds to the length scale of interest $\lambda = L/n$ with $n = 1, 2, 3, \cdots$ and L is the length of the domain. The specific dependence of macroscopic properties on q in DPD, such as the effective shear viscosity $\nu(q)$, the effective bulk viscosity $\zeta(q)$, and the effective isothermal speed of sound $c_{\mathrm{t}}(q)$, varies with length scales. With DPD, one can distinguish three different characteristic length scales: cut-off radius r_{c}, decorrelation length l_0 of particles, and length of interest λ. The decorrelation length l_0 of DPD particles is analogous to the mean free path[14]. Depending on the relation of the cut-off radius r_{c} to the decorrelation length l_0 of DPD particles, different scaling regimes were defined[14]: the collective regime $r_{\mathrm{c}} > l_0$ and the particle regime $r_{\mathrm{c}} < l_0$. Please refer to Table 1 for a classification. In analogy to the length-scale parameter l_0, the collision time $t_0 = l_0/v_0$ was defined as time-scale parameter[14], where v_0 is the thermal velocity. Please refer to Table 2 for the definitions of variables. In the collective regime within the collision time t_0, particles on the average do not travel far enough before interacting with neighboring particles multiple times. This situation is common for liquid molecules. In the particle regime, particles encounter less frequent interactions with the same neighboring particles and rather interact with new neighbors. The particle regime is typical for gas molecules. One can choose between collective or particle regime by setting the parameters of DPD appropriately.

For the collective regime of DPD, one can distinguish three different subregimes: the standard hydrodynamic subregime $\lambda > r_{\mathrm{c}} > l_0$, the mesoscopic subregime $r_{\mathrm{c}} > \lambda > l_0$, and the N-particle subregime $r_{\mathrm{c}} > l_0 > \lambda$. Macroscopic properties of DPD in the standard hydrodynamic subregime do not depend on wavenumber and correspond to the isothermal NS equations[14].

Table 1 Regimes of DPD and corresponding subregimes

Collective regime ($r_{\mathrm{c}} > l_0$)	Particle regime ($l_0 > r_{\mathrm{c}}$)
$\lambda > r_{\mathrm{c}} > l_0$, NS	$\lambda > l_0 > r_{\mathrm{c}}$, NS
$r_{\mathrm{c}} > \lambda > l_0$, mesoscopic	$l_0 > \lambda > r_{\mathrm{c}}$, kinetic
$r_{\mathrm{c}} > l_0 > \lambda$, N-particle	$l_0 > r_{\mathrm{c}} > \lambda$, N-particle

Table 2 DPD nondimensional parameters

Parameter	Meaning	Definition
ν	Effective shear viscosity	$\frac{\eta_s}{\rho}$
ζ	Effective bulk viscosity	$\frac{\eta_\nu}{\rho}$
v_0	Thermal velocity	$\sqrt{k_{\mathrm{B}}T/m}$
$[\cdots]_{\boldsymbol{r}}$	Volume integral operator	$\int \cdots \mathrm{d}\boldsymbol{r}$
ω_0	Collision frequency	$\frac{1}{d}[w^{\mathrm{D}}]_{\boldsymbol{r}}\gamma$
t_0	Collision time	$\frac{1}{\omega_0}$
l_0	Decorrelation length	$t_0 v_0$ 7
Ω_0	Dynamic overlapping	$\frac{r_{\mathrm{c}}}{l_0}$
$\tilde{q}$	Nondimensional wave number	ql_0
$\tilde{\nu}$	Nondimensional ν	$\frac{\nu}{\omega_0 l_0^2}$
$\tilde{\zeta}$	Nondimensional ζ	$\frac{\zeta}{\omega_0 l_0^2}$

For the particle regime of DPD, one can expect three different subregimes as well[14]: the standard hydrodynamic subregime $\lambda > l_0 > r_c$, the kinetic subregime $l_0 > \lambda > r_c$, and the N-particle subregime $l_0 > r_c > \lambda$. The functional dependence of DPD properties on q varies across the subregimes. Regimes of DPD and corresponding subregimes are summarized in Table 1.

It was shown in Ref. [33] that on the small scales, CACFs of DPD follow non-exponential laws. We investigate this property in detail in this work. For this purpose, we first consider the properties of CACFs for LLNS equations and LEs, followed by a comparison of small-scale behaviors of the LEs and of DPD.

3 CACFs

The CACF $C(q_k, t)$ is defined as[32]

$$C(q_k, t) = \frac{\langle \widehat{w}_l(q_k, 0)\widehat{w}_l(q_k, t)\rangle}{\delta \widehat{w}_l^2(q_k, 0)} \ . \tag{10}$$

Subscripts k, l indicate the wavenumber-vector, current-vector, and velocity-vector components in coordinate directions x, y, z, respectively. $k = l$ results in the longitudinal CACF with $C_\parallel(q, t)$, and $k \neq l$ results in the transverse CACF with $C_\perp(q, t)$. $\delta \widehat{w}_l^2(q_k, t)$ is the variance of the respective Fourier mode of current w.

CACFs are used to analyze MD systems[31–32], fluctuating hydrodynamics[34–35], DPD[33,36–37], and multi-particle collision dynamics solvent[38–39], and are directly related to macroscopic properties, such as the effective shear viscosity, the effective bulk viscosity, and the effective isothermal speed of sound. CACFs may also represent the ensemble-averaged decay of an initial sinusoidal velocity field to the steady state. This property follows from the regression hypothesis of Onsager[40] which states that microscopic thermal fluctuations at equilibrium can be modeled by non-equilibrium transport coefficients. Setting an initial sinusoidal velocity in two different directions parallel or perpendicular to the velocity direction corresponds to longitudinal and transverse CACFs, respectively[34]. In the following subsections, we consider CACFs of two models, that is, the LLNS equations and the LEs, at thermodynamic equilibrium.

3.1 CACFs of the LLNS equations

The LLNS equations are an extension of the NS equations to smaller scales where thermal fluctuations are important[1]. A stochastic term is introduced to account for the spontaneous fluctuations of stresses in a finite thermodynamic system. The dissipative term of the LLNS is the same as that of the NS equations, and the stochastic term in the LLNS together with the dissipative term satisfies the fluctuation-dissipation theorem. For simplicity, in this paper, we consider only isothermal LLNS in the linearized form. For the linearized equations in a periodic domain, one can derive the transverse and longitudinal CACFs as well as density auto-correlation function[41] as

$$C_{\mathrm{LLNS}\perp}(q, t) = \mathrm{e}^{-q^2\nu t}, \tag{11}$$

$$C_{\mathrm{LLNS}\parallel}(q, t) = \mathrm{e}^{-q^2\Gamma t}\cos(\Theta q t) - \frac{q\Gamma}{\Theta}\mathrm{e}^{-q^2\Gamma t}\sin(\Theta q t), \tag{12}$$

$$C_{\mathrm{LLNS}\rho}(q, t) = \mathrm{e}^{-q^2\Gamma t}\cos(\Theta q t) + \frac{q\Gamma}{\Theta}\mathrm{e}^{-q^2\Gamma t}\sin(\Theta q t), \tag{13}$$

respectively, where

$$\Theta = \frac{\sqrt{4\,c_t^2 - q^2\Gamma^2}}{2}, \quad \Gamma = \Big(1 - \frac{1}{d}\Big)\nu + \frac{1}{2}\zeta. \tag{14}$$

3.2 CACFs of the LEs

The LEs were introduced to describe the Brownian motion of particles[42]. In this section, we consider one particle driven by the LE

$$\dot{\boldsymbol{x}} = \boldsymbol{v}, \tag{15}$$

$$\dot{\boldsymbol{v}} = -\beta \boldsymbol{v} + \boldsymbol{\theta}(t). \tag{16}$$

Here, we take a constant dissipation coefficient β and a delta-correlated in time Gaussian random variable $\theta_{k,i}$,

$$\langle \theta(t) \rangle = 0, \tag{17}$$

$$\langle \theta(t)\theta(t') \rangle = \frac{2k_{\mathrm{B}}T\beta}{m}\delta(t-t'), \tag{18}$$

where k_{B} is the Boltzmann constant, T is the temperature, and m is the mass of the particle.

The CACFs can be derived from simulations or analytically. An analytical derivation is provided in the Appendix for reference. The CACFs of the LEs are

$$C_{\mathrm{LE}\perp} = \exp(-\beta t) \times \exp\Big(-\frac{q^2 k_{\mathrm{B}}T}{\beta^2 m}(\beta t - 1 + \mathrm{e}^{-\beta t})\Big), \tag{19}$$

$$C_{\mathrm{LE}\parallel} = \Big(\mathrm{e}^{\beta t} - q^2\Big(\frac{k_{\mathrm{B}}T}{\beta^2 m}\Big)(\mathrm{e}^{\beta t}-1)^2\Big) \times \exp(-2\beta t) \exp\Big(-\frac{q^2 k_{\mathrm{B}}T}{\beta^2 m}(\beta t - 1 + \mathrm{e}^{-\beta t})\Big), \tag{20}$$

$$C_{\mathrm{LE}\rho} = \exp\Big(-\frac{q^2 k_{\mathrm{B}}T}{\beta^2 m}(\beta t - 1 + \mathrm{e}^{-\beta t})\Big). \tag{21}$$

We compare the analytical expressions with simulations. In the simulations, for one particle, we take[33]

$$\widehat{w}_l(q_k, t) = v_l(k,t)\sin(kq_k), \tag{22}$$

where k, $l = x, y, z$ are direction indices. Equation (22) can be used to compute CACFs according to Eq. (10). Equation (10) for N_{r} independent realizations gives

$$C(q_k, t) = \sum_{i=1}^{N_{\mathrm{r}}} \frac{1}{N_{\mathrm{r}}} \frac{\langle \widehat{w}_l(q_k,0)\widehat{w}_l(q_k,t)\rangle_i}{\delta \widehat{w}_l^2(q_k,0)}, \tag{23}$$

where angular parentheses $\langle\cdot\rangle_i$ denote averaging in time of the ith realization. In order to determine the CACFs for LEs, we perform a numerical simulation with one particle moving according to the LEs (15) and (16) with $k_{\mathrm{B}}T = 0.25$ and $\beta = 0.1$. The particle moves in a three-dimensional box of size $250\times250\times250$ with periodic boundary conditions. For the simulation, we use the velocity-verlet algorithm for integration in time. The number of independent realizations is $N_{\mathrm{r}} = 128$, and the time interval of each simulation spans $T = 5 \times 10^5$ time units. The comparison of numerical results with theoretical predictions for CACFs is presented in Fig. 1 for different wavenumbers. The statistical errors in Fig. 1 are smaller than the symbol size. The results show that the numerical simulations agree well with the analytical predictions for CACFs of LEs, which verifies the numerical approach.

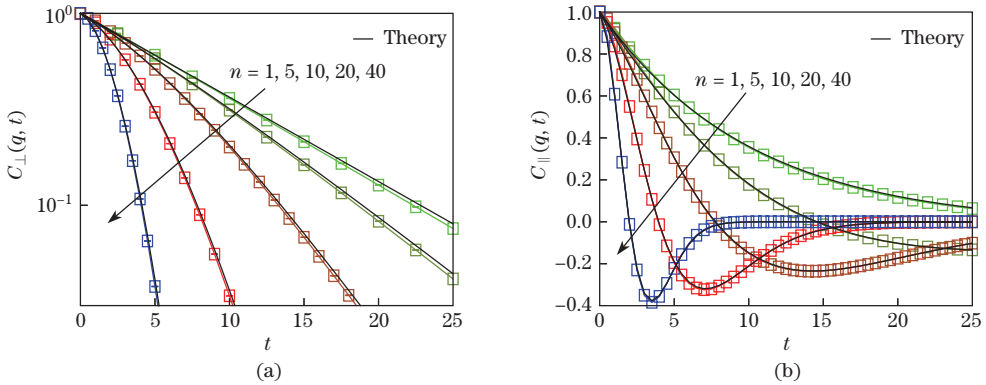

Fig. 1 (a) Transverse CACF $C_{\mathrm{LE}\perp}$ and (b) longitudinal CACF $C_{\mathrm{LE}\parallel}$ of LEs for different integer wavenumbers n. Black solid lines denote the analytical predictions, Eqs. (19) and (20), while colored lines with symbols denote results measured from numerical simulation (Color online)

3.3 Effective shear viscosity

It is convenient to operate with the nondimensional DPD parameters which were introduced in Ref. [14] and are listed in Table 2. Dynamic overlapping Ω_0 is introduced as the ratio between cut-off radius and decorrelation length,

$$\Omega_0 = \frac{r_{\mathrm{c}}}{l_0} = \frac{r_{\mathrm{c}}\rho\gamma(w^{\mathrm{D}})_{\boldsymbol{r}}}{d\sqrt{k_{\mathrm{B}}T/m}}, \tag{24}$$

where ρ is the number density. For the particle regime of DPD, $\Omega_0 < 1$, and for the collective regime, $\Omega_0 > 1$. Analytical estimations of macroscopic DPD properties for large scales and for mesoscopic scales have been derived in Refs. [12]–[14]. For the standard hydrodynamic subregime, the nondimensional effective shear viscosity is estimated as

$$\widetilde{\nu} = \frac{1}{2} + a_2\Omega_0^2, \tag{25}$$

where the coefficient a_2 is

$$a_2 = \frac{3(r^2 w^{\mathrm{D}})_{\boldsymbol{r}}}{2(d+2)r_{\mathrm{c}}^2(w^{\mathrm{D}})_{\boldsymbol{r}}}. \tag{26}$$

For the weighting function of Eq. (9) and $d = 3$, $a_2 = \frac{1}{35}$. In the mesoscopic subregime, the estimation is

$$\widetilde{\nu} = 1 + \widetilde{q}^{\,-2}, \tag{27}$$

whereas in the N-particle subregime of DPD, the estimation is $\widetilde{\nu} = 1$[14].

The common macroscopic definition of viscosity is the coefficient relating the stress tensor to the deformation rate of the fluid[1]. In DPD literature, viscosity is usually defined as a measure of energy dissipation, which is a wavenumber dependent property[12–14]. The energy dissipation in DPD has dissipative and kinematic contributions. The energy dissipation can be derived directly from CACFs. In this paper, we compare CACFs which are derived from Langevin dynamics of a single particle with CACFs derived from DPD simulations. For such a comparison, it is convenient to define a quantity of interest that resembles the definition of DPD viscosity which is used in the literature. However, the definition of this quantity of interest as kinematic viscosity for LEs may be misleading. For this reason, we employ the effective viscosity. In this paper, the effective shear viscosity is defined from transverse CACF as

$$\nu(q) := \frac{1}{q^2}\Big(\int_0^\infty C_\perp(t,q)\mathrm{d}t\Big)^{-1}. \tag{28}$$

This definition allows us to determine the effective shear viscosities for systems without momentum conservation, such as described by the LEs. The effective shear viscosity has the same dimension as the usual kinematic viscosity. Note that the effective shear viscosity defined by Eq. (28) may have properties different from the kinematic shear viscosity in a continuum description. For example, in the limit of $q \to 0$, the effective shear viscosity diverges for Langevin dynamics, but reaches a plateau value for DPD fluids.

The effective shear viscosity ν_{LE} of LE can be derived from the transverse CACF. Upon inserting Eq. (19) into Eq. (28), we obtain

$$\nu_{\mathrm{LE}}(q) = \frac{1}{q^2}\Big(\frac{1}{\beta}A_1^{-A_1-1}\mathrm{e}^{A}(\Gamma(A_1+1) - \Gamma(A_1+1, A_1))\Big)^{-1}, \tag{29}$$

where $\Gamma(s,x) := \int_x^\infty y^{s-1}\mathrm{e}^{-y}\mathrm{d}y$ is the upper incomplete gamma function, $\Gamma(s) := \int_0^\infty y^{s-1}\mathrm{e}^{-y}\mathrm{d}y$ is the gamma function, and $A_1 := \frac{k_{\mathrm{B}}Tq^2}{\beta^2 m}$ is a coefficient.

We emphasize that Eq. (29) does not go beyond what has been covered in the previous studies[43], but it provides a convenient tool to compare properties of Langevin dynamics with that of DPD.

4 CACFs of DPD

In the previous section, we have derived analytical expressions for C_{LLNS} and C_{LE}. In order to measure CACFs of DPD, we consider numerical simulations for different wavenumbers q. We calculate CACFs for DPD using the same numerical technique as for LEs. For N DPD particles, Eq. (22) is

$$\widehat{w}_l(q_k, t) = \sum_{i=1}^{N} v_{l,i}(k,t)\sin(k_i q_k), \tag{30}$$

and the corresponding CACFs can be evaluated according to Eq. (23). The number of independent realizations is $N_{\mathrm{r}} = 16$, and the time interval of each simulation spans $T = 4 \times 10^6$ time units. Simulation parameters are given in Table 3. For DPD simulations, periodic boundary conditions are used. The statistical errors in Fig. 2 and Fig. 3 are smaller than the symbol size. In Fig. 2, the current characteristics of DPD are shown for different wavenumbers and different subregimes. We compare these characteristics with the corresponding analytical predictions derived from the LE theory, Eqs. (19), (20), and (21). The decorrelation length of a particle governed by LE is $l_{\mathrm{LE}} = \sqrt{k_{\mathrm{B}}T/m}/\beta$. Parameters for the analytical predictions are chosen in such a way that the particle in the LE has the decorrelation length equal to the one of DPD l_0 and the relaxation time in the LE is equal to the collision time t_0 of DPD particles.

Table 3 Parameters of DPD simulation

Parameter	Meaning	Numerical value
r_{c}	Cut-off radius	1
m	Mass	1
$L_x \times L_y \times L_z$	Domain size	$10 \times 10 \times 10$
ρ	Number density	4
σ	Random coefficient	3
Ω_0	Dynamics overlapping	$[0.1; 0.3; 1; 5; 10; 20; 50; 100]$
$k_{\mathrm{B}}T$	Temperature	$\Big(\frac{\pi m^{3/2}\rho r_{\mathrm{c}}^4\sigma^2}{45\Omega_0}\Big)^{\frac{2}{3}}$
γ	Dissipative coefficient	$\frac{\sigma^2}{2k_{\mathrm{B}}T}$
d	Dimension	3

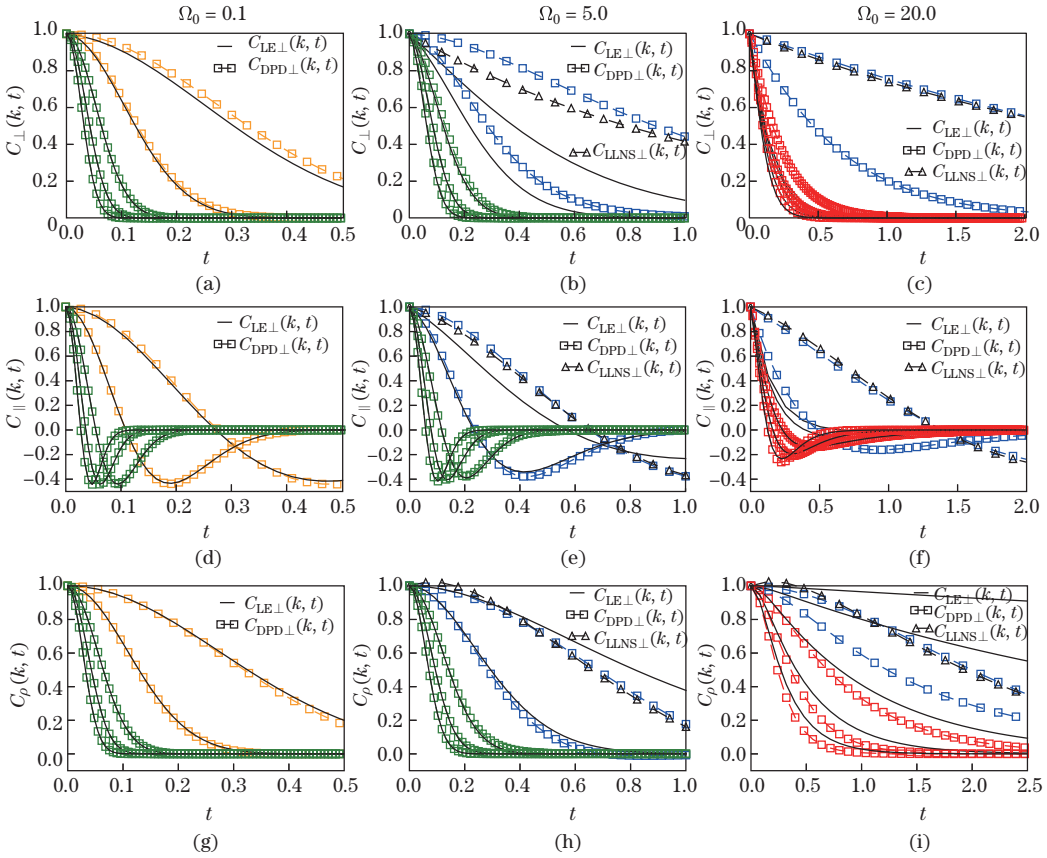

Fig. 2 From top to bottom (a)–(c) transverse CACFs, (d)–(f) longitudinal CACFs, and (g)–(i) density auto-correlation functions, which are derived from DPD simulation and are compared with analytical estimates for LEs (19), (20), and (21). Simulations with different values of dynamic overlapping are presented: $\Omega_0 = 0.1$, 5.0, 20.0 from left to right. In every plot, wavenumbers $n = 2$, 5, 10, 15, 20 are taken. Faster decay of the CACF corresponds to larger wavenumbers. Green, yellow, red, and blue colors correspond to N-particle, kinetic, mesoscopic, and standard hydrodynamic subregimes of DPD, respectively (Color online)

For this purpose, the temperature in the LE is set equal to the temperature in DPD, and the dissipation coefficient in the LE is set the same as the collision frequency in DPD $\beta = \omega_0$. Nondimensional wavenumbers $\widetilde{q}$ in the LE predictions correspond to the ones in DPD. For the N-particle subregime, which is depicted with green color in Fig. 2, we find that the CACFs of DPD are in good agreement with those predicted by the LE theory. The correspondence of CACFs of DPD and LE is independent of the DPD parameters. This observation suggests that the large wavenumbers of DPD have a common, universal behavior. We compare CACFs on small wavenumbers of DPD with CACFs of the LLNS equation. Lines with triangles in Fig. 2 present a fit of CACFs of DPD in the standard hydrodynamic regime with Eqs. (11)–(13). For large dynamic overlapping $\Omega_0 = 20$, DPD agrees with LLNS. Transverse CACFs derived from DPD for $\Omega_0 = 5$ differ from the ones of LLNS. This demonstrates that the transition between different dynamic subregimes occurs gradually. An alternative way to look at the subregimes of DPD is to analyze the nondimensional effective shear viscosity.

Figure 3(a) presents a comparison of the nondimensional effective shear viscosity of DPD and LE. Every data point in Fig. 3(a) corresponds to the respective $C_\perp$ of DPD and is computed

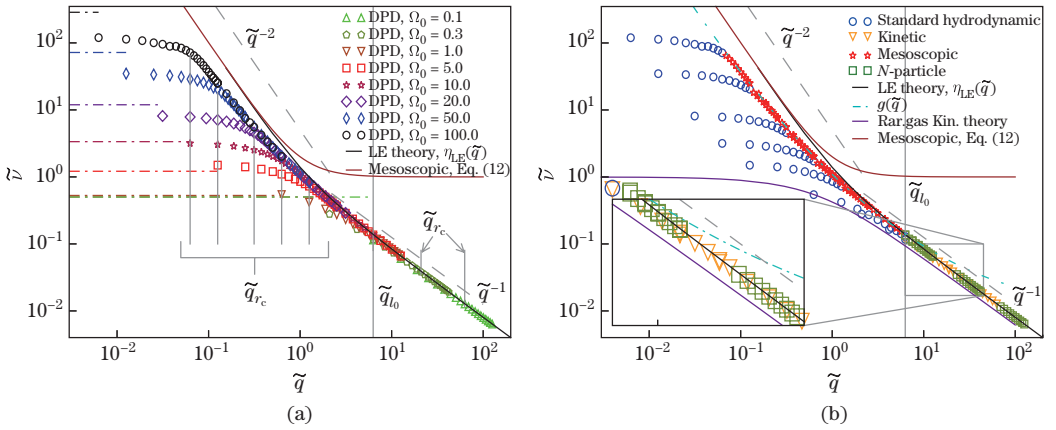

Fig. 3 Nondimensional effective shear viscosity $\widetilde{\nu}(\widetilde{q})$ estimated from DPD simulations and compared with nondimensional effective shear viscosity of LE (29). Brown line corresponds to the estimation (27) of scaling law for mesoscopic regime from Ref. [14]. In (a) DPD simulations with different Ω_0 are presented. Colored dash-dotted lines are the analytical estimates for the corresponding values of dynamic overlapping equation (25) from Ref. [14]. For all values of dynamic overlapping, the nondimensional kinematic viscosity collapses to the same law for wavenumbers larger than the cut-off wavenumber. In (b) different subregimes of DPD, see Table 1, are compared with the effective shear viscosity estimate for LE, Eq. (29), and the effective shear viscosity of rarefied gas Eq. (35). Colors correspond to those in Fig. 2 (Color online)

according to the definition of the effective shear viscosity in Eq. (28). One can observe that the dependency of the nondimensional effective shear viscosity $\widetilde{\nu}$ on $\widetilde{q}$ differs for different values of dynamic overlapping Ω_0. Nondimensional wavenumbers that correspond to the cut-off radius and decorrelation length are $\widetilde{q}_{r_c} = l_0 \frac{2\pi}{r_c}$ and $\widetilde{q}_{l_0} = 2\pi$, respectively. We choose the decorrelation length as length unit. For that reason, the nondimensional parameter $\widetilde{q}_{l_0}$ coincides for different values of Ω_0 in Fig. 3(a). However, $\widetilde{q}_{r_c}$ differs for different Ω_0. For wavenumbers larger than the cut-off wavenumber $\widetilde{q}_{r_c}$, the nondimensional effective shear viscosities for different Ω_0 follow the same universal trend. For the large wavenumbers $\widetilde{q} > \widetilde{q}_{l_0}$, the trend follows a $\widetilde{q}^{-1}$ scaling law and coincides with the LE effective shear viscosity. However, for small wavenumbers $\widetilde{q} < \widetilde{q}_{l_0}$, the trend differs from the LE effective shear viscosity and differs from the $\widetilde{q}^{-2}$ scaling law. Note that the $\widetilde{q}^{-1}$ scaling law corresponds to the ballistic regime of LE[44] and $\widetilde{q}^{-2}$ corresponds to the case where the CACFs of LE are exponential functions. The effective shear viscosities of DPD and LE are similar in the N-particle subregime and are different in the mesoscopic subregime. This fact deviates from the estimates for the mesoscopic and N-particle regimes given by Eq. (27), represented by a brown line in Fig. 3(a), previously derived in Ref. [14]. According to Eq. (27) in the N-particle subregime, the effective shear viscosity of DPD is constant, and in the mesoscopic subregime, it follows a $\widetilde{q}^{-2}$ scaling law. To improve the prediction given by Eq. (27), we approximate $\widetilde{\nu}(\widetilde{q})$ of DPD for the mesoscopic subregime empirically as

$$g(\widetilde{q}) = 1.09\widetilde{q}^{-1.3}\exp(0.1\log(\widetilde{q})^2). \tag{31}$$

An LE-based model was applied to rarefied gas flows in Refs. [30] and [45]. The Knudsen number is defined as the ratio of the mean free path to the length scale of interest $n_K := l_0/\lambda$. For high Knudsen numbers, length scales of interest are comparable to the mean free path of gas molecules. In the proposed model[30,45], Lagrangian particles are governed by a modified version of LE and the length scales of interest are comparable with the mean free path of Lagrangian particles. In Fig. 3(a), we demonstrate the similarity of the LE and DPD on the N-particle

subregime. However, it is also possible to compare $\widetilde{\nu}(\widetilde{q})$ of a rarefied gas with that of DPD. The velocity auto-correlation of a Brownian particle in gas is[46–47]

$$\langle v(0)v(t)\rangle = \frac{k_{\mathrm{B}}T}{M}\mathrm{e}^{-\Gamma_0 t}, \tag{32}$$

where the damping coefficient Γ_0 is

$$\Gamma_0 = \frac{6\pi\eta_{\mathrm{gas}}R}{m}\frac{0.619}{0.619+n_{\mathrm{K}}}(1+c_{\mathrm{K}}), \tag{33}$$

$$c_{\mathrm{K}} = \frac{0.31n_{\mathrm{K}}}{0.785+1.152n_{\mathrm{K}}+n_{\mathrm{K}}^2}. \tag{34}$$

An alternative way to represent the motion of a Brownian particle in gas is to consider that the effective viscosity depends on the Knudsen number

$$\widetilde{\nu}_{\mathrm{r.g.}} = \widetilde{\nu}_{\mathrm{gas}}\frac{0.619}{0.619+n_{\mathrm{K}}}(1+c_{\mathrm{K}}), \tag{35}$$

where $\widetilde{\nu}_{\mathrm{gas}}$ is the constant effective shear viscosity of the gas for $n_{\mathrm{K}} \ll 1$. Define the nondimensional wavenumber as $\widetilde{q} = 2\pi l_0/\lambda$ so that $\widetilde{q} = 2\pi n_{\mathrm{K}}$. We take $\widetilde{\nu}_{\mathrm{gas}} = 1$, without restricting the validity of the results in Fig. 3(b). Different colors in Fig. 3(b) correspond to different subregimes of DPD. The N-particle subregime (green lines) is in good agreement with the LE-theory (29). The kinetic subregime (yellow lines) deviates slightly from the LE theory. The mesoscopic subregime of DPD (red lines) exhibits a universal scaling range, which differs from the LE theory and is in good agreement with the empirical function $g(\widetilde{q})$ given by Eq. (31). For wavenumbers smaller than the cut-off wavenumber and the decorrelation-length wavenumber, we observe that DPD recovers the LLNS viscosity dependence which is characterized by the constant nondimensional effective shear viscosity (blue lines).

We conclude that the nondimensional effective shear viscosity of a rarefied gas and of DPD have common properties. For large wavenumbers, they follow the $\widetilde{q}^{\,-1}$ power law, corresponding to the N-particle subregime of DPD (green lines). In the limit of small wavenumbers, a plateau of the effective shear viscosity corresponds to the standard hydrodynamic subregime (blue lines). A smooth transition from N-particle to standard hydrodynamic subregime corresponds to the kinetic subregime of DPD (yellow lines).

5 Summary and discussions

In this paper, we review properties of the CACFs for two different systems, LLNS and LE. For these systems, expressions for CACFs can be derived analytically. The analytical solutions are well reproduced by numerical simulations for the CACFs of the LE.

The effective shear viscosity is defined through an integration of the transverse current auto-correlation function (28). This definition allows to introduce the effective shear viscosity for systems without momentum conservation, such as the LE. We determine the wavenumber dependence of the nondimensional effective shear viscosity of DPD without repulsive potential with the method introduced in a previous study[33].

The plateau exhibited by the DPD model is associated with macroscopic properties. For the standard hydrodynamic subregime, isothermal laws of motion in liquids and gases can be described with the LLNS equations, and the CACFs of DPD and LLNS are in good agreement, as was shown in Fig. 2 and in Ref. [33]. We show that the CACFs of the N-particle subregime of DPD and LE coincide. We also demonstrate that the effective shear viscosity of the DPD mesoscopic subregime differs from the LE effective shear viscosity. We introduce an empirical function $g(\widetilde{q})$ to match the dependency $\widetilde{\nu}(\widetilde{q})$ for the mesoscopic subregime of DPD.

We extend previous findings in Ref. [14] where it was suggested that the effective shear viscosity is constant both in the limit of large wavenumbers and small wavenumbers. For the range between small and large wavenumbers, it was estimated that the effective shear viscosity of DPD follows a $1 + q^{-2}$ scaling law. In the current paper, we confirm that on small wavenumbers, the effective viscosity is constant. However, for large wavenumbers, the effective viscosity exhibits a similar behavior as the effective viscosity for LEs (29), which corresponds to a q^{-1} scaling law. The correspondence of DPD and Langevin equations for this wavenumber range is also shown by comparison of the non-trivial form of CACFs of the LEs and of DPD. Moreover, we show that the $1 + q^{-2}$ scaling law can be improved by the introduction of the empirically derived (31). The difference from previous reports may be attributed to the fact that in such previous studies, e.g., Ref. [14], an exponential approximation for the transverse CACF was used. Note that in another previous study[33], it was shown that on small scales, the transverse CACF in DPD is not exponential.

The concept of DPD particle is loosely defined and lacks physical meaning[11]. Scales smaller than the cut-off radius are underresolved. However, in this work, we show that such scales exhibit a consistent dissipation law. We suggest that the small-scale behavior of DPD may be employed as an implicit fluid model, e.g., for high-Knudsen number flows. Properties of small, numerically underresolved scales are used for instance in turbulence modeling. For so-called implicit large-eddy simulation models, numerical dissipation on underresolved scales can be tuned to reproduce established energy-transfer mechanisms of turbulence[48–49].

We compare properties of Langevin and DPD thermostats. For that purpose, we consider DPD without conservative force. In principle, the effective shear viscosity can be measured for Kolmogorov flow[22]. The estimate from Kolmogorov flow coincides with the estimate of effective viscosity from CACF analysis[33]. However, for purely dissipative systems, such as the LE, it is challenging to set up Kolmogorov flow simulation, and a CACF analysis is preferable.

We use the analytical derivation of CACFs of a particle governed by the LEs. The same results are valid for a system of non-interacting particles governed by the LE. However, in the case of an additional force between the particles, e.g., due to a Lennard-Jones potential, the analytical expressions for CACFs are much more challenging to derive. In Fig. 1, it is shown that CACFs of LE can be accurately measured in simulations. For that reason, the analysis provided here can be extended to systems with repulsive potential. One can compare simulations of a Langevin thermostat with a certain interaction between particles against a DPD thermostat with the same interaction. From preliminary results, we can find that for large wavenumbers, such comparison reveals similar behavior of CACFs. Moreover, it is plausible that for DPD with a classical potential[4], the same scaling law as for DPD without potential will be observed.

Although we compare only the effective shear viscosity of DPD with that derived from the LE, an extension of the analysis for other macroscopic parameters, such as the effective isothermal speed of sound and the effective bulk viscosity, is straightforward. For this purpose, one needs to introduce a definition of effective bulk viscosity and effective isothermal speed of sound that is based on the longitudinal CACF. However, with any definition chosen, the isothermal speed of sound and the effective bulk viscosity of the N-particle subregime of DPD and LE would be similar due to the similarity of the longitudinal CACFs for both systems, which is presented in Figs. 2(d)–2(f). Another possibility is to extend the analysis to types of non-Markovian DPD (NM-DPD)[8]. The NM-DPD model on small scales can be compared with the colored noise LEs[50]. A comparison of the q-dependency of the effective shear viscosity of DPD with that of a rarefied gas reveals that DPD has the potential to model flows at high Knudsen number. For the correct representation of complex high Knudsen number flows, one needs to introduce a proper treatment for rarefied-gas wall boundaries in DPD. Practical rarefied gas modeling computations of DPD are beyond the scope of the current paper. We consider CACFs of DPD without the presence of mean shear. However, it is possible to extend the findings of the paper to the case of moderate shear rates following[36]. From the modeling perspective, the

presented analysis of DPD small scales extends the application of DPD to new problems, such as the modeling of turbulent phenomena on the mesoscale level or modeling of flows with high Knudsen number.

An extended consideration of current memory functions of the LE as well as DPD enables to use grid-based models for both systems. Numerical algorithms for the generalized Langevin model with repulsive potential were described in a previous study[51], where a repulsive potential was used for stability of the numerical algorithm and enters as a model parametrization. By tuning the form and the value of the repulsive potential and by using correlated form in time noise, current characteristics of grid-based models can be matched with Lagrangian ones.

Acknowledgements The first author acknowledges travel support from the Technical University of Munich (TUM) Graduate School. We thank the Munich Center of Advanced Computing for providing computational resources. We thank V. BOGDANOV for proofreading.

References

[1] Landau, L. D. and Lifshitz, E. M. *Fluid Mechanics*, 1st ed., Pergamon Press, Oxford (1959)

[2] Hoogerbrugge, P. J. and Koelman, J. M. V. A. Simulating microscopic hydrodynamic phenomena with dissipative particle dynamics. *Europhysics Letters*, **19**(3), 155–160 (1992)

[3] Español, P. and Warren, P. Statistical mechanics of dissipative particle dynamics. *Europhysics Letters*, **30**(4), 191–196 (1995)

[4] Groot, R. D. and Warren, P. B. Dissipative particle dynamics: bridging the gap between atomistic and mesoscopic simulation. *Journal of Chemical Physics*, **107**(11), 4423–4435 (1997)

[5] Pan, W., Caswell, B., and Karniadakis, G. E. Rheology, microstructure and migration in Brownian colloidal suspensions. *Langmuir*, **26**(1), 133–142 (2010)

[6] Fedosov, D. A., Caswell, B., and Karniadakis, G. E. A multiscale red blood cell model with accurate mechanics, rheology, and dynamics. *Biophysical Journal*, **98**(10), 2215–2225 (2010)

[7] Hijón, C., Español, P., Vanden-Eijnden, E., and Delgado-Buscalioni, R. Mori-Zwanzig formalism as a practical computational tool. *Faraday Discussions*, **144**, 301–322 (2010)

[8] Li, Z., Bian, X., Li, X., and Karniadakis, G. E. Incorporation of memory effects in coarse-grained modeling via the Mori-Zwanzig formalism. *Journal of Chemical Physics*, **143**(24), 243128 (2015)

[9] Mori, H. Transport, collective motion, and Brownian motion. *Progress of Theoretical Physics*, **33**(3), 423–455 (1965)

[10] Zwanzig, R. Ensemble method in the theory of irreversibility. *Journal of Chemical Physics*, **33**(5), 1338–1341 (1960)

[11] Español, P. and Warren, P. B. Perspective: dissipative particle dynamics. *Journal of Chemical Physics*, **146**(15), 150901 (2017)

[12] Marsh, C., Backx, G., and Ernst, M. H. Static and dynamic properties of dissipative particle dynamics. *Physical Review E*, **56**(2), 1676–1691 (1997)

[13] Marsh, C. *Theoretical Aspects of Dissipative Particle Dynamics*, Ph. D. dissertation, University of Oxford (1998)

[14] Ripoll, M., Ernst, M. H., and Español, P. Large scale and mesoscopic hydrodynamics for dissipative particle dynamics. *Journal of Chemical Physics*, **115**(15), 7271–7284 (2001)

[15] Español, P. and Revenga, M. Smoothed dissipative particle dynamics. *Physical Review E*, **67**(2), 026705 (2003)

[16] Lucy, L. B. A numerical approach to the testing of the fission hypothesis. *Astronomical Journal*, **82**, 1013–1024 (1977)

[17] Gingold, R. A. and Monaghan, J. J. Smoothed particle hydrodynamics: theory and application to non-spherical stars. *Monthly Notices of the Royal Astronomical Society*, **181**(3), 375–389 (1977)

[18] Öttinger, H. C. and Grmela, M. Dynamics and thermodynamics of complex fluids, II, illustrations of a general formalism. *Physical Review E*, **56**(6), 6633–6655 (1997)

[19] Henry, E., Holm, S. H., Zhang, Z., Beech, J. P., Tegenfeldt, J. O., Fedosov, D. A., and Gompper, G. Sorting cells by their dynamical properties. *Scientific Reports*, **6**, 34375 (2016)

[20] Bian, X., Litvinov, S., Qian, R., Ellero, M., and Adams, N. A. Multiscale modeling of particle in suspension with smoothed dissipative particle dynamics. *Physics of Fluids* (1994-*present*), **24**(1), 012002 (2012)

[21] Litvinov, S., Ellero, M., Hu, X., and Adams, N. A. Smoothed dissipative particle dynamics model for polymer molecules in suspension. *Physical Review E*, **77**(6), 066703 (2008)

[22] Vázquez-Quesada, A., Ellero, M., and Español, P. Smoothed particle hydrodynamic model for viscoelastic fluids with thermal fluctuations. *Physical Review E*, **79**(5), 056707 (2009)

[23] Kulkarni, P. M., Fu, C. C., Shell, M. S., and Leal, L. G. Multiscale modeling with smoothed dissipative particle dynamics. *Journal of Chemical Physics*, **138**(23), 234105 (2013)

[24] Lei, H., Mundy, C. J., Schenter, G. K., and Voulgarakis, N. K. Modeling nanoscale hydrodynamics by smoothed dissipative particle dynamics. *Journal of Chemical Physics*, **142**(19), 194504 (2015)

[25] Soddemann, T., Dünweg, B., and Kremer, K. Dissipative particle dynamics: a useful thermostat for equilibrium and nonequilibrium molecular dynamics simulations. *Physical Review E*, **68**(4), 046702 (2003)

[26] Yong, X. and Zhang, L. T. Thermostats and thermostat strategies for molecular dynamics simulations of nanofluidics. *Journal of Chemical Physics*, **138**(8), 084503 (2013)

[27] Junghans, C., Praprotnik, M., and Kremer, K. Transport properties controlled by a thermostat: an extended dissipative particle dynamics thermostat. *Physical Review E*, **4**(1), 156–161 (2007)

[28] Español, P. and Serrano, M. Dynamical regimes in the dissipative particle dynamics model. *Physical Review E*, **59**(6), 6340–6347 (1999)

[29] Haworth, D. C. and Pope, S. B. A generalized Langevin model for turbulent flows. *Physics of Fluids*, **29**(2), 387–405 (1986)

[30] Jenny, P., Torrilhon, M., and Heinz, S. A solution algorithm for the fluid dynamic equations based on a stochastic model for molecular motion. *Journal of Computational Physics*, **229**(4), 1077–1098 (2010)

[31] Boon, J. P. and Yip, S. *Molecular Hydrodynamics*, Dover Publications, New York (1992)

[32] Palmer, B. J. Transverse-current autocorrelation-function calculations of the shear viscosity for molecular liquids. *Physical Review E*, **49**(1), 359–366 (1994)

[33] Azarnykh, D., Litvinov, S., Bian, X., and Adams, N. A. Determination of macroscopic transport coefficients of a dissipative particle dynamics solvent. *Physical Review E*, **93**(1), 013302 (2016)

[34] De Fabritiis, G., Serrano, M., Delgado-Buscalioni, R., and Coveney, P. V. Fluctuating hydrodynamic modeling of fluids at the nanoscale. *Physical Review E*, **75**(2), 026307 (2007)

[35] Bell, J. B., Garcia, A. L., and Williams, S. A. Numerical methods for the stochastic Landau-Lifshitz Navier-Stokes equations. *Physical Review E*, **76**(1), 016708 (2007)

[36] Bian, X., Deng, M., Tang, Y. H., and Karniadakis, G. E. Analysis of hydrodynamic fluctuations in heterogeneous adjacent multidomains in shear flow. *Physical Review E*, **93**(3), 033312 (2016)

[37] Bian, X., Deng, M., and Karniadakis, G. E. Analytical and computational studies of correlations of hydrodynamic fluctuations in shear flow. *Computer Physics Communications*, **23**(1), 93–117 (2018)

[38] Huang, C. C., Gompper, G., and Winkler, R. G. Hydrodynamic correlations in multiparticle collision dynamics fluids. *Physical Review E*, **86**(5), 056711 (2012)

[39] Varghese, A., Huang, C. C., Winkler, R. G., and Gompper, G. Hydrodynamic correlations in shear flow: multiparticle-collision-dynamics simulation study. *Physical Review E*, **92**(5), 053002 (2015)

[40] Onsager, L. Reciprocal relations in irreversible processes, I. *Physical Review*, **37**(4), 405–426 (1931)

[41] Berne, B. J. and Pecora, R. *Dynamic Light Scattering*: *With Applications to Chemistry*, *Biology*, *and Physics*, Dover Publications, New York (2000)

[42] Langevin, P. Sur la théorie du mouvement brownien. *Comptes Rendus de l'Académie des Sciences* (*Paris*), **146**, 530–533 (1908)

[43] Chandrasekhar, S. Stochastic problems in physics and astronomy. *Reviews of Modern Physics*, **15**(1), 1–89 (1943)

[44] Bian, X., Kim, C., and Karniadakis, G. E. 111 years of Brownian motion. *Soft Matter*, **12**(30), 6331–6346 (2016)

[45] Gorji, M. H., Torrilhon, M., and Jenny, P. Fokker-Planck model for computational studies of monatomic rarefied gas flows. *Journal of Fluid Mechanics*, **680**, 574–601 (2011)

[46] Beresnev, S. A., Chernyak, V. G., and Fomyagin, G. A. Motion of a spherical particle in a rarefied gas, part 2, drag and thermal polarization. *Journal of Fluid Mechanics*, **219**, 405–421 (1990)

[47] Li, T. and Raizen, M. G. Brownian motion at short time scales. *Annalen der Physik*, **525**(4), 281–295 (2013)

[48] Hickel, S., Adams, N. A., and Domaradzki, J. A. An adaptive local deconvolution method for implicit LES. *Journal of Computational Physics*, **213**(1), 413–436 (2006)

[49] Schranner, F. S., Hu, X., and Adams, N. A. A physically consistent weakly compressible high-resolution approach to underresolved simulations of incompressible flows. *Computers and Fluids*, **86**, 109–124 (2013)

[50] Wang, P., Tartakovsky, A. M., and Tartakovsky, D. M. Probability density function method for Langevin equations with colored noise. *Physical Review Letters*, **110**(14), 140602 (2013)

[51] Azarnykh, D., Litvinov, S., and Adams, N. A. Numerical methods for the weakly compressible generalized Langevin model in Eulerian reference frame. *Journal of Computational Physics*, **314**, 93–106 (2016)

[52] McLennan, J. A. Correlation functions for dilute systems. *Physics of Fluids* (1958-1988), **9**(8), 1581–1589 (1966)

Appendix A

The LEs are characterized by the velocity auto-correlation function and the mean-squared displacement (MSD)[44,47]

$$C_{\mathrm{LE}v}(t) = \frac{\langle v(0)v(t)\rangle}{\langle v(0)v(0)\rangle} = \mathrm{e}^{-\beta t}\ , \tag{A1}$$

$$C_{\mathrm{LE}x}(t) = \langle \Delta x^2(t)\rangle = \frac{2k_{\mathrm{B}}T}{\beta^2 m}(\beta t - 1 + \mathrm{e}^{-\beta t}). \tag{A2}$$

Another general way to describe the properties of the LE is through its conditional joint probability distribution function (PDF) $P(\boldsymbol{v}, \boldsymbol{x}, t|\boldsymbol{v_0})$, which is the probability of the particle with the initial velocity $\boldsymbol{v}(t = 0, \boldsymbol{x} = \boldsymbol{0}) = \boldsymbol{v_0}$ and location $\boldsymbol{x_0}$ to be at time t in $\boldsymbol{x}$ with velocity $\boldsymbol{v}$. The expression for the conditional joint-PDF for the LEs in d-dimensions is[43]

$$P(\boldsymbol{v}, \boldsymbol{x}, t|\boldsymbol{v_0}) = Z_p \exp\Big(- \frac{A\boldsymbol{V}\cdot\boldsymbol{V} + 2C\boldsymbol{V}\cdot\boldsymbol{X} + B\boldsymbol{X}\cdot\boldsymbol{X}}{2(AB - C^2)}\Big), \tag{A3}$$

$$Z_p = \frac{\mathrm{e}^{\beta t d}}{(2\pi)^d (AB - C^2)^{\frac{d}{2}}}, \tag{A4}$$

$$\boldsymbol{V} = \mathrm{e}^{\beta t}\boldsymbol{v} - \boldsymbol{v_0}, \quad \boldsymbol{X} = \boldsymbol{x} + \boldsymbol{u}/\beta - \boldsymbol{x_0} - \boldsymbol{v_0}/\beta, \tag{A5}$$

$$A = 2\frac{k_{\mathrm{B}}T}{m}\beta^{-2}t, \quad B = \frac{k_{\mathrm{B}}T}{m}\beta^{-1}(\mathrm{e}^{2\beta t} - 1), \quad C = -2\frac{k_{\mathrm{B}}T}{m}\beta^{-2}(\mathrm{e}^{\beta t} - 1). \tag{A6}$$

As the LE is an isotropic model, it is sufficient to consider only one direction. The corresponding equations for other directions are equivalent. The marginal PDF results by definition from integration of the joint-PDF,

$$P_x(x, t|v_{x0}) = \int_{-\infty}^{\infty} P(v_x, x, t|v_{x0})\mathrm{d}v,$$

$$P_v(v_x, t|v_{x0}) = \int_{-\infty}^{\infty} P(v_x, x, t|v_{x0})\mathrm{d}x.$$

The one-dimensional Maxwell-Boltzmann distribution results as equilibrium PDF,

$$\begin{cases} G(v_x) = \lim_{t\to\infty} P_v(v_x, t|v_{x0}), \\ G(v_x) = \sqrt{2\pi\dfrac{k_\mathrm{B}T}{m}}\exp\Big(-\dfrac{m}{2_\mathrm{B}T}v_x^2\Big). \end{cases} \tag{A7}$$

We further derive the analytical expressions for the transverse CACF, longitudinal CACF, and density auto-correlation functions, respectively, as

$$\begin{cases} C_{\mathrm{LE}\perp} = \dfrac{1}{\widehat{w}(0)^2}\displaystyle\int_{-\infty}^{\infty} v_{x0}v_x \mathrm{e}^{\mathrm{i}qy_0}\mathrm{e}^{\mathrm{i}qy} \times P(v_x, y, t|v_{x0})G(v_{x0})\mathrm{d}v_x\mathrm{d}v_{x0}\mathrm{d}y, \\ C_{\mathrm{LE}\parallel} = \dfrac{1}{\widehat{w}(0)^2}\displaystyle\int_{-\infty}^{\infty} v_{x0}v_x \mathrm{e}^{\mathrm{i}qx_0}\mathrm{e}^{\mathrm{i}qx} \times P(v_x, x, t|v_{x0})G(v_{x0})\mathrm{d}v_x\mathrm{d}v_{x0}\mathrm{d}x, \end{cases} \tag{A8}$$

$$C_{\mathrm{LE}\rho} = \frac{1}{\widehat{\rho}(0)^2}\int_{-\infty}^{\infty} \mathrm{e}^{\mathrm{i}qy_0}\mathrm{e}^{\mathrm{i}qy}P_y(y, t|v_{y0})G(v_{y0})\mathrm{d}y\mathrm{d}v_{y0}. \tag{A9}$$

After integration, we obtain Eqs. (19)–(21),

$$C_{\mathrm{LE}\perp} = \exp(-\beta t) \times \exp\Big(-\frac{q^2k_\mathrm{B}T}{\beta^2 m}(\beta t - 1 + \mathrm{e}^{-\beta t})\Big),$$

$$C_{\mathrm{LE}\parallel} = \Big(\mathrm{e}^{\beta t} - q^2\Big(\frac{k_\mathrm{B}T}{\beta^2 m}\Big)(\mathrm{e}^{\beta t} - 1)^2\Big) \times \exp(-2\beta t)\exp\Big(-\frac{q^2k_\mathrm{B}T}{\beta^2 m}(\beta t - 1 + \mathrm{e}^{-\beta t})\Big),$$

$$C_{\mathrm{LE}\rho} = \exp\Big(-\frac{q^2k_\mathrm{B}T}{\beta^2 m}(\beta t - 1 + \mathrm{e}^{-\beta t})\Big).$$

To our knowledge, Eqs. (19)–(21) have not been explicitly stated before, although the Laplace-Fourier transformed version of Eqs. (19)–(21) were provided in Ref. [52].

Note that the first factor of Eq. (19) on the right originates from the exponential auto-correlation of Lagrangian particle velocity, Eq. (A1). The other factor originates from the diffusion of the particles in space, Eq. (A2), and coincides with the density auto-correlation function $C_{\mathrm{LE}\rho}$.

B. Bibliography

[1] L. D. Landau and E. M. Lifshitz. *Fluid Mechanics*. Pergamon Press, Oxford, 1st edition, 1959.

[2] G. K. Batchelor. *An Introduction to Fluid Dynamics*. Cambridge University Press, February 2000.

[3] B. J. Alder and T. E. Wainwright. Studies in Molecular Dynamics. I. General Method. *The Journal of Chemical Physics*, 31(2):459–466, August 1959.

[4] M. P. Allen and D. J. Tildesley. *Computer Simulation of Liquids*. Clarendon Press, Oxford England; New York, revised ed. edition edition, June 1989.

[5] P. Langevin. Sur la théorie du mouvement brownien. *C. R. Acad. Sci. (Paris)*, 146:530–533, 1908.

[6] R. Kubo. The fluctuation-dissipation theorem. *Reports on Progress in Physics*, 29(1):255, 1966.

[7] S. B. Pope. A Lagrangian two-time probability density function equation for inhomogeneous turbulent flows. *Physics of Fluids*, 26(12):3448–3450, December 1983.

[8] S.B. Pope. PDF methods for turbulent reactive flows. *Progress in Energy and Combustion Science*, 11(2):119–192, 1985.

[9] D. C. Haworth and S. B. Pope. A generalized Langevin model for turbulent flows. *Physics of Fluids*, 29(2):387–405, February 1986.

[10] M. Griebel, T. Dornsheifer, and T. Neunhoeffer. *Numerical Simulation in Fluid Dynamics: A Practical Introduction*. SIAM: Society for Industrial and Applied Mathematics, Philadelphia, December 1997.

[11] J. Anderson. *Computational Fluid Dynamics*. McGraw-Hill Education, New York, 1 edition edition, February 1995.

[12] G. A. Bird. Approach to Translational Equilibrium in a Rigid Sphere Gas. *Physics of Fluids (1958-1988)*, 6(10):1518–1519, October 1963.

[13] G. A. Bird. Monte Carlo Simulation of Gas Flows. *Annual Review of Fluid Mechanics*, 10(1):11–31, 1978.

[14] G. A. Bird. *Molecular Gas Dynamics and the Direct Simulation of Gas Flows*. Oxford Engineering Science Series. Oxford University Press, USA, 2nd edition, 1994.

[15] M. Serrano and P. Español. Thermodynamically consistent mesoscopic fluid particle model. *Physical Review E*, 64(4):046115, September 2001.

[16] P. Español and M. Revenga. Smoothed dissipative particle dynamics. *Physical Review E*, 67(2):026705, February 2003.

[17] P. J. Hoogerbrugge and J. M. V. A. Koelman. Simulating Microscopic Hydrodynamic Phenomena with Dissipative Particle Dynamics. *EPL (Europhysics Letters)*, 19(3):155, June 1992.

[18] P. Español and P. Warren. Statistical Mechanics of Dissipative Particle Dynamics. *EPL (Europhysics Letters)*, 30(4):191, May 1995.

[19] R. D. Groot and P. B. Warren. Dissipative particle dynamics: Bridging the gap between atomistic and mesoscopic simulation. *The Journal of Chemical Physics*, 107(11):4423–4435, September 1997.

[20] M. Bixon and R. Zwanzig. Boltzmann-Langevin Equation and Hydrodynamic Fluctuations. *Physical Review*, 187(1):267–272, November 1969.

[21] R. F. Fox and G. E. Uhlenbeck. Contributions to Non-Equilibrium Thermodynamics. I. Theory of Hydrodynamical Fluctuations. *Physics of Fluids*, 13(8):1893–1902, August 1970.

[22] G. E. Kelly and M. B. Lewis. Hydrodynamic Fluctuations. *Physics of Fluids (1958-1988)*, 14(9):1925–1931, September 1971.

[23] P. Español. Stochastic differential equations for non-linear hydrodynamics. *Physica A: Statistical Mechanics and its Applications*, 248(1):77–96, January 1998.

[24] M. M. Mansour, A. L. Garcia, G. C. Lie, and E. Clementi. Fluctuating hydrodynamics in a dilute gas. *Physical Review Letters*, 58(9):874–877, March 1987.

[25] M. Mareschal, E. Kestemont, F. Baras, E. Clementi, and G. Nicolis. Nonequilibrium states by molecular dynamics: Transport coefficients in constrained fluids. *Physical Review A*, 35(9):3883–3893, May 1987.

[26] A. García and C. Penland. Fluctuating hydrodynamics and principal oscillation pattern analysis. *Journal of Statistical Physics*, 64(5-6):1121–1132, September 1991.

[27] M. Moseler and U. Landman. Formation, Stability, and Breakup of Nanojets. *Science*, 289(5482):1165–1169, August 2000.

[28] J. Eggers. Dynamics of Liquid Nanojets. *Physical Review Letters*, 89(8):084502, August 2002.

[29] W. Kang and U. Landman. Universality Crossover of the Pinch-Off Shape Profiles of Collapsing Liquid Nanobridges in Vacuum and Gaseous Environments. *Physical Review Letters*, 98(6):064504, February 2007.

[30] G. De Fabritiis, M. Serrano, R. Delgado-Buscalioni, and P. V. Coveney. Fluctuating hydrodynamic modeling of fluids at the nanoscale. *Physical Review E*, 75(2):026307, February 2007.

[31] J. B. Bell, A. L. Garcia, and S. A. Williams. Numerical methods for the stochastic Landau-Lifshitz Navier-Stokes equations. *Physical Review E*, 76(1):016708, 2007.

[32] A. Vailati and M. Giglio. Giant fluctuations in a free diffusion process. *Nature*, 390(6657):262–265, November 1997.

[33] A. Vailati, R. Cerbino, S. Mazzoni, C. J. Takacs, D. S. Cannell, and M. Giglio. Fractal fronts of diffusion in microgravity. *Nature Communications*, 2:290, April 2011.

[34] A. Donev, J. B. Bell, A. de la Fuente, and A. L. Garcia. Diffusive Transport by Thermal Velocity Fluctuations. *Physical Review Letters*, 106(20):204501, May 2011.

[35] A. Donev, J. Bell, A. Garcia, and B. Alder. A Hybrid Particle-Continuum Method for Hydrodynamics of Complex Fluids. *Multiscale Modeling & Simulation*, 8(3):871–911, January 2010.

[36] A. Donev, A. Nonaka, A. K. Bhattacharjee, A. L. Garcia, and J. B. Bell. Low Mach number fluctuating hydrodynamics of multispecies liquid mixtures. *Physics of Fluids (1994-present)*, 27(3):037103, March 2015.

[37] P. Plunkett, J. Hu, C. Siefert, and P. J. Atzberger. Spatially adaptive stochastic methods for fluid–structure interactions subject to thermal fluctuations in domains with complex geometries. *Journal of Computational Physics*, 277:121–137, November 2014.

[38] L. B. Lucy. A numerical approach to the testing of the fission hypothesis. *Astronomical Journal*, 82:1013–1024, December 1977.

[39] R. A. Gingold and J. J. Monaghan. Smoothed particle hydrodynamics: theory and application to non-spherical stars. *Monthly Notices of the Royal Astronomical Society*, 181(3):375–389, December 1977.

[40] J.J. Monaghan. Smoothed Particle Hydrodynamics and Its Diverse Applications. *Annual Review of Fluid Mechanics*, 44(1):323–346, 2012.

[41] M. Grmela and H. C. Öttinger. Dynamics and thermodynamics of complex fluids. I. Development of a general formalism. *Physical Review E*, 56(6):6620–6632, December 1997.

[42] H. C. Öttinger and M. Grmela. Dynamics and thermodynamics of complex fluids. II. Illustrations of a general formalism. *Physical Review E*, 56(6):6633–6655, December 1997.

[43] P. Español, M. Serrano, and H. C. Öttinger. Thermodynamically Admissible Form for Discrete Hydrodynamics. *Physical Review Letters*, 83(22):4542–4545, November 1999.

[44] J. Kordilla, W. Pan, and A. Tartakovsky. Smoothed particle hydrodynamics model for Landau-Lifshitz-Navier-Stokes and advection-diffusion equations. *The Journal of Chemical Physics*, 141(22):224112, December 2014.

[45] S. Litvinov, M. Ellero, X. Hu, and N. A. Adams. Smoothed dissipative particle dynamics model for polymer molecules in suspension. *Physical Review E*, 77(6):066703, June 2008.

[46] S. Litvinov, M. Ellero, X. Hu, and N. A. Adams. Self-diffusion coefficient in smoothed dissipative particle dynamics. *The Journal of Chemical Physics*, 130(2):021101, January 2009.

[47] S. Litvinov, X. Hu, M. Ellero, and N. A. Adams. Mesoscopic simulation of the transient behavior of semi-diluted polymer solution in a microchannel following extensional flow. *Microfluidics and Nanofluidics*, 16(1-2):257–264, May 2013.

[48] S. Litvinov, Q. Xie, X. Hu, N. Adams, and M. Ellero. Simulation of Individual Polymer Chains and Polymer Solutions with Smoothed Dissipative Particle Dynamics. *Fluids*, 1(1):7, February 2016.

[49] S. Litvinov. *Mesoscopic simulation of DNA using Smoothed Dissipative Particle Dynamics*. Ph.D. thesis, Technical University of Munich, Munich, 2014.

[50] X. Bian, S. Litvinov, R. Qian, M. Ellero, and N. A. Adams. Multiscale modeling of particle in suspension with smoothed dissipative particle dynamics. *Physics of Fluids (1994-present)*, 24(1):012002, January 2012.

[51] X. Bian, S. Litvinov, M. Ellero, and N. J. Wagner. Hydrodynamic shear thickening of particulate suspension under confinement. *Journal of Non-Newtonian Fluid Mechanics*, 213:39–49, November 2014.

[52] X. Bian. *Modeling and simulation of particle dispersions with smoothed dissipative particle dynamics*. Ph.D. thesis, Technical University of Munich, Munich, 2015.

[53] D. A. Fedosov, M. Dao, G. E. Karniadakis, and S. Suresh. Computational Biorheology of Human Blood Flow in Health and Disease. *Annals of Biomedical Engineering*, 42(2):368–387, October 2013.

[54] D. A. Fedosov, M. Peltomäki, and G. Gompper. Deformation and dynamics of red blood cells in flow through cylindrical microchannels. *Soft Matter*, 10(24):4258–4267, 2014.

[55] K. Müller, D. A. Fedosov, and G. Gompper. Margination of micro- and nano-particles in blood flow and its effect on drug delivery. *Scientific Reports*, 4, May 2014.

[56] E. Henry, S. H. Holm, Z. Zhang, J. P. Beech, J. O. Tegenfeldt, D. A. Fedosov, and G. Gompper. Sorting cells by their dynamical properties. *Scientific Reports*, 6:34375, October 2016.

[57] A. J. C. Ladd. Short-time motion of colloidal particles: Numerical simulation via a fluctuating lattice-Boltzmann equation. *Physical Review Letters*, 70(9):1339–1342, March 1993.

[58] S. Chen and G. D. Doolen. Lattice Boltzmann Method for Fluid Flows. *Annual Review of Fluid Mechanics*, 30(1):329–364, 1998.

[59] P. L. Bhatnagar, E. P. Gross, and M. Krook. A Model for Collision Processes in Gases. I. Small Amplitude Processes in Charged and Neutral One-Component Systems. *Physical Review*, 94(3):511–525, May 1954.

[60] S. Succi. *The Lattice Boltzmann Equation for Fluid Dynamics and Beyond*. Clarendon Press, Oxford : New York, 1 edition edition, August 2001.

[61] N.-Q. Nguyen and A. J. C. Ladd. Lubrication corrections for lattice-Boltzmann simulations of particle suspensions. *Physical Review E*, 66(4):046708, October 2002.

[62] G. R. McNamara, A. L. Garcia, and B. J. Alder. A hydrodynamically correct thermal lattice Boltzmann model. *Journal of Statistical Physics*, 87(5-6):1111–1121, June 1997.

[63] X. Shan. Simulation of Rayleigh-Bénard convection using a lattice Boltzmann method. *Physical Review E*, 55(3):2780–2788, March 1997.

[64] X. He, S. Chen, and G. D. Doolen. A Novel Thermal Model for the Lattice Boltzmann Method in Incompressible Limit. *Journal of Computational Physics*, 146(1):282–300, October 1998.

[65] A. J. C. Ladd. Numerical simulations of particulate suspensions via a discretized Boltzmann equation. Part 2. Numerical results. *Journal of Fluid Mechanics*, 271:311–339, July 1994.

[66] A. J. C. Ladd. Numerical simulations of particulate suspensions via a discretized Boltzmann equation. Part 1. Theoretical foundation. *Journal of Fluid Mechanics*, 271:285–309, July 1994.

[67] A. J. C. Ladd and R. Verberg. Lattice-Boltzmann Simulations of Particle-Fluid Suspensions. *Journal of Statistical Physics*, 104(5-6):1191–1251, September 2001.

[68] W. Pan, B. Caswell, and G. E. Karniadakis. Rheology, Microstructure and Migration in Brownian Colloidal Suspensions. *Langmuir*, 26(1):133–142, January 2010.

[69] D. A. Fedosov, B. Caswell, and G. E. Karniadakis. A Multiscale Red Blood Cell Model with Accurate Mechanics, Rheology, and Dynamics. *Biophysical Journal*, 98(10):2215–2225, May 2010.

[70] M. Ripoll, M. H. Ernst, and P. Español. Large scale and mesoscopic hydrodynamics for dissipative particle dynamics. *The Journal of Chemical Physics*, 115(15):7271–7284, October 2001.

[71] C. Marsh. *Theoretical Aspects of Dissipative Particle Dynamics*. Ph.D. thesis, University of Oxford, 1998.

[72] C. Marsh, G. Backx, and M. H. Ernst. Static and Dynamic Properties of Dissipative Particle Dynamics. *Physical Review E*, 56(2):1676–1691, August 1997.

[73] C. A Marsh, G Backx, and M. H Ernst. Fokker-Planck-Boltzmann equation for dissipative particle dynamics. *Europhysics Letters (EPL)*, 38(6):411–416, May 1997.

[74] H. Mori. Transport, Collective Motion, and Brownian Motion. *Progress of Theoretical Physics*, 33(3):423–455, March 1965.

[75] R. Zwanzig. Ensemble Method in the Theory of Irreversibility. *J. Chem. Phys.*, 33(5):1338–1341, 1960.

[76] R. Zwanzig. *Nonequilibrium Statistical Mechanics*. Oxford University Press, Oxford; New York, 1 edition edition, April 2001.

[77] Z. Li, X. Bian, X. Li, and G. E. Karniadakis. Incorporation of memory effects in coarse-grained modeling via the Mori-Zwanzig formalism. *The Journal of Chemical Physics*, 143(24):243128, December 2015.

[78] Z. Li, Y.-H. Tang, H. Lei, B. Caswell, and G. E. Karniadakis. Energy-conserving dissipative particle dynamics with temperature-dependent properties. *Journal of Computational Physics*, 265:113–127, May 2014.

[79] Z. Li, X. Bian, B. Caswell, and G. E. Karniadakis. Construction of dissipative particle dynamics models for complex fluids via the Mori–Zwanzig formulation. *Soft Matter*, 10(43):8659–8672, October 2014.

[80] P. Español, M. Serrano, I. Pagonabarraga, and I. Zúñiga. Energy-conserving coarse-graining of complex molecules. *Soft Matter*, April 2016.

[81] A. Malevanets and R. Kapral. Mesoscopic model for solvent dynamics. *The Journal of Chemical Physics*, 110(17):8605–8613, May 1999.

[82] T. Ihle and D. M. Kroll. Stochastic rotation dynamics: a Galilean-invariant mesoscopic model for fluid flow. *Physical Review. E, Statistical, Nonlinear, and Soft Matter Physics*, 63(2 Pt 1):020201, February 2001.

[83] T. Ihle and D. M. Kroll. Stochastic rotation dynamics. I. Formalism, Galilean invariance, and Green-Kubo relations. *Physical Review E*, 67(6):066705, June 2003.

[84] T. Ihle and D. M. Kroll. Stochastic rotation dynamics. II. Transport coefficients, numerics, and long-time tails. *Physical Review E*, 67(6):066706, June 2003.

[85] A. D. Fokker. Die mittlere Energie rotierender elektrischer Dipole im Strahlungsfeld. *Annalen der Physik*, 348(5):810–820, January 1914.

[86] M. Planck. *Über einen Satz der statistischen Dynamik und seine Erweiterung in der Quantentheorie*. De Gruyter, 1917.

[87] G. E. Uhlenbeck and L. S. Ornstein. On the Theory of the Brownian Motion. *Physical Review*, 36(5):823–841, September 1930.

[88] S. Chandrasekhar. Stochastic Problems in Physics and Astronomy. *Reviews of Modern Physics*, 15(1):1–89, January 1943.

[89] W. T. Coffey, Y. P. Kalmykov, and J. T. Waldron. *The Langevin Equation: With Applications to Stochastic Problems in Physics, Chemistry and Electrical Engineering (World Scientific Series in Contemporary Chemical Physics Vol. 14) - Second Edition*. World Scientific Publishing Company, River Edge, NJ, 2nd revised ed. edition edition, March 2004.

[90] X. Bian, C. Kim, and G. E. Karniadakis. 111 years of Brownian motion. *Soft Matter*, 12(30):6331–6346, July 2016.

[91] Tongcang Li and Mark G. Raizen. Brownian motion at short time scales. *Annalen der Physik*, 525(4):281–295, April 2013.

[92] D. L. Ermak and J. A. McCammon. Brownian dynamics with hydrodynamic interactions. *The Journal of Chemical Physics*, 69(4):1352–1360, August 1978.

[93] T. Soddemann, B. Dünweg, and K. Kremer. Dissipative particle dynamics: A useful thermostat for equilibrium and nonequilibrium molecular dynamics simulations. *Physical Review E*, 68(4):046702, October 2003.

[94] X. Yong and L. T. Zhang. Thermostats and thermostat strategies for molecular dynamics simulations of nanofluidics. *The Journal of Chemical Physics*, 138(8):084503, February 2013.

[95] D. C. Haworth. Progress in probability density function methods for turbulent reacting flows. *Progress in Energy and Combustion Science*, 36(2):168–259, April 2010.

[96] J.-P. Minier. Statistical descriptions of polydisperse turbulent two-phase flows. *Physics Reports*, 2016.

[97] S. B. Pope. *Turbulent Flows*. Cambridge University Press, August 2000.

[98] J. P. Boon and S. Yip. *Molecular Hydrodynamics*. Dover Publications, January 1992.

[99] B. J. Berne and R. Pecora. *Dynamic Light Scattering: With Applications to Chemistry, Biology, and Physics*. Dover Publications, unabridged edition, August 2000.

[100] B. J. Berne and G. D. Harp. On the Calculation of Time Correlation Functions. In I. Prigogine and Stuart A. Rice, editors, *Advances in Chemical Physics*, pages 63–227. John Wiley & Sons, Inc., 2007.

[101] F. Balboa, J. B. Bell, R. Delgado-Buscalioni, A. Donev, T. G. Fai, B. E. Griffith, and C. S. Peskin. Staggered Schemes for Fluctuating Hydrodynamics. *Multiscale Modeling & Simulation*, 10(4):1369–1408, November 2012.

[102] D. Azarnykh, S. Litvinov, and N. A. Adams. Numerical methods for the weakly compressible Generalized Langevin Model in Eulerian reference frame. *Journal of Computational Physics*, 314:93–106, June 2016.

[103] B. J. Palmer. Transverse-current autocorrelation-function calculations of the shear viscosity for molecular liquids. *Physical Review E*, 49(1):359–366, January 1994.

[104] C.-C. Huang, G. Gompper, and R. G. Winkler. Hydrodynamic correlations in multiparticle collision dynamics fluids. *Physical Review E*, 86(5):056711, November 2012.

[105] A. Varghese, C.-C. Huang, R. G. Winkler, and G. Gompper. Hydrodynamic correlations in shear flow: Multiparticle-collision-dynamics simulation study. *Physical Review E*, 92(5):053002, November 2015.

[106] D. Azarnykh, S. Litvinov, X. Bian, and N. A. Adams. Determination of macroscopic transport coefficients of a dissipative particle dynamics solvent. *Physical Review E*, 93(1):013302, January 2016.

[107] A. Donev, E. Vanden-Eijnden, A. Garcia, and J. B. Bell. On the accuracy of finite-volume schemes for fluctuating hydrodynamics. *Communications in Applied Mathematics and Computational Science*, 5(2):149–197, June 2010.

[108] C. Gardiner. *Stochastic Methods: A Handbook for the Natural and Social Sciences*. Springer, Berlin, softcover reprint of hardcover 4th ed. 2009 edition edition, November 2010.

[109] H. C. Öttinger. *Stochastic Processes in Polymeric Fluids: Tools and Examples for Developing Simulation Algorithms*. Springer, Berlin ; New York, softcover reprint of the original 1st ed. 1996 edition edition, October 2013.

[110] L. Arnold. *Stochastic Differential Equations: Theory and Applications*. Krieger Pub Co, Malabar, Fla, May 1992.

[111] B. Øksendal. *Stochastic Differential Equations: An Introduction with Applications*. Springer, Berlin ; New York, 6th edition edition, September 2010.

[112] F. C. Klebaner. *Introduction to Stochastic Calculus with Applications*. Imperial College Press, London ; Hackensack, N.J, 2 edition edition, June 2005.

[113] J.-P. Minier and E. Peirano. The pdf approach to turbulent polydispersed two-phase flows. *Physics Reports*, 352(1–3):1–214, October 2001.

[114] L. Verlet. Computer "Experiments" on Classical Fluids. I. Thermodynamical Properties of Lennard-Jones Molecules. *Physical Review*, 159(1):98–103, July 1967.

[115] W. C. Swope, H. C. Andersen, P. H. Berens, and K. R. Wilson. A computer simulation method for the calculation of equilibrium constants for the formation of physical clusters of molecules: Application to small water clusters. *The Journal of Chemical Physics*, 76(1):637–649, January 1982.

[116] S. Gottlieb and C. W. Shu. Total variation diminishing Runge-Kutta schemes. *Mathematics of Computation*, 67(221):73–85, January 1998.

[117] J. X. Qiu and C. W. Shu. Runge-Kutta discontinuous Galerkin method using WENO limiters. *Siam Journal on Scientific Computing*, 26(3):907–929, 2005.

[118] S. Delong, B. E. Griffith, E. Vanden-Eijnden, and A. Donev. Temporal integrators for fluctuating hydrodynamics. *Physical Review E*, 87(3):033302, March 2013.

[119] N. K. Voulgarakis and J.-W. Chu. Bridging fluctuating hydrodynamics and molecular dynamics simulations of fluids. *The Journal of Chemical Physics*, 130(13):134111, April 2009.

[120] Y. Morinishi. Skew-symmetric form of convective terms and fully conservative finite difference schemes for variable density low-Mach number flows. *Journal of Computational Physics*, 229(2):276–300, January 2010.

[121] F. U. Balboa. *Minimal models for finite particles in fluctuating hydrodynamics*. Ph.D. thesis, Autonomous University of Madrid, February 2014.

[122] J. A. de la Torre, P. Español, and A. Donev. Finite element discretization of non-linear diffusion equations with thermal fluctuations. *The Journal of Chemical Physics*, 142(9):094115, mar 2015.

[123] W. Dehnen and H. Aly. Improving convergence in smoothed particle hydrodynamics simulations without pairing instability. *Monthly Notices of the Royal Astronomical Society*, 425(2):1068–1082, September 2012.

[124] S. Litvinov, M. Ellero, X. Y. Hu, and N. A. Adams. A Splitting Scheme for Highly Dissipative Smoothed Particle Dynamics. *J. Comput. Phys.*, 229(15):5457–5464, August 2010.

[125] X. Bian and M. Ellero. A splitting integration scheme for the SPH simulation of concentrated particle suspensions. *Computer Physics Communications*, 185(1):53–62, January 2014.

[126] P. Jenny, M. Torrilhon, and S. Heinz. A solution algorithm for the fluid dynamic equations based on a stochastic model for molecular motion. *Journal of Computational Physics*, 229(4):1077–1098, February 2010.

[127] M. H. Gorji, M. Torrilhon, and P. Jenny. Fokker–Planck model for computational studies of monatomic rarefied gas flows. *Journal of Fluid Mechanics*, 680:574–601, August 2011.

[128] J. A. McLennan. Correlation Functions for Dilute Systems. *Physics of Fluids (1958-1988)*, 9(8):1581–1589, August 1966.

[129] P. E. Kloeden and E. Platen. *Numerical Solution of Stochastic Differential Equations*. Springer, Berlin ; New York, corrected edition edition, August 1992.

[130] V. Sabel'nikov and O. Soulard. Rapidly decorrelating velocity-field model as a tool for solving one-point Fokker-Planck equations for probability density functions of turbulent reactive scalars. *Physical Review E*, 72(1):016301, July 2005.

[131] O. Soulard and V. A. Sabel'nikov. Eulerian Monte Carlo method for the joint velocity and mass-fraction probability density function in turbulent reactive gas flows. *Combustion, Explosion and Shock Waves*, 42(6):753–762, November 2006.

[132] N. A. Adams. A stochastic extension of the approximate deconvolution model. *Physics of Fluids*, 23(5):055103, 2011.

[133] N. Petrova. *Turbulence-chemistry interaction models for numerical simulation of aeronautical propulsion systems*. Ph.D. thesis, Ecole polytechnique X, January 2015.

[134] V. Sabel'nikov and O. Soulard. Eulerian (Field) Monte Carlo Methods for Solving PDF Transport Equations in Turbulent Reacting Flows. In *Handbook of Combustion*. Wiley-VCH Verlag GmbH & Co. KGaA, 2010.

[135] C. Emako, V. Letizia, N. Petrova, R. Sainct, R. Duclous, and O. Soulard. Diffusion limit of the simplified Langevin PDF model in weakly inhomogeneous turbulence. *ESAIM: Proceedings and Surveys*, 48:400–419, January 2015.

[136] D. Azarnykh, S. Litvinov, X. Bian, and N. A. Adams. Discussions on the correspondence of dissipative particle dynamics and langevin dynamics at small scales. *Applied Mathematics and Mechanics*, 39(1):31–46, Jan 2018.

[137] T. Shardlow. Splitting for Dissipative Particle Dynamics. *SIAM Journal on Scientific Computing*, 24(4):1267–1282, January 2003.

[138] P Nikunen, M Karttunen, and I Vattulainen. How would you integrate the equations of motion in dissipative particle dynamics simulations? *Computer Physics Communications*, 153(3):407–423, July 2003.

[139] M. Lísal, J. K. Brennan, and J. B. Avalos. Dissipative particle dynamics at isothermal, isobaric, isoenergetic, and isoenthalpic conditions using Shardlow-like splitting algorithms. *The Journal of Chemical Physics*, 135(20):204105, November 2011.

[140] S. Stolz and N. A. Adams. An approximate deconvolution procedure for large-eddy simulation. *Physics of Fluids*, 11(7):1699–1701, July 1999.

[141] S. Stolz, N. A. Adams, and L. Kleiser. An approximate deconvolution model for large-eddy simulation with application to incompressible wall-bounded flows. *Physics of Fluids*, 13(4):997–1015, April 2001.

[142] T. Nakamura and A. Yoshimori. Derivation of the nonlinear fluctuating hydrodynamic equation from the underdamped Langevin equation. *Journal of Physics A: Mathematical and Theoretical*, 42(6):065001, February 2009.

[143] X. Fan, N. Phan-Thien, N. T. Yong, X. Wu, and D. Xu. Microchannel flow of a macromolecular suspension. *Physics of Fluids (1994-present)*, 15(1):11–21, January 2003.

[144] J. Backer. *Bridging time and length scales in Dissipative Particle Dynamics*. Ph.D. thesis, University of Amsterdam, September 2006.

[145] J. A. Backer, C. P. Lowe, H. C. J. Hoefsloot, and P. D. Iedema. Poiseuille flow to measure the viscosity of particle model fluids. *The Journal of Chemical Physics*, 122(15):154503, April 2005.

[146] D. A. Fedosov, G. E. Karniadakis, and B. Caswell. Steady shear rheometry of dissipative particle dynamics models of polymer fluids in reverse Poiseuille flow. *The Journal of Chemical Physics*, 132(14):144103, April 2010.